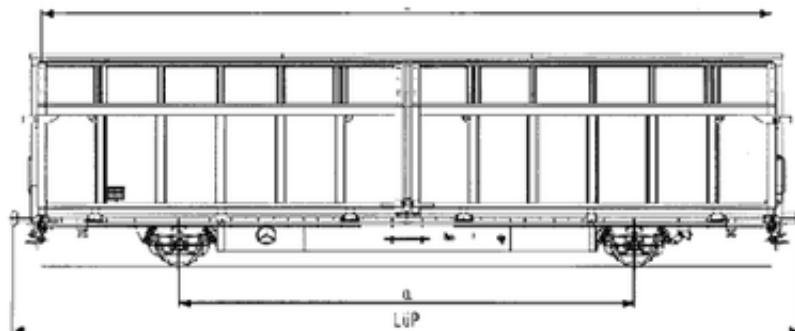


Dry Friction and Impact Dynamics in Railway Vehicles

Dan Erik Petersen
c973539

Mark Hoffmann
c973500



M.Sc.Eng. Thesis

June 2003

Supervisor:

Hans True

Institute:

Informatics and Mathematical Modelling

Technical University of Denmark

Richard Petersens Plads

Building 321

DK-2800 Kongens Lyngby

Denmark

Preface

Work on this thesis commenced the 3rd of February and ended the 23rd of June, 2003. The thesis was completed under the supervision of professor Hans True, at the Institute for Informatics and Mathematical Modelling, Technical University of Denmark. His guidance and insight has been both invaluable and inspiring, and we thank him for his time and help, and the opportunity for producing this thesis.

An important portion of work in this project was carried out at Politechnica Warszawska, Poland, under the supervision of professor Jerzy Piotrowski and with the help of Artur Grzelak. Our stay there was rewarding, both culturally and academically, and we would like to thank them.

Much of the work in this project is based on previous theoretical and numerical work, and our thanks go out to all those who have contributed to the advancement of nonlinear dynamics.

Mark Hoffmann
c973500

Dan Erik Petersen
c973539

23rd June 2003

Abstract

This thesis develops a mathematical model of a Hbbills 311 freight wagon. Central to this model is the UIC double-link suspension which incorporates a parabolic leaf spring. The lateral and longitudinal dynamical model of the UIC suspension is based on theory by Jerzy Piotrowski. This model successfully takes into account damping due to dry friction in the suspension links.

Parameter identification for Piotrowski's model was performed in Warsaw, Poland, on real UIC double linkages. Two sets of parameters were used, the first emphasizing frequency-matching characteristics with the experimental setup, and the second matching theoretical geometric analysis of the suspension joints. Both were used in simulation.

The vertical dynamical model of the UIC suspension is discussed, and several models proposed. Results were generated with the implementation of a piece-wise linear spring-damper system that takes into account the progressive characteristics of the parabolic spring as well as damping due to dry friction.

The wheelsets are constrained by guidance structures of the freight wagon, and the impacts involving these structures are modelled. Wheel-rail contact forces are calculated using the Shen-Hedrick-Elkins method and a wheel-rail contact geometry table (RSGEO) by Walter Kik.

The wheel profile is the S1002 profile, and the rail profile is the UIC60 profile. All modelling and simulation takes place on straight and level track with a fixed gauge of 1435 mm. Low frequency stability dynamics analysis is carried out. The model is implemented through C++ programming, accessed through the command line or a Java GUI, and results analyzed with MatLab .

Keywords: Nonlinear dynamics, railway vehicle dynamics, dry friction, impact dynamics, differential succession.

Contents

1	Introduction	9
2	Mathematical Model	13
2.1	Wheelset Analysis	13
2.1.1	Coordinate Systems	15
2.1.2	Equations of Motion	18
2.2	Car Body Analysis	20
2.2.1	Coordinate Systems	20
2.2.2	Equations of motion	22
2.3	Forces	22
2.4	Complete System	23
3	Wheel-Rail Contact	25
3.1	RSGEO	25
3.2	Creep Forces	25
3.3	Normal Forces	27
4	UIC Suspension Links	29
4.1	Model	29
4.2	Experiment	31
4.2.1	Measuring Equipment	32
4.2.2	Procedure	33
4.3	Analysis	34
4.3.1	Problems	34
4.3.2	Data Fitting Strategy	35
4.3.3	Determining Stiffness	38
4.3.4	Dry Friction Parameter, T_{0i}	41
4.3.5	Model Parameters	41
4.4	Model vs. Measurement	43

5	UIC Vertical Suspension	47
5.1	Standard Leaf Spring	47
5.2	Parabolic Spring	52
5.3	Determining Damping	54
5.3.1	Standard Leaf Spring	55
5.3.2	Parabolic Leaf Spring	60
6	Impact Model	63
6.1	Degrees of Freedom	63
6.2	Mathematical Model	64
6.2.1	Impact	64
6.2.2	Equations	66
6.2.3	Forces	66
6.3	Results	67
7	Freight Wagon Inertia	71
7.1	Empty Freight Wagon	71
7.2	Adding Freight	72
8	Dry Friction Dynamics	75
9	Numerical Approach	79
9.1	Implementation	79
9.2	SDIRK	80
9.3	Jacobi Matrix	80
9.4	Dependencies	83
9.4.1	Front Wheelset	83
9.4.2	Rear Wheelset	84
9.4.3	Car Body	84
9.4.4	Dry Friction Elements	85
10	Results	87
10.1	Method of Attack	87
10.2	Suspension Parameter Set 1	88
10.2.1	Critical Velocities	88
10.2.2	Guidance Impact Behaviour	94
10.3	Suspension Parameter Set 2	112
10.3.1	Critical Velocities	112
10.3.2	Guidance Impact Behaviour	117
10.4	Frequency Analysis	119
10.5	Summary	124

11 Future Work	127
12 Conclusion	129
A Symbols	131
A.1 Latin Symbols	131
A.1.1 A to B	132
A.1.2 C to E	133
A.1.3 F to L	134
A.1.4 M to Q	135
A.1.5 R to V	136
A.1.6 X to Y	137
A.2 Greek Symbols	138
B Parabolic Spring Data	141
C Coordinate Transformations	143
D Creepage	149
E Additional Penetration	153
F Differential Succession of the Dry Friction Element	157
G Maple Code for the Calculations of the Moment of Inertia	161
H RSGEO table	169
I Java Demonstration	173
I.1 Sun Solaris 5.8	173
I.2 Apple Mac OS X.2.6 Jaguar	179

Chapter 1

Introduction

The history of the rail vehicle in Europe is one that stretches back into the 18th century, with the development of first wooden, then steel railed *wagonways*, on which carts were drawn with horses. These *wagonways* evolved into *tramways* and flanged wheels were introduced to rail vehicles in 1789 by William Jessup. In the early 19th century steam power was introduced to these vehicles, and eventually replaced the horse as propulsion power.

The advent of the modern steam engine by James Watt introduced an instrument which aided rail transportation immensely. With the growth of railways and the transportation network they provided, a strong ally in facilitating the industrial revolution, and the spread of industry out in the world had been forged.

Although the long history of rail transportation has seen its ups and downs, the future does look promising, with the advent of new technologies such as intermodal freight trains, and the rise of freight shipments. Shipping rates by rail typically beat the cost of truck shipments, especially over longer distances, and are thus an attractive and important instrument of transportation.

Before the strong emergence and interest of nonlinear dynamics, and especially of bifurcation or catastrophe theory, many decisions involving the design of railway elements and vehicles resided on sound judgement and engineering skills outside these mathematical schools of thought. However, with all man's pursuits, we push ourselves and our inventions beyond their first conceptions, and into unknown territory. Phenomena arose which necessitated further study, systematically breaking down the elements of a train into its constituent parts, modelling these and examining how they behave individually, collectively, and under different conditions. This mathematical analysis and testing became possible with the advent of the digital computer, the increasing performance and availability of computing power and the emergence of numerical algorithms. Phenomena, new and old, which had been observed could now truly be explained or at least examined mathematically, instead of being rationalized away by sound engineering experience.

The goal of this thesis is to systematically assemble a mathematical model of one Hbbills 311 freight wagon and investigate the behaviour in the low frequency domain. This wagon is illustrated in figure 1.1.

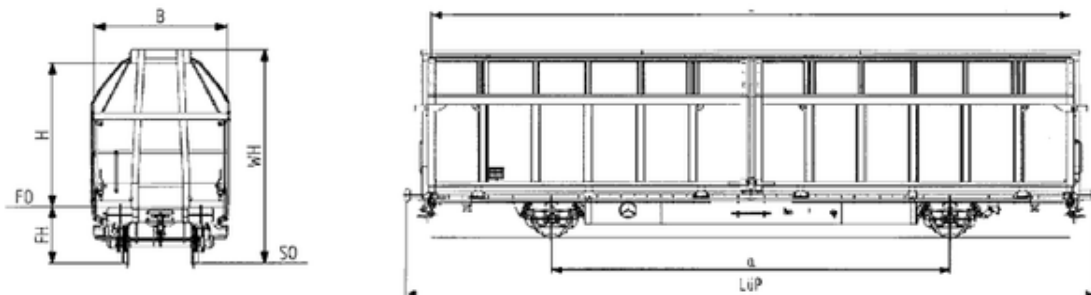
The suspension of the Hbbills 311 is of summary importance in this thesis, since it is chiefly responsible for much of the dynamic behaviour we will investigate. The suspension is dealt with in two chapters, one of which focuses on the longitudinal and lateral characteristics, and the other of which focuses on the vertical suspension characteristics. Beyond this, we have also examined a basic dry friction system in order to shed some light on the behaviour of the UIC suspension.

The important wheel-rail contact interface is modelled through the use of Shen-Hedrick-Elkins theory to determine tangential creep forces, and a tabulated RSGEO data table in order to determine normal forces and the geometrical parameters after suitable dynamic adjustments.

All simulations are performed using S1002 wheel profiles running on UIC60 profile rails canted at $1/40$ towards centerline in accordance with what can be found in Europe. The rail gauge is fixed at 1435 mm throughout our experimentation, and we only consider straight and level track.



(a)



(b)

Figure 1.1: (a) The Hbbills 311 freight wagon. The internal partition walls are clearly visible. (b) Schematic of the Hbbills 311 freight wagon.

Chapter 2

Mathematical Model

In this chapter we derive our mathematical model of the Hbbills 311 freight wagon. We model the freight wagon as a multi body system consisting of two wheelsets and a car body. Through an analysis of each element we set up a nonlinear system of ordinary differential equations that determines the motion of the vehicle.

The interacting forces such as contact forces between wheel and rail, suspension forces and impact forces play a central role in the dynamics of the freight wagon, however, in order to present the mathematical model of the freight wagon as simple as possible the interacting forces are referred to through mathematical symbols, whereas the modelling of these forces are omitted this chapter. The modelling of the interacting forces is the topic of chapters to come.

In figure 2.1 we have shown model pictures of the freight wagon emphasizing the main elements that are important in the mathematical modelling. We refer to appendix A for detailed information of all defined quantities. A few constants we use are given values in table 2.1. We have used the symbol shown in figure 2.2 as a suspension element. The purpose of this is to have an abstract suspension element allowing multiple suspension implementations exhibiting elements such as linear springs/dampers, UIC links, leaf springs and parabolic springs without changing the overall structure of the mathematical model and, ultimately, the construction of the computer program used to solve the mathematical model.

2.1 Wheelset Analysis

In general, a rigid body has six degrees of freedom. Three coordinates to specify the position of the center of mass and three coordinates to specify the rotation of the body around its principal axes. However, the configuration space for a real wheelset is not six dimensional, because the wheelset is constrained (if derailment is neglected) to be in contact with the rails. This constraint connects the lateral and yaw motion with the

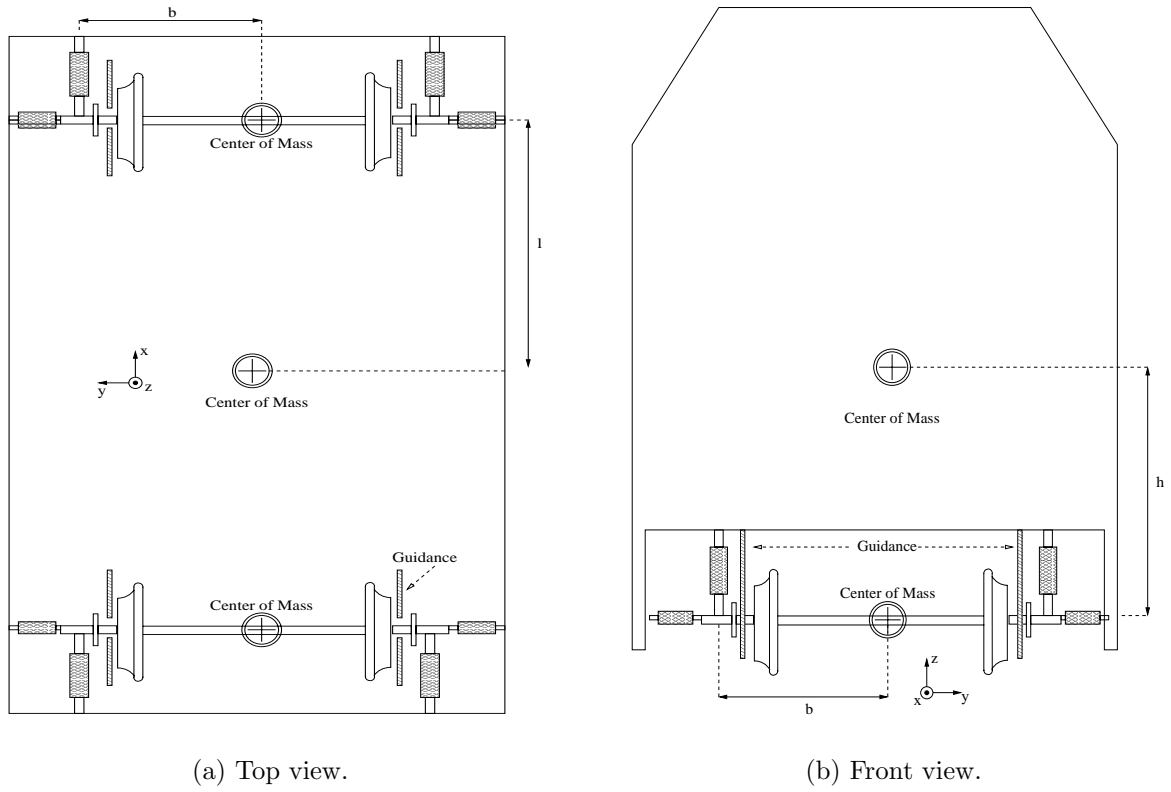


Figure 2.1: Model pictures of the Hbbills 311.



Figure 2.2: General suspension element.

Parameter	Value	Unit
b	1.074	[m]
h	0.802*	[m]
l	5.00	[m]
m_w	1022	[kg]
m_c	13563*	[kg]
I_{wx}	678	[kg m ²]
I_{wy}	80	[kg m ²]
I_{wz}	678	[kg m ²]
I_{cx}	32675*	[kg m ²]
I_{cz}	413097*	[kg m ²]
g	9.82	[m/s ²]

Table 2.1: Some central constants used in the report. Values marked with * are for an empty wagon.

vertical and roll motion of the wheelset.

Instead, in modelling wheelsets one can choose to proceed in another fashion. We have followed the strategy from [9]. This model allows the wheelset to have six degrees of freedom leaving out the kinematic wheel-rail constraint discussed above and we thus avoid having a differential algebraic system to solve. Instead of the constraint, the wheelset penetrates into the rail making the contact forces between the wheel and rail a function of the penetration. Thus, the wheelset has the following degrees of freedom

x : Wheelset longitudinal

y : Wheelset lateral

z : Wheelset vertical

ϕ : Wheelset roll

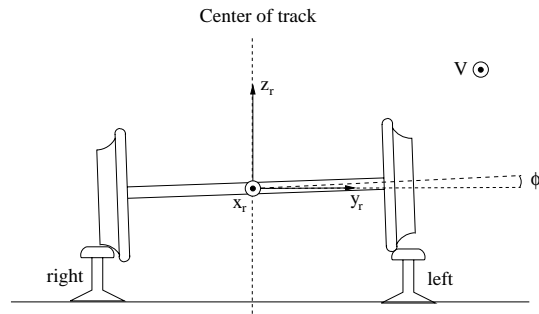
χ : Wheelset pitch

ψ : Wheelset yaw

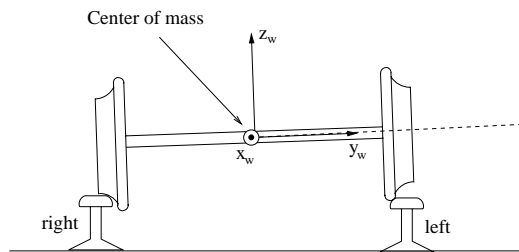
2.1.1 Coordinate Systems

We have found it necessary to define three different coordinate systems regarding the motion of the wheelset. Following the usual conventions in railway dynamics we define a rotation around a longitudinal axis as roll (ϕ), lateral axis as pitch (χ) and vertical axis as yaw (ψ) (see figure 2.4). Furthermore, transformation matrices between all defined coordinate systems are derived and listed in appendix C.

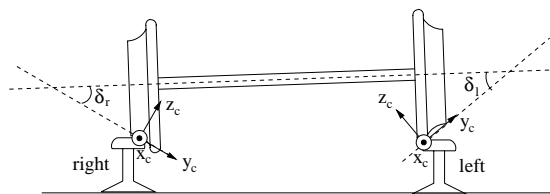
- (X_r, Y_r, Z_r)
A reference frame moving along with the velocity of the vehicle. The subscript is for rail. Each wheelset has its own rail coordinate system and the origin is placed in the center of mass of the wheelset when it is in centered position. This frame is an inertial frame of reference. Positive directions are defined in figure 2.3(a).
- (X_w, Y_w, Z_w)
A coordinate system that follows the wheelsets. The subscript is for wheelset. The coordinate axes are parallel to the principal axes of the wheelset. Each wheelset has its own wheelset coordinate system and the origin is placed in the center of mass. This frame is not an inertial frame of reference. Positive directions are defined in figure 2.3(b).
- (X_c, Y_c, Z_c)
A coordinate system that follows the contact plane between the wheel and rail. The subscript is for contact. The origin is placed in the contact point, see figure 2.3(c). The contact coordinate system is defined because it is a natural reference when the contact forces are going to be described.



(a) Rail coordinate system.



(b) Wheelset coordinate system.



(c) Contact coordinate system for the left and right wheel.

Figure 2.3: Wheelset coordinate systems.

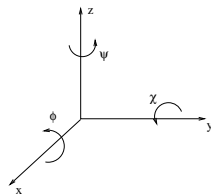


Figure 2.4: Positive directions for the angles (right hand rule).

2.1.2 Equations of Motion

We determine the position of the center of mass of the wheelset by using Newton's second law, whereas the rotation of the wheelset is found through Euler's equations of motion. The application of Newton's second law is straight forward, because we can set up the equations of motion in the rail reference frame, which is an inertial frame of reference. The results of this is

$$\begin{aligned} m_w \ddot{x} &= \sum F_{x,ext}^r \\ m_w \ddot{y} &= \sum F_{y,ext}^r \\ m_w \ddot{z} &= \sum F_{z,ext}^r \end{aligned}$$

However, to determine the rotation of a rigid body in a three dimensional space we have to be more careful. It is seen that the wheelset coordinate system is not an inertial frame of reference, and the consequence of this is that gyroscopic forces has to be taken into consideration. The result of this is formulated in Euler's equations of motion. These equations are derived as follows.

The angular momentum around the center of mass and according to the principal axes of the wheelset is given by

$$\mathbf{L}_C = I_{wx} \dot{\phi} \cdot \mathbf{e}_{wx} + I_{wy} \dot{\chi} \cdot \mathbf{e}_{wy} + I_{wz} \dot{\psi} \cdot \mathbf{e}_{wz}$$

The theorem of angular momentum says that

$$\frac{d\mathbf{L}_C}{dt} = \tau_{C,ext}$$

and since the wheelset coordinate system is rotating we find that

$$\begin{aligned} \frac{d\mathbf{L}_C}{dt} &= I_{wx} \ddot{\phi} \cdot \mathbf{e}_{wx} + I_{wy} \ddot{\chi} \cdot \mathbf{e}_{wy} + I_{wz} \ddot{\psi} \cdot \mathbf{e}_{wz} \\ &\quad + I_{wx} \dot{\phi} \cdot \frac{d\mathbf{e}_{wx}}{dt} + I_{wy} \dot{\chi} \cdot \frac{d\mathbf{e}_{wy}}{dt} + I_{wz} \dot{\psi} \cdot \frac{d\mathbf{e}_{wz}}{dt} \end{aligned}$$

Keeping in mind that the angular velocity of the wheelset coordinate system is $\hat{\omega} = [\dot{\phi}, 0, \dot{\psi}]^T$ we find that

$$\begin{aligned} \frac{d\mathbf{e}_{wx}}{dt} &= \hat{\omega} \times \mathbf{e}_{wx} \\ \frac{d\mathbf{e}_{wy}}{dt} &= \hat{\omega} \times \mathbf{e}_{wy} \\ \frac{d\mathbf{e}_{wz}}{dt} &= \hat{\omega} \times \mathbf{e}_{wz} \end{aligned}$$

thus

$$\begin{aligned} \frac{d\mathbf{L}_C}{dt} &= I_{wx}\ddot{\phi} \cdot \mathbf{e}_{wx} + I_{wy}\ddot{\chi} \cdot \mathbf{e}_{wy} + I_{wz}\ddot{\psi} \cdot \mathbf{e}_{wz} + \hat{\omega} \times \mathbf{L}_C \\ &= \begin{bmatrix} I_{wx}\ddot{\phi} - I_{wy}\dot{\chi}\dot{\psi} \\ I_{wy}\ddot{\chi} + (I_{wx} - I_{wz})\dot{\phi}\dot{\psi} \\ I_{wz}\ddot{\psi} + I_{wy}\dot{\phi}\dot{\chi} \end{bmatrix} \cdot \begin{bmatrix} \mathbf{e}_{wx} \\ \mathbf{e}_{wy} \\ \mathbf{e}_{wz} \end{bmatrix} \end{aligned}$$

From this we find that Euler's equations takes the form

$$\begin{aligned} I_{wx}\ddot{\phi} &= I_{wy}\dot{\chi}\dot{\psi} + \sum \tau_{x,ext}^w \\ I_{wy}\ddot{\chi} &= (I_{wz} - I_{wx})\dot{\phi}\dot{\psi} + \sum \tau_{y,ext}^w \\ I_{wz}\ddot{\psi} &= -I_{wy}\dot{\phi}\dot{\chi} + \sum \tau_{z,ext}^w \end{aligned}$$

The order of $\dot{\phi}$ and $\dot{\psi}$ is about 10^{-2} or less, and $\dot{\chi} \approx V/r_0$, where V is the velocity of the vehicle and r_0 is the known as the *basic rolling radius* of the wheels. We immediately neglect the $(I_{wz} - I_{wx})\dot{\phi}\dot{\psi}$ term due to the multiplication of two low order terms. Furthermore, if we consider a simulation at $V = 30 \text{ m s}^{-1}$ ($r_0 = 0.425 \text{ m}$) we find that

$$\begin{aligned} |I_{wy}\dot{\chi}\dot{\psi}| &< 80 \cdot 71 \cdot 10^{-2} = 56.8 \\ | -I_{wy}\dot{\phi}\dot{\chi} | &< 80 \cdot 10^{-2} \cdot 71 = 56.8 \end{aligned}$$

which is much less than the magnitude of the moments due to the contact, suspension and impact forces, and thus we neglect these terms as well. Leaving out the gyroscopic forces we determine the motion of the wheelset through the following nonlinear system of equations.

$$m_w \ddot{x} = C_{lx}^r + C_{rx}^r + S_{lx}^r + S_{rx}^r + \delta_{lx}^r + \delta_{rx}^r \quad (2.1)$$

$$m_w \ddot{y} = C_{ly}^r + C_{ry}^r + S_{ly}^r + S_{ry}^r + \delta_{ly}^r + \delta_{ry}^r \quad (2.2)$$

$$m_w \ddot{z} = C_{lz}^r + C_{rz}^r + S_{lz}^r + S_{rz}^r - m_w g \quad (2.3)$$

$$I_{wx} \ddot{\phi} = a_l C_{lx}^w - a_r C_{rx}^w + b(S_{lz}^w + \delta_{lz}^w) - b(S_{rz}^w + \delta_{rz}^w) \quad (2.4)$$

$$I_{wy} \ddot{\chi} = -r_l C_{lx}^w - r_r C_{rx}^w \quad (2.5)$$

$$I_{wz} \ddot{\psi} = -a_l C_{lx}^w + a_r C_{rx}^w - b(S_{lx}^w + \delta_{lx}^w) + b(S_{rx}^w + \delta_{rx}^w) \quad (2.6)$$

where C , S and δ are short for contact, suspension and impact forces, respectively. The impact forces are assumed to act in a plane parallel to flat earth.

Equation (2.1) to (2.6) completely defines the position of the wheelset. We can simplify the system slightly, because we are not interested in distinguishing a situation with χ_1 wheelset revolutions from another situation with χ_2 wheelset revolutions. Thus χ in itself is uninteresting, yet $\dot{\chi}$ is very important since the contact forces depend on

the relative velocity between the wheel and rail. Since $\dot{\chi} \sim \frac{V}{r_0}$ we can simplify this as well. We define a pitch angular velocity perturbation, β , as the deviation from the ideal rolling velocity ($\frac{V}{r_0}$):

$$\dot{\chi} = \frac{V}{r_0} + \beta$$

thus equation (2.5) is reduced to

$$I_{wy}\dot{\beta} = -r_l C_{lx}^w - r_r C_{rx}^w$$

2.2 Car Body Analysis

The motion car body is affected by wheelset through suspension forces and impact forces. However, since the inertia of the car body is very big compared to the wheelsets we neglect the longitudinal and pitch motion of the car body. With this simplification we are left with the following four degrees of freedom

y : Car body lateral

z : Car body vertical

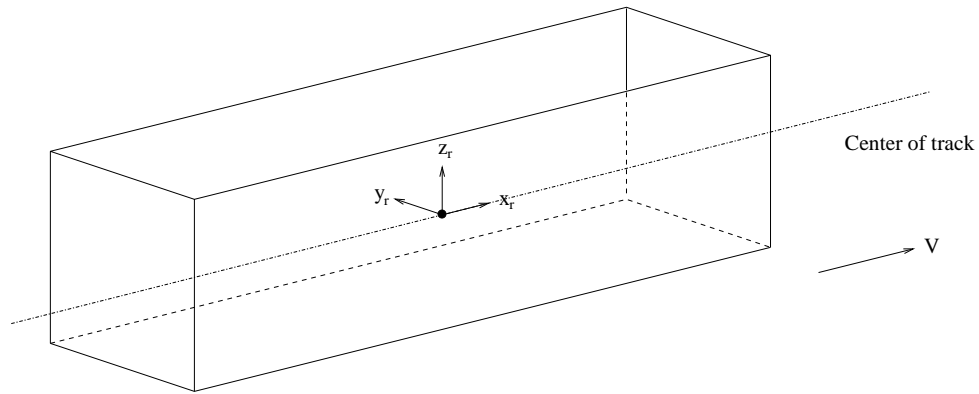
ϕ : Car body roll

ψ : Car body yaw

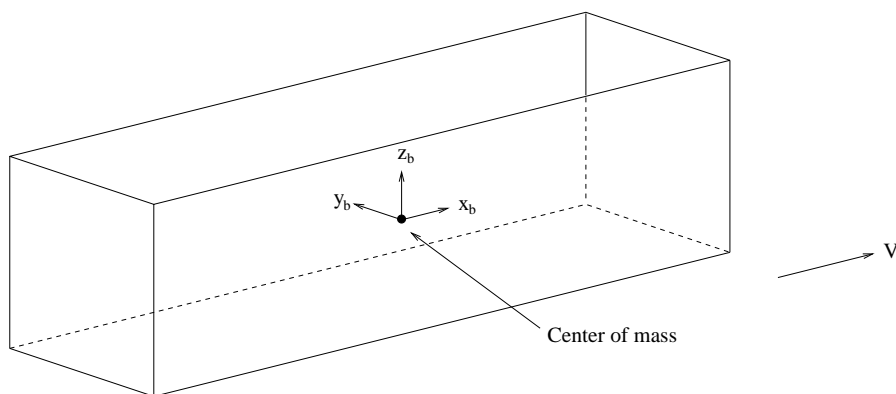
2.2.1 Coordinate Systems

To be able to set up the equations of motion for the car body we now define two reference frames.

- (X_r, Y_r, Z_r)
A reference frame moving along with the velocity of the vehicle. The subscript is for rail. The car body has its own rail coordinate system and the origin is placed in the center of mass of the car body when it is in centered position. This frame is an inertial frame of reference. Positive directions are shown in figure 2.5(a).
- (X_b, Y_b, Z_b)
A coordinate system that follows the car body. The subscript is for car body. The coordinate axes are parallel to the principal axes of the car body. The origin is placed in the center of mass of the car body. Positive directions are shown in figure 2.5(b).



(a) Rail coordinate system.



(b) Car body coordinate system.

Figure 2.5: Car body coordinate systems.

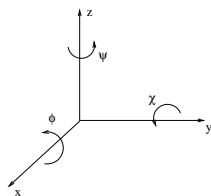


Figure 2.6: Positive directions for the angles (right hand rule).

2.2.2 Equations of motion

We follow the same strategy as before, however, since the order of $\dot{\phi}$, $\dot{\chi}$ and $\dot{\psi}$ are all very small we can neglect gyroscopic effects immediately. Thus, the motion of the car body is determined from

$$\begin{aligned} m_c \ddot{y} &= \sum F_{y,ext}^r \\ m_c \ddot{z} &= \sum F_{z,ext}^r \\ I_{cx} \ddot{\phi} &= \sum \tau_{x,ext}^b \\ I_{cz} \ddot{\psi} &= \sum \tau_{z,ext}^b \end{aligned}$$

leading to

$$m_c \ddot{y} = S_{fly}^r + S_{fry}^r + S_{rly}^r + S_{rry}^r + \delta_{fly}^r + \delta_{fry}^r + \delta_{rly}^r + \delta_{rry}^r \quad (2.7)$$

$$m_c \ddot{z} = S_{flz}^r + S_{frz}^r + S_{rlz}^r + S_{rrz}^r - m_c g \quad (2.8)$$

$$I_{cx} \ddot{\phi} = h(S_{fly}^b + S_{fry}^b + S_{rly}^b + S_{rry}^b + \delta_{fly}^b + \delta_{fry}^b + \delta_{rly}^b + \delta_{rry}^b) \quad (2.9)$$

$$+ b(S_{flz}^b - S_{frz}^b + S_{rlz}^b - S_{rrz}^b + \delta_{flz}^b - \delta_{frz}^b + \delta_{rlz}^b - \delta_{rrz}^b) \quad (2.10)$$

$$I_{cz} \ddot{\psi} = b(-S_{flx}^b + S_{frx}^b - S_{rlx}^b + S_{rrx}^b - \delta_{flx}^b + \delta_{frx}^b - \delta_{rlx}^b + \delta_{rrx}^b) \quad (2.11)$$

$$+ l(S_{fly}^b + S_{fry}^b - S_{rly}^b - S_{rry}^b + \delta_{fly}^b + \delta_{fry}^b - \delta_{rly}^b - \delta_{rry}^b) \quad (2.12)$$

2.3 Forces

The forces involved in the system arise from 3 different characteristic locations : wheel-rail contact, suspension forces and impact forces between the wheelset and car body guidance structures. In our equations, we have labelled wheel-rail contact forces as C , the suspension forces as S and the impact forces as δ .

The superscripts prevalent among these force symbols indicate what coordinate system the value represented by the symbol is measured in. Here we have that w indicates the wheelset coordinate system, b the car body coordinate system and r indicates the rail coordinate system.

Subscripts first indicate if the force is generated on the right, r , or left, l , side of the freight wagon, i.e. the right and left wheel or suspension element. They secondly indicate with what direction they are measured in, with x , y and z being the directions in the corresponding coordinate system.

Furthermore, the car body forces subscripts are prefixed by either f or r , in order to indicate if forces originate from the *front* or *rear* wheelset. The mathematical models that reside behind all these forces are described in the chapters to come.

2.4 Complete System

y_1	Front wheelset longitudinal	y_{31}	T_1 UIC, front left longitudinal
y_2	Front wheelset longitudinal velocity	y_{32}	T_2 UIC, front left longitudinal
y_3	Front wheelset lateral	y_{33}	T_3 UIC, front left longitudinal
y_4	Front wheelset lateral velocity	y_{34}	T_4 UIC, front left longitudinal
y_5	Front wheelset vertical	y_{35}	T_1 UIC, front right longitudinal
y_6	Front wheelset vertical velocity	y_{36}	T_2 UIC, front right longitudinal
y_7	Front wheelset roll	y_{37}	T_3 UIC, front right longitudinal
y_8	Front wheelset roll angular velocity	y_{38}	T_4 UIC, front right longitudinal
y_9	Front wheelset pitch ang. vel. pert.	y_{39}	T_1 UIC, rear left longitudinal
y_{10}	Front wheelset yaw	y_{40}	T_2 UIC, rear left longitudinal
y_{11}	Front wheelset yaw angular velocity	y_{41}	T_3 UIC, rear left longitudinal
y_{12}	Rear wheelset longitudinal	y_{42}	T_4 UIC, rear left longitudinal
y_{13}	Rear wheelset longitudinal velocity	y_{43}	T_1 UIC, rear right longitudinal
y_{14}	Rear wheelset lateral	y_{44}	T_2 UIC, rear right longitudinal
y_{15}	Rear wheelset lateral velocity	y_{45}	T_3 UIC, rear right longitudinal
y_{16}	Rear wheelset vertical	y_{46}	T_4 UIC, rear right longitudinal
y_{17}	Rear wheelset vertical velocity	y_{47}	T UIC, front left lateral
y_{18}	Rear wheelset roll	y_{48}	T UIC, front right lateral
y_{19}	Rear wheelset roll angular velocity	y_{49}	T UIC, rear left lateral
y_{20}	Rear wheelset pitch ang. vel. pert.	y_{50}	T UIC, rear right lateral
y_{21}	Rear wheelset yaw	y_{51}	Leaf spring, front left vertical
y_{22}	Rear wheelset yaw angular velocity	y_{52}	Leaf spring, front right vertical
y_{23}	Car body lateral	y_{53}	Leaf spring, rear left vertical
y_{24}	Car body lateral velocity	y_{54}	Leaf spring, rear right vertical
y_{25}	Car body vertical		
y_{26}	Car body vertical velocity		
y_{27}	Car body roll		
y_{28}	Car body roll angular velocity		
y_{29}	Car body yaw		
y_{30}	Car body yaw angular velocity		

Table 2.2: Table detailing the independent variables in the system.

We define our complete system as the following system of nonlinear first order *ODE*'s.

$$\begin{aligned}
 \dot{\mathbf{y}} &= \mathbf{f}(\mathbf{y}) & \mathbf{y} &= [y_1, y_2, \dots, y_{30}]^T & \text{Suspension type 1} \\
 \dot{\mathbf{y}} &= \mathbf{f}(\mathbf{y}) & \mathbf{y} &= [y_1, y_2, \dots, y_{50}]^T & \text{Suspension type 2} \\
 \dot{\mathbf{y}} &= \mathbf{f}(\mathbf{y}) & \mathbf{y} &= [y_1, y_2, \dots, y_{54}]^T & \text{Suspension type 3}
 \end{aligned} \tag{2.13}$$

The right hand side \mathbf{f} is a vector function defined by the previous analysis of the elements in freight wagon. In table 2.2 it is possible to see a description of y_i . Furthermore, an explanation of the different suspension types is listed below

- **Suspension type 1:** Linear model. All suspension elements are linear spring-dampers.
- **Suspension type 2 :** UIC links are present in the lateral and longitudinal dynamics. A stepwise linear spring-damper represents a parabolic spring in the vertical dynamics.
- **Suspension type 3 :** Standard leaf spring model. UIC links are present in the lateral and longitudinal dynamics. A standard leaf spring represents the vertical dynamics.

Chapter 3

Wheel-Rail Contact

3.1 RSGEO

The contact forces between the wheels and rails play a crucial role when analysing the dynamics of railway vehicles. In order to get a realistic model of the contact forces, [4] has tabulated the geometrical parameters¹ between the *UIC60* rail profile and the *S1002* wheel profile through the use of RSGEO, developed by W. Kik. In general, these geometrical parameters depend on the lateral displacement of the wheelset as well as the yaw motion of the wheelset. The effect of the yaw motion of the wheelset is an additional longitudinal displacement of the contact point, but in simulations with curve radii larger than 200 m this effect is negligible (see [7]). In this project we only consider simulations on a straight and level track, and therefore our geometrical parameters depend only on the lateral displacement of the wheelset.

The strength of the RSGEO table is that we do not have to compute the geometrical parameters during the simulation, because it is tabulated beforehand. However, the table has a certain resolution, which means that we have to do something when we have a lateral displacement of the wheelset in between the table values. We have chosen a simple linear interpolation strategy to get around this problem, and we find it reasonable since the resolution of the table is quite dense². In appendix H we have illustrated the geometrical parameters in order to get a feeling of the data stored in the RSGEO table.

3.2 Creep Forces

In this section we will find expressions for the tangential wheel-rail forces, called creep forces, that arise in the wheel-rail contact patch. Since the wheel-rail interaction is very

¹i.e. rolling radius, position of contact point, size of contact patch, etc.

²table entry every 10^{-5} m of lateral displacement.

important when analysing the behaviour of the vehicle, we have to take into account some of the nonlinearities that exist in this contact.

Several theories have been developed to approximate the creep forces, and the one we use is due to Shen, Hedrick and Elkins (SHE). The method combines Kalker's linear theory with the theory presented by Johnson and Vermuelen, and the result is a nonlinear relationship between the creep forces and the normal forces.

To be able to use SHE we have to find the relative motion between the wheel and rail. This relative motion is called the creepage. This requires some mathematical manipulation which can be found in appendix D. We use SHE because the approximation of the creep forces is good compared to real measurements and it is well suited for dynamic simulations. This well suitedness is due to the fact that SHE consists of explicit formulas. This results in creep force calculations that are very fast compared to iterative methods. We have found the following creep terms.

$$\begin{aligned}\xi_{lx} &= 1 - \frac{r_l \dot{\chi}}{V} + \frac{\dot{x} - a_l \dot{\psi}}{V} \\ \xi_{rx} &= 1 - \frac{r_r \dot{\chi}}{V} + \frac{\dot{x} + a_r \dot{\psi}}{V} \\ \xi_{ly} &= \left(-\psi + \frac{\dot{y} + r_l \dot{\phi}}{V} \right) \cos \delta_l + \frac{\dot{z} + a_l \dot{\phi}}{V} \sin \delta_l \\ \xi_{ry} &= \left(-\psi + \frac{\dot{y} + r_r \dot{\phi}}{V} \right) \cos \delta_r - \frac{\dot{z} - a_r \dot{\phi}}{V} \sin \delta_r \\ \\ \xi_{ls} &= \frac{-\dot{\chi} \sin \delta_l + \dot{\psi} \cos \delta_l}{V} \\ \xi_{rs} &= \frac{\dot{\chi} \sin \delta_r + \dot{\psi} \cos \delta_r}{V}\end{aligned}$$

Kalker's linear theory gives the following creep force components with respect to the contact coordinate system

$$\begin{aligned}\tilde{F}_x &= -a_e b_e G C_{11} \xi_x \\ \tilde{F}_y &= -a_e b_e G \left(C_{22} \xi_y + \sqrt{a_e b_e} C_{23} \xi_s \right)\end{aligned}$$

and the resulting creep force is then

$$\tilde{\mathbf{F}}_\tau = \tilde{F}_x \mathbf{e}_x + \tilde{F}_y \mathbf{e}_y$$

where G is the shear modulus³ and C_{11} , C_{22} and C_{23} are Kalker's creepage coefficients. These coefficients are also provided by the RSGEO table. We adjust the creep force from Kalker's linear theory and the result are the creep forces F_x and F_y , given by

³ $G = \frac{21 \cdot 10^{10}}{2 \cdot (1+0.27)} \frac{N}{m^2} \approx 8.27 \cdot 10^{10} \frac{N}{m^2}$

$$|\mathbf{F}_\tau| = \begin{cases} \mu N \left(\left[\frac{|\tilde{\mathbf{F}}_\tau|}{\mu N} \right] - \frac{1}{3} \left[\frac{|\tilde{\mathbf{F}}_\tau|}{\mu N} \right]^2 + \frac{1}{27} \left[\frac{|\tilde{\mathbf{F}}_\tau|}{\mu N} \right]^3 \right) & \frac{|\tilde{\mathbf{F}}_\tau|}{\mu N} < 3 \\ \mu N & \frac{|\tilde{\mathbf{F}}_\tau|}{\mu N} \geq 3 \end{cases} \quad (3.1)$$

$$\epsilon = \frac{|\mathbf{F}_\tau|}{|\tilde{\mathbf{F}}_\tau|}$$

$$F_x = \epsilon \tilde{F}_x \quad F_y = \epsilon \tilde{F}_y$$

The friction coefficient μ described here is chosen to be 0.15 throughout our simulations. The creep versus creep force relationship given in equation (3.1) is in general not realistic since the creep force will decay when the wheels are spinning, but since we do not have any torque on the wheel axles we can accept the above relationship.

3.3 Normal Forces

The normal forces generated at the contact points arise directly from Newton's third law: every action force has an equal and opposite reaction force. We also consider the wheel and rail to be two elastic bodies, and are thus subject to deformation. In order to model the actual deformation, we consider the two bodies to penetrate into one another without deforming, and use the fact that the normal force depends on this fictitious penetration.

In our effort to determine the normal forces, we are then required to somehow determine characteristics of the contact patch, most especially penetration. Ultimately, to determine the normal force, we take advantage of a relationship between wheel-rail penetration and the normal forces generated.

Our first step is the use of theory presented by Henrich Hertz in the late 19th century (1882) in order to determine contact patch characteristics. This enables us to begin to determine the forces by letting us know the dimensions of the elliptic contact patch between the wheel and rail. This, however, comes under the price of the following four conditions:

- The two bodies in contact must be described by a bilinear polynomial in the point of contact.
- The two bodies are made from completely elastic, homogeneous and isotropic materials.
- The displacement in the point of contact can be neglected.
- The diameter of the contact patch is small compared to the characteristic diameters of the two bodies.

By [4], the relationship between contact patch ellipse semi-axes and penetration with respect to the normal force generated is given by:

$$a_e \propto N^{\frac{1}{3}} \quad b_e \propto N^{\frac{1}{3}} \quad N \propto q^{\frac{3}{2}}$$

RSCEO yields the *static*⁴ normal force as a function of the lateral displacement of the wheelsets. We then adjust the normal force and the contact ellipse geometries dynamically, because the rolling motion and the vertical displacements of the wheelsets will affect the normal force. We do this by using that the above proportionalities yield the following formula for updating the normal force:

$$\begin{aligned} N_0 &= kq_0^{\frac{3}{2}} \\ N_{\text{dyn}} &= kq_{\text{dyn}}^{\frac{3}{2}} \\ q_{\text{dyn}} &= q_0 + \Delta q \end{aligned}$$

Thus

$$\begin{aligned} \frac{N_{\text{dyn}}}{N_0} &= \left[\frac{q_{\text{dyn}}}{q_0} \right]^{\frac{3}{2}} = \left[\frac{q_0 + \Delta q}{q_0} \right]^{\frac{3}{2}} \\ N_{\text{dyn}} &= N_0 \left[1 + \frac{\Delta q}{q_0} \right]^{\frac{3}{2}} \end{aligned}$$

where Δq is the additional penetration given by (see appendix E):

$$\begin{aligned} \Delta q_l &= -(a_{Rl} - y - a_l - \phi r_l) \sin(\delta_l + \phi) + (-z - \phi a_l) \cos(\delta_l + \phi) \\ \Delta q_r &= (-a_{Rr} - y + a_r - \phi r_r) \sin(\delta_r - \phi) + (-z + \phi a_r) \cos(\delta_r - \phi) \end{aligned}$$

Similarly, we update the contact ellipse by

$$\begin{aligned} a_{e,\text{dyn}} &= a_{e,0} \left[\frac{N_{\text{dyn}}}{N_0} \right]^{\frac{1}{3}} \\ b_{e,\text{dyn}} &= b_{e,0} \left[\frac{N_{\text{dyn}}}{N_0} \right]^{\frac{1}{3}} \end{aligned}$$

⁴The normal force when the wheelset is not influenced by external forces except the contact forces and gravity.

Chapter 4

UIC Suspension Links

The UIC link suspension comes in a variety of configurations, but the type that we are interested in here is known as the double-link kind, and is used by many freight wagons in Europe. Figure 4.1 illustrates the entire suspension set up for one side of a wheelset. Figure 4.2 illustrates the double links that characterize this suspension, and which governs the lateral and longitudinal dynamics of the suspension. The vertical spring in these images is a standard leaf spring, and it should be noted again that the vertical spring on the Hbbills 311 is a parabolic spring.

The good properties of the link suspension is that it delivers stiffness as well as damping in an very economic fashion. The stiffness comes into play due to the rise in potential energy for any displacement from equilibrium much like the stiffness present in an ordinary pendulum. The damping in the link suspension is a consequence of the dry friction that occurs in the joints. However, this dissipation of energy is only present when the amplitude of the excitations exceeds a certain limit. This means that for small excitations the joints experience pure rolling (at least in theory) for which there is no loss in energy. This critical value differentiating the rolling motion and sliding motion of the joints depends on many factors such as the dimensions of the joints, weather, state of wear, on so on.

The UIC link suspension exhibits also some undesirable properties. Firstly, the lateral dynamics of the suspension is not satisfactory even though the speed of the vehicle is moderate. Secondly, the dynamics of the vehicle depends highly on the state of the suspension. This state changes significantly with wear, weather conditions and dirt and grime, for example.

4.1 Model

We have used the mathematical model presented by Jerzy Piotrowski (see [8]) to model the lateral and longitudinal dynamics of the UIC suspension. The model is composed

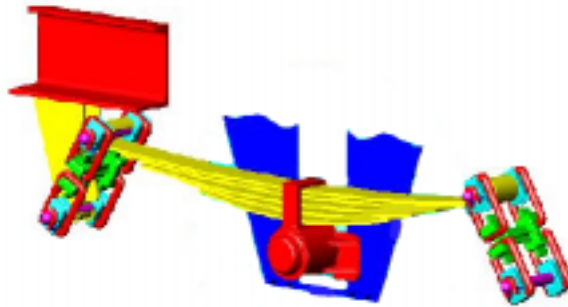


Figure 4.1: Model picture of the UIC double link suspension with the standard leaf spring.

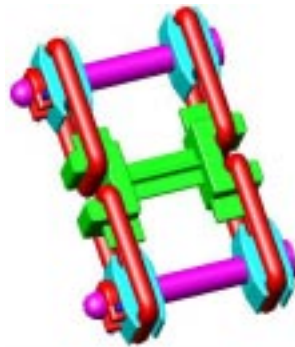


Figure 4.2: UIC double links.

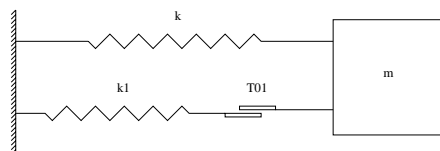


Figure 4.3: Lateral model of the UIC suspension.

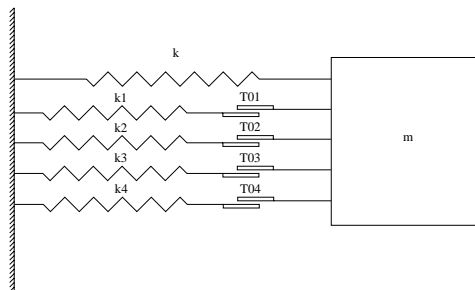


Figure 4.4: Longitudinal model of the UIC suspension.

of linear springs and dry friction sliders (see figure 4.3 and 4.4).

A significant property of this model by Piotrowski is that the stiffnesses of the parameters in the model are assumed to vary *linearly* with respect to the load that the suspension supports. Thus in this chapter we ultimately determine a set of *normalized* parameters, which can be scaled to correct values depending on how much load the suspension supports.

Another consequence of the model that we adopt is that we assume Coulomb's law of friction holds for sliding in the joints. This has been argued for in [8], and a comparison of measurement with the theoretical curve for Coulomb's friction law can be seen in figure F.2 in the appendix. As can be seen, there seems to be an acceptable degree of similarity. Ultimately, this entails that we do not differentiate between static and kinetic coefficients of friction when it comes to sliding in the suspension joints.

The mathematical model is derived through a differential succession of the dry friction element. A derivation¹ of this is found in appendix F and the result is summarized below.

$$\begin{aligned} F &= -ky + T_1 && \text{Lateral} \\ F &= -ky + \sum_{i=1}^4 T_i && \text{Longitudinal} \end{aligned}$$

where T_i are defined by

$$\dot{T}_i = \begin{cases} -k_i \dot{y} & \text{if } |T_i| < T_{0i} \\ -[k_i \dot{y}]^+ & \text{if } T_i = T_{0i} \\ [-k_i \dot{y}]^+ & \text{if } T_i = -T_{0i} \end{cases}$$

The parameters k , k_i and T_0 are determined through *real* experiments on the UIC suspension. The experiments and identification of the parameters is the topic of the following sections.

4.2 Experiment

The aim of this section is to produce a set of parameters for the lateral and longitudinal dynamics of the UIC suspension model. Actual experimental measurements were carried out at the Institute of Vehicles, Warsaw University of Technology, in the month of March, 2003, in cooperation with Artur Grzelak and under the guidance of Jerzy Piotrowski.

As inspired by [8], we focus mainly on the longitudinal and lateral dynamics of the UIC suspension here, and thus it is sufficient for us to create a setup involving only the actual linkages present in the UIC suspension, omitting the leaf spring. The linkages were delivered in a worn state as desired, but in that they were disassembled,

¹This technique is known in non-smooth mechanics but this derivation is not shown in [8].

it was impossible to determine the exact original configuration of the linkages. Unable to assemble the linkages as they originally fit together, we had no other option but to sandblast and reprofile the linkages in an attempt to yield them as new in order to attempt meaningful experimentation with them.

Furthermore, in that the leaf spring is of no interest in our measurements, it is replaced by a stiff beam upon which mass is placed in order to load the linkages. The actual construction of the suspension setup is performed in an upside down fashion, inspired by [8]. This setup is illustrated in figure 4.5. The mass of the beam and added masses total 378.2 kg. This value has remained constant throughout experimentation. The length of the beam replacing the leaf spring is 1.22 m. The angle $\alpha = 25.9^\circ$ represents the angle the linkages form with respect to vertical. The UIC linkage dimensions correspond to those where the longitudinal pivot element has a diameter of 35 mm.

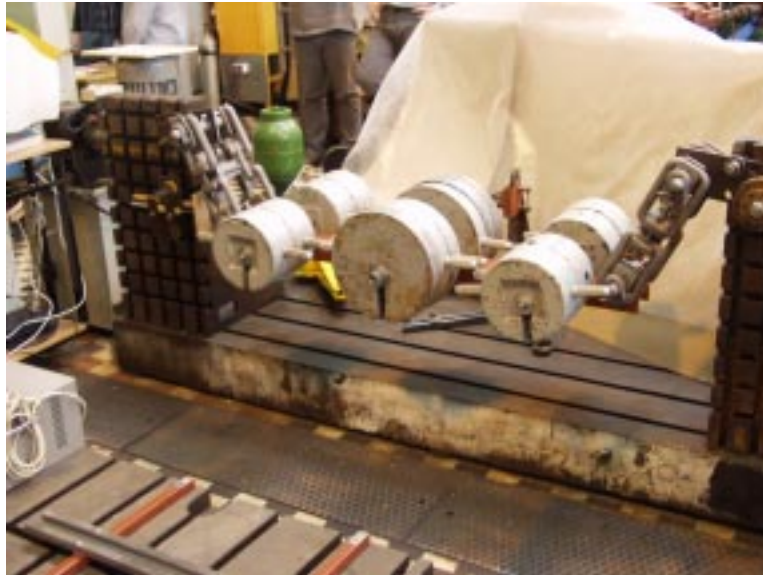


Figure 4.5: The suspension setup.

4.2.1 Measuring Equipment

The suspension setup was instrumented with linear displacement sensors in the longitudinal and lateral directions. They operate on the basis of translating physical displacement into a voltage value that is subsequently transmitted to an amplifier. The amplifier then feeds the analog signal to an analog to digital converter that interfaces with the computer through a PCI card device, and the digital signal is subsequently recorded by software. The displacement sensors can be seen in figure 4.5.

A brief overview of the measurement equipment:

- 2 linear displacement sensors.
- Amplifier.
- Analog to digital converter.
- Computer with available PCI slot.
- Oscilloscope software for sampling data.

4.2.2 Procedure

We here outline the procedures taken to setup the oscilloscope software correctly for measurement. This must be done for both sensors.

1. Ensure that the suspension is at rest.
2. Select the channel for the sensor of interest.
3. Shift the sensor physically such that it registers a voltage corresponding to the middle of the range of voltage it is capable of generating (its own zero-point).
4. Set the oscilloscope software's zero-point for the voltage given by the sensor of interest.
5. Utilizing a standardized block of metal with a known dimension, insert this between the sensor and suspension, taking care not to displace the suspension.
6. Set the oscilloscope software to register the voltage now measured.
7. The oscilloscope software is calibrated by entering the displacement in mm corresponding to the standardized block of metal.
8. Repeat for the other sensor.

Once this is done, we can proceed to limit ourselves to measure only two channels of the sixteen that the digital to analog converter delivers. We also choose the total measurement time to record. In recording, the sampling was done at a rate of 1000 samples per second.

Recordings were performed in one direction at a time, since the mathematical model we strive to implement explicitly separates longitudinal and lateral mathematical elements. Theoretically, they should be kinematically independent. However, in measurement, we are interested in preventing as much dissipation as possible other than that dissipation that will yield parameters for the mathematical model. This is because that low amplitude oscillations do not seem to be nearly as kinematically independent as

the larger amplitude oscillations. This leads to the low amplitude pure rolling oscillations to die off too quickly for proper measurement if oscillation goes on laterally and longitudinally simultaneously.

When recording starts, the suspension is excited in the lateral direction, carefully preventing too much excitation in the longitudinal direction. This is done to an amplitude that takes advantage of the entire range of motion the corresponding sensor can register. Furthermore, excitation of the suspension ceases prior to the suspension reaching an extremum in motion. This is of importance when we later need to determine parameters from measurements. An analogous procedure was used for measurement in the longitudinal direction.

Several measurements were recorded for excitations in both longitudinal and lateral directions in order to limit the data from a poor measurement run polluting calculated parameters.

Once a recording is done, it can be saved in its raw format to disk, but in order to analyse results, the data is converted to ASCII format, and only every 5th data point is sampled. This reduces both the file sizes as well some high frequency noise in the data.

4.3 Analysis

In order to analyse results, we export measurements into ASCII files which are easier to manipulate and extract data from. Also, when the oscilloscope software converts measurements to ASCII files, the original voltage data from the sensors are automatically transformed into displacements according to the calibration done earlier.

The result of a typical experiment is shown in figure 4.6. The time histories shown consists of three different stages. The first stage shows how we have excited the suspension at resonance frequency in order to displace the suspension from equilibrium. We then stop pushing it (at about $t = 3$ s in the longitudinal experiment and $t = 2.5$ s in the lateral experiment) and record approximately 15 seconds of motion all in all. The second stage is the damping transient which is eventually quickly taken over by the “pure” rolling motion in the joints (we see a little dissipation in this motion as well).

In the following sections we are going to describe how we extract the model parameters from the time histories measured.

4.3.1 Problems

It becomes evident, that although the mathematical model of the UIC suspension has four dry friction sliders in order to account for longitudinal behaviour, the stiffnesses of the springs for the individual sliders can not be determined at first glance. Dissipation is so strong in the suspension that it resides most of the time in either all joints rolling, or all joints sliding. Determining the exact moments in which certain joints transition

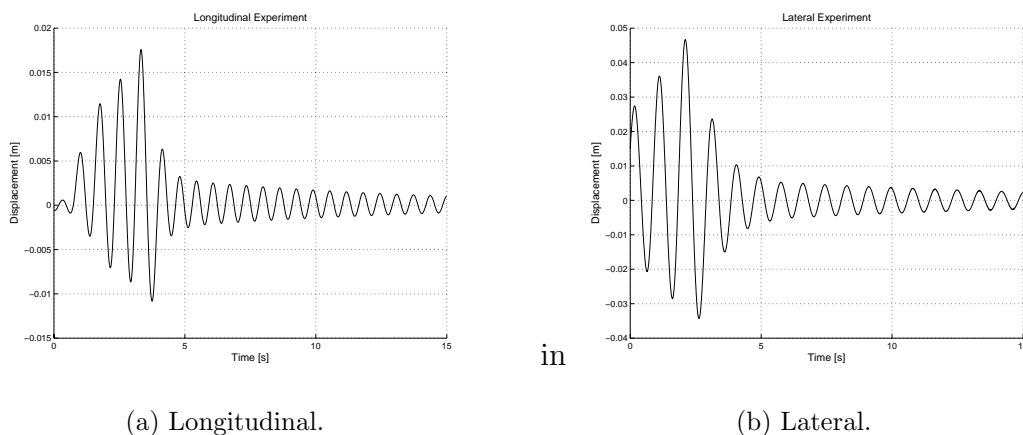


Figure 4.6: Measured results for one of the experiments.

from rolling to sliding is practically impossible. Therefore in the longitudinal case we will only be able to determine the stiffness k exhibited when all joints are sliding, as well as the total stiffness of the system when all joints are rolling. This will let us determine $\sum k_i$, the sum of the stiffnesses of the springs connected with dry friction sliders. In the lateral case, we only have one slider/spring element and $\sum k_i = k_1$.

4.3.2 Data Fitting Strategy

In observing the time series, we see that there are two characteristic frequencies which we wish to extract. This holds for both longitudinal and lateral excitation measurements. These frequencies characterise the suspension when all joints are sliding, and when all joints are rolling. The condition in which all joints are rolling is visible towards the later stages in the time series, when the amplitude of excitation is only being weakly dissipated. However, the condition in which all joints are sliding is more difficult to extract. These frequencies will be used to establish the stiffnesses of the springs in the mathematical model of the UIC suspension.

Sliding

This condition of all joints sliding occurs during the time when maximum dissipation of the amplitude is taking place. If we observe a single extremum of the motion prior to pure rolling, we can be sure that all joints will stick as soon as the velocities of movement in the joints become zero just when the motion reaches the extremum. After this, the suspension joints will progressively cascade into pure sliding as the motion transitions to an opposite extreme. However, prior to the extremum, pure sliding occurs in all joints.

Therefore our strategy becomes one in isolating a section of the time series where pure sliding occurs in all joints. This will be from the point of an extrema, and moving back in time a certain amount. This amount is arbitrary, however we limit it to moving back so far as we don't return to a displacement in which pure rolling will take over later in the time series. Thus we define a cutoff amplitude to prevent us from taking too great a section of the time series for analysis. This will avoid us having a section for analysis in which one or more joints may be rolling.

Once we have agreed on a section of the time series where all joints are sliding, we fit this curve with a sine function of the following form:

$$f(t) = a \sin(\omega_{\text{sliding}}t + \phi)$$

where a indicates the amplitude of the sine function, and is chosen to be the extrema of the curve to be fitted. The choice of $f(t)$ is not random. In that the mathematical model will oscillate like that of a harmonic oscillator when all joints are sliding, a sine function is a natural choice since it is a solution to such a system.

Thus we have two unknowns, namely ω and ϕ . These can be determined since we have two data points our function must intercept, namely at the beginning and end of the time series' section of interest.

(t_1, y_1) : Coordinates indicating the start of the time series' section of interest.

(t_2, y_2) : Coordinates indicating the end of the time series' section of interest.

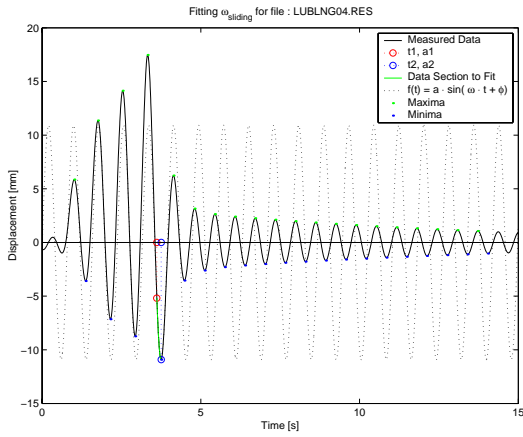
a : The amplitude of the sine fitting function. Taken to be $a = |y_2|$.

ω : The angular frequency of the sine fitting function.

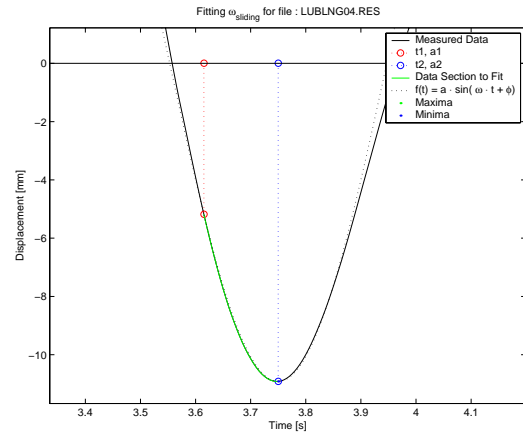
ϕ : The phase of the sine fitting function.

With the coordinates in hand, we can analytically calculate the parameters of our sine fitting function:

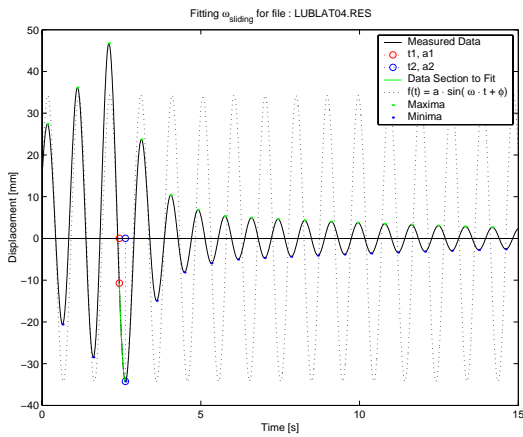
$$\begin{aligned}\omega_{\text{sliding}} &= \frac{\arcsin\left(\frac{y_1}{a}\right) - \arcsin\left(\frac{y_2}{a}\right)}{t_1 - t_2} \\ \phi &= \frac{t_1 \arcsin\left(\frac{y_2}{a}\right) - t_2 \arcsin\left(\frac{y_1}{a}\right)}{t_1 - t_2}\end{aligned}$$



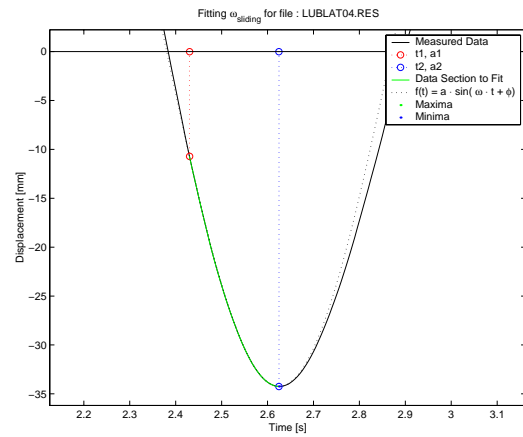
(a) Time series analysis of longitudinal excitation.



(b) Longitudinal case: A close up of the time series analysis detailing the sine function fitting.



(c) Time series analysis of lateral excitation.



(d) Lateral case: A close up of the time series analysis detailing the sine function fitting.

Figure 4.7: Determining the sliding frequency. Cutoff amplitudes were fixed at a value of 5 mm in the longitudinal case, and 10 mm in the lateral case.

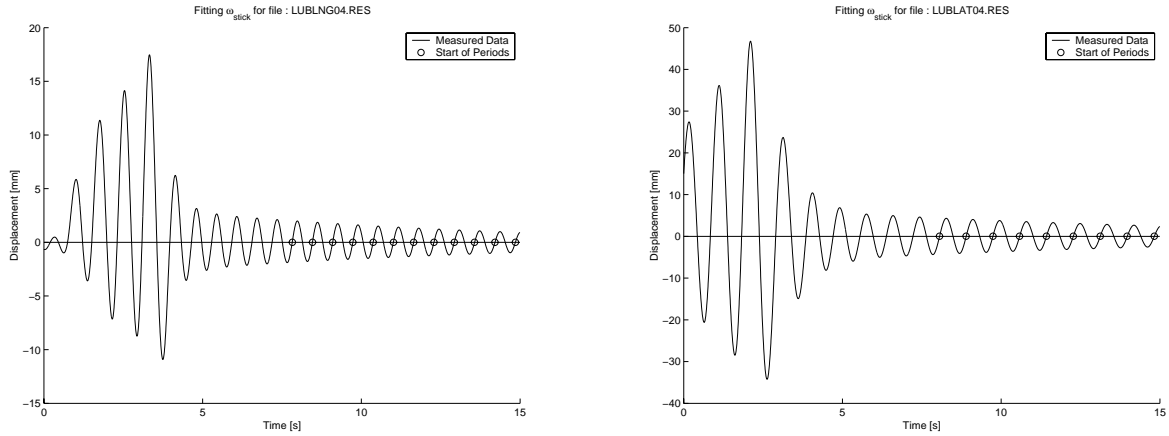
Rolling

In order to determine the stiffness of the system when all joints roll, we concentrate on the section of the time series where dissipation is lowest. This occurs towards the end of the time series, when the strongest dissipation due to joints sticking and slipping has ceased.

The angular frequency in this section of the time series can easily be calculated by summing up a certain amount of periods and using the following formula:

$$\omega_{\text{rolling}} = \frac{2\pi}{T} = \frac{2\pi N}{t_2 - t_1}$$

where t_1 and t_2 indicate the start of the first period and the end of the last period, respectively. The value N indicates the amount of periods in this time span.



(a) Longitudinal case: Determining wavelengths in order to ultimately determine total stiffness.

(b) Lateral case: Determining wavelengths in order to ultimately determine total stiffness.

Figure 4.8: Determining the rolling frequency.

4.3.3 Determining Stiffness

Once we have determined the characteristic angular frequencies, we can determine the stiffness parameters that should be employed by a mathematical model of the suspension:

$$\omega_{\text{sliding}} = \sqrt{\frac{k}{M}}$$

$$\omega_{\text{rolling}} = \sqrt{\frac{k + \sum k_i}{M}}$$

$$k = M\omega_{\text{sliding}}^2$$

$$k + \sum_i k_i = M\omega_{\text{rolling}}^2 \Rightarrow \sum_i k_i = M(\omega_{\text{rolling}}^2 - \omega_{\text{sliding}}^2)$$

In the longitudinal case, we determined the normalized stiffnesses to be $k = 6.4743$ and $\sum k_i = 3.3717$ for this time series. In the lateral case, the time series analysis yielded $k = 4.2010$ and $\sum k_i = k_1 = 1.4222$. By normalized stiffnesses, we mean a stiffness $k_{\text{normalized}} = \frac{k}{Mg}$.

Calculated stiffnesses for all experiments are shown in figures 4.9(a), 4.9(b) and 4.9(c). We compare the values obtained in the lateral experiments to the theoretical stiffnesses derived in [8].

$$k_{\text{norm}} = \frac{1}{2L \cos(\alpha)}$$

$$k_{1,\text{norm}} = \frac{L + \frac{2r^2}{R-r}}{2(L-2r)^2 \cos(\alpha)} - \frac{1}{2L \cos(\alpha)}$$

which for the UIC linkage dimensions $L = 0.165\text{m}$, $R = 0.0135\text{m}$, $r = 0.0125\text{m}$ and angle $\alpha = 25.9^\circ$ yields:

$$k_{\text{norm}} = 3.37 \frac{1}{\text{m}}$$

$$k_{1,\text{norm}} = 10.17 \frac{1}{\text{m}}$$

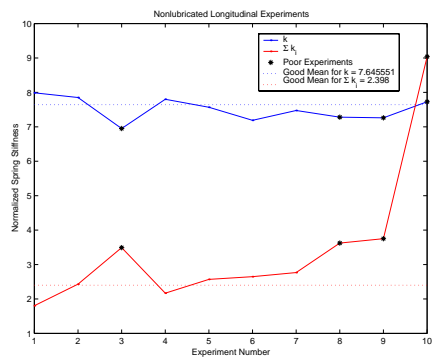
When we compare these values to the identified values over several experiments (illustrated in figure 4.9(c)), we can clearly see a strong difference.

Following the numerical procedure in [8] we have determined the theoretical normalized stiffnesses in the longitudinal case. For further details we refer to the `MatLab` file `uiclong.m` in the source code:

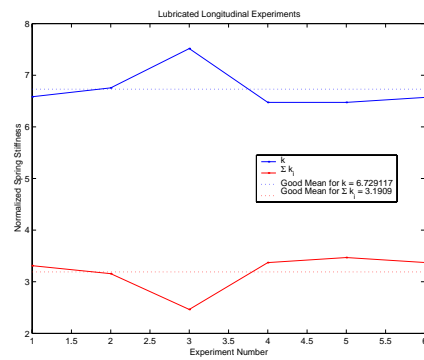
$$k_{\text{norm}} = 2.99 \frac{1}{\text{m}}$$

$$\sum_i k_{i,\text{norm}} = 5.64 \frac{1}{\text{m}}$$

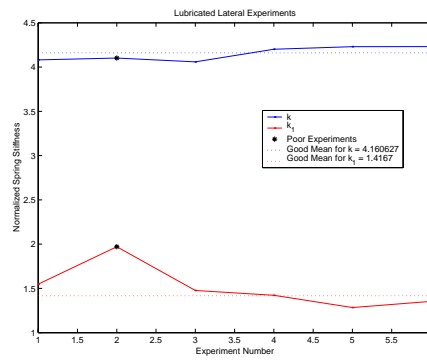
which we compare to figure 4.9(a) and 4.9(b). The main characteristic is that $\sum k_i$ is less than k in measurement, while in numerical simulation of ideal joints, we have k less than $\sum k_i$. This is a serious discrepancy.



(a) Unlubricated longitudinal experiments.



(b) Lubricated longitudinal experiments.



(c) Lubricated lateral experiments.

Figure 4.9:

A conclusion from comparing identified stiffnesses to theoretical stiffnesses is that some assumption made in the theoretical model have been violated. This violation could very well be that the experimental suspension's link geometries are either non-circular, or are circular, but of very different geometry than those for a new UIC double-link suspension. Furthermore, in the assembly of the links, it was not possible to match elements, and thus the linkages aren't "worn into each other".

4.3.4 Dry Friction Parameter, T_{0i}

As no obvious analytical approach is present for the determination of the dry friction parameters T_{0i} we estimated the magnitude of these parameters by comparing direct numerical simulations of the model with the measured results. In the lateral case, there is only one dry friction parameter which is found pretty quick with this comparison strategy. However, in the longitudinal direction we have the same problem as we did in the determination of the stiffness parameters, namely, that it is not possible to distinguish the four individual sliders in the results measured.

4.3.5 Model Parameters

In order to simulate the suspension with the mathematical model we need specific values for all parameters in both directions. So with respect to the problem in the longitudinal direction regarding k_i and T_{0i} for the individual sliders we have chosen appropriate distributions of the parameters between the sliders in order to get the best correspondance between the model and the results measured.

We summarize the results identified in table 4.1 and we define these parameters as suspension parameter set 1. Furthermore, we have shown the theoretical results from [8] in table 4.2, which we define as suspension parameter set 2.

Parameter	Lateral [1]	Longitudinal [1]
k/Mg	4.2010	6.4763
k_1/Mg	1.4222	2.00
k_2/Mg	–	0.50
k_3/Mg	–	0.37
k_4/Mg	–	0.50
T_{01}/Mg	0.014	$6 \cdot 10^{-3}$
T_{02}/Mg	–	$3 \cdot 10^{-3}$
T_{03}/Mg	–	$2 \cdot 10^{-3}$
T_{04}/Mg	–	$2 \cdot 10^{-3}$

Table 4.1: **Suspension Parameter Set 1.** Normalized identified parameters for the model of the UIC suspension.

Parameter	Lateral [1]	Longitudinal [1]
k/Mg	3.413	5.50
k_1/Mg	10.503	3.44
k_2/Mg	–	2.00
k_3/Mg	–	0.33
k_4/Mg	–	1.90
T_{01}/Mg	0.018	$6.98 \cdot 10^{-3}$
T_{02}/Mg	–	$5.11 \cdot 10^{-3}$
T_{03}/Mg	–	$0.91 \cdot 10^{-3}$
T_{04}/Mg	–	$7.16 \cdot 10^{-3}$

Table 4.2: **Suspension Parameter Set 2.** Normalized theoretical parameters for the model of the UIC suspension.

4.4 Model vs. Measurement

We now model the suspension in MatLab (see matlab file `uicidentification.m` and `model.m` in the source code) and compare a measured time series with a simulated one. This was done for both parameter sets.

Figures 4.12(a) and 4.12(b) show a comparison between the experiment and a simulation done using parameter set 1. It is directly clear that as a consequence of how we chose to fit parameters that the frequencies of the simulation and measurement match very well. However, we see that the amplitudes match less well.

To understand why the simulation with parameter set 1 fails to follow the strong dissipation measured we have to analyse the dry friction element (see figure 4.10).

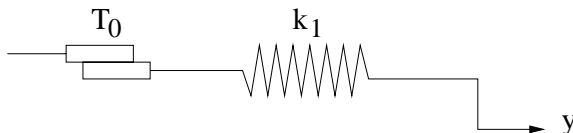


Figure 4.10: Dry friction element.

The dissipation in the model originates from this element. The amount of dissipated energy in the model depends on the parameter T_0 *as well* as the spring stiffness, k_1 . This is seen from the continuity equation

$$k_1 y = T$$

where T is the restoring force from the friction slider. Dissipation occurs for displacements larger than

$$k_1 y_c = T_0 \quad \Rightarrow \quad y_c = \frac{T_0}{k_1} \quad (4.1)$$

Increasing the parameter T_0 obviously leads to greater dissipation *when* sliding, however, the critical displacement at which sliding occurs is postponed according to equation (4.1). In reference to figure 4.11 this means that the slope α becomes steeper, but y_c is increased. So in the determination of the identified parameters in e.g. the lateral case in figure 4.12(a) the problem is as follows. We would like to have a steeper slope in the dissipative phase in order to follow the measured result. This requires an increment in T_0 , however, since we can not allow y_c to increase we have to lower k_1 , but our hands are tied because k_1 is fixed from the sliding and rolling frequencies measured.

Figures 4.12(c) and 4.12(d) show a comparison between experiment and a simulation using parameter set 2. Here we see that amplitudes seem to match better in the strong dissipative phase of movement, yet oscillation frequencies do not match at all in the rolling phase.

The conclusion from this is that the mathematical model does not model the experiment correctly. We have seen that the model can either recreate the frequencies or the dissipation slope from the experiment, but it was not possible to model both at the same time.

Although, we have this dissimilarity we do not discard the model right away, because it should be kept in mind that the UIC links were delivered disassembled and thus it was impossible to determine the original configuration of the linkages. The fact that the links are not worn into each other might introduce some additional dissipation, which could explain the low frequency measured in the rolling phase.

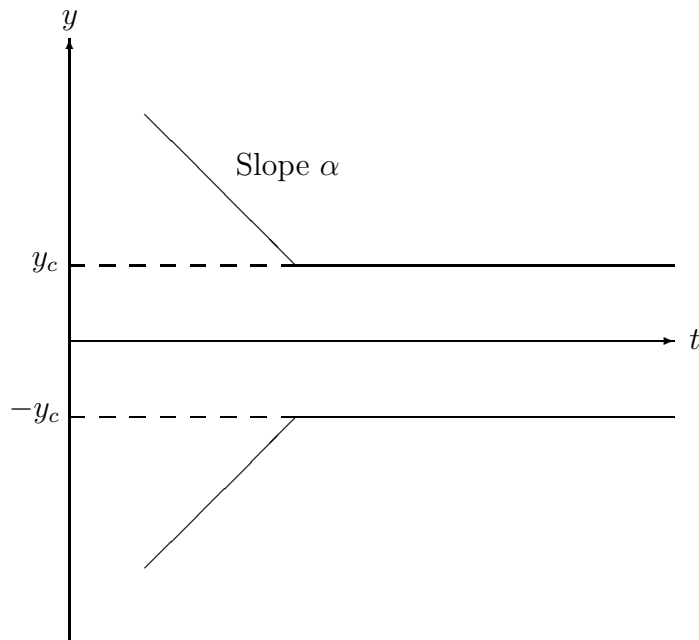
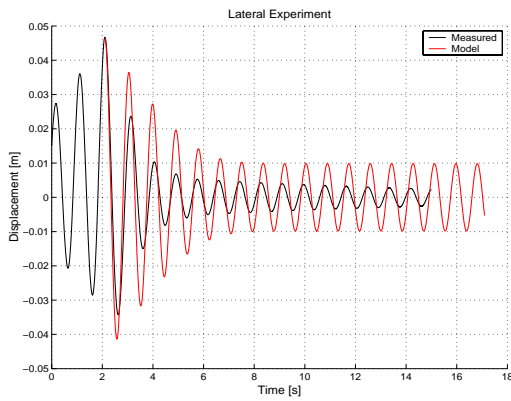
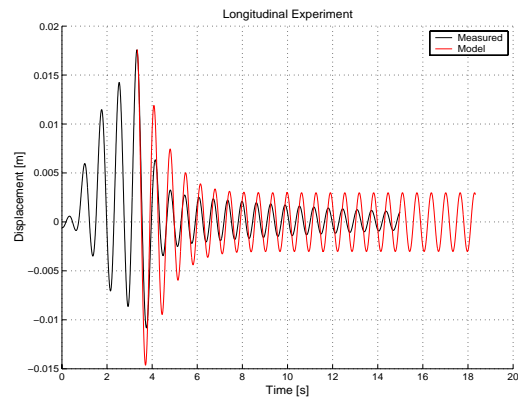


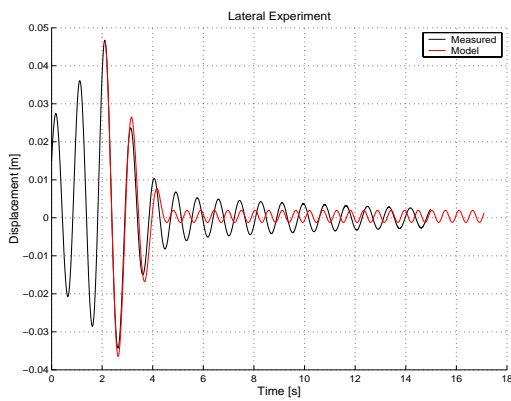
Figure 4.11: Schematic diagram illustrating the time history envelope produced by the model in the lateral direction.



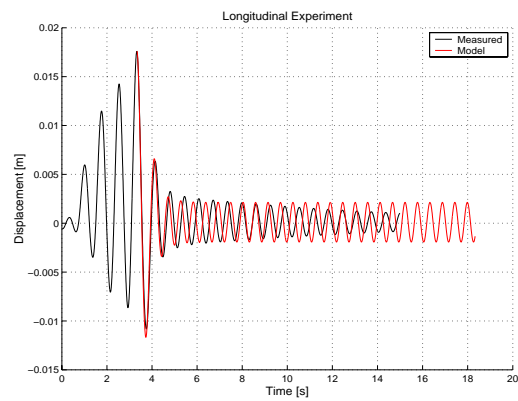
(a) Comparison between measured experiment and model with the identified parameters in the lateral direction. It is seen that the frequency is correct, but the amplitude overshoots.



(b) Comparison between measured experiment and model with the identified parameters in the longitudinal direction. It is seen that the frequency is correct, but the amplitude overshoots.



(c) Comparison between measured experiment and model with the theoretical parameters in the lateral direction. It is seen that the amplitude is good on the first part, however there is an overall difference in frequency.



(d) Comparison between measured experiment and model with the theoretical parameters in the longitudinal direction. It is seen that the amplitude is good on the first part, however there is an overall difference in frequency.

Figure 4.12: Model vs. Experiment.

Chapter 5

UIC Vertical Suspension

This chapter deals with how we model the vertical spring dynamics of the UIC suspension. The suspension found on the Hbbills 311 is of the parabolic leaf spring type, however before we present the model for the parabolic spring, we first treat the case of a standard leaf spring, as found on other freight wagons running the UIC double link suspension.

This is done since the model for the standard leaf spring may one day be able to be modified in order to perhaps better model the parabolic spring, compared to how we currently model it, or even replace it in the case of modelling a freight wagon with standard leaf springs.

Finally, we present a section on how we determine the damping in the different types of vertical suspension discussed in this chapter, based on analysis of a dry friction system.

5.1 Standard Leaf Spring

The theory that governs the dynamics of the standard leaf spring have been garnered from [2], and parameters for it have been calculated with the help of [6]. In figure 5.1 we have a sketch of a leaf spring supporting a mass.

According to [2], an equation presented by Paul Fancher *et al* was used to model the dynamics of a leaf spring. It basically models the leaf spring as having two different characteristic spring constants, one for when the spring is being loaded and another when being unloaded. Ultimately, the behaviour of the spring will be such that forces will tend towards *envelopes* defined by these constants as the spring is loaded and unloaded. A diagram is given in figure 5.2 of these envelopes.

The following equation dictates the behaviour of our leaf spring.

$$\frac{\partial F}{\partial \delta} = \frac{F_{env} - F}{\beta}$$

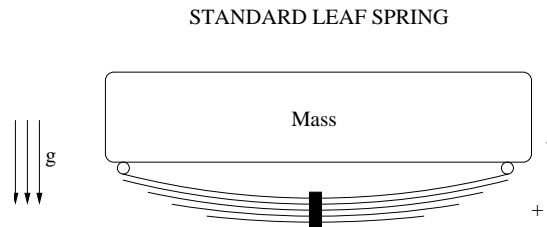


Figure 5.1: A diagram showing the leaf spring supporting a mass. The diagram also indicates positive directions as well as the gravitational field.

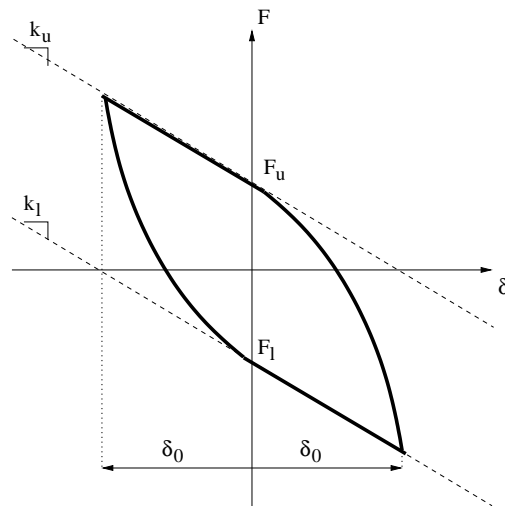


Figure 5.2: A diagram showing the hysteresis loop of the mathematical model, and the envelopes to which forces tend to under a sinusoidal load cycling. The loop is counter-clockwise in direction.

where

F : Spring force [N].

F_{env} : Force on the upper or lower envelope, depending on if we're unloading or loading the spring [N].

δ : Spring deflection [m]. As opposed to displacement, deflection does not preserve an orientation.

β : Decay constant [m].

If we take the equation that defines the behaviour of the leaf spring, we can manipulate it such that we have a form we can use in our system of differential equations.

$$\begin{aligned}\frac{\partial F}{\partial \delta} &= \frac{F_{env} - F}{\beta} \\ \frac{\partial F}{\partial \delta} \cdot \frac{\partial \delta}{\partial t} &= \frac{F_{env} - F}{\beta} \cdot \frac{\partial \delta}{\partial t} \\ \frac{\partial F}{\partial t} &= \frac{F_{env} - F}{\beta} \cdot \frac{\partial \delta}{\partial t} \\ \dot{F} &= \frac{F_{env} - F}{\beta} \dot{\delta}\end{aligned}$$

The value F_{env} can be a force pertaining to one of the two linear envelopes characterized by the spring constant under loading or unloading, as well as a 'pretensioned' force at zero deflection under loading or unloading. Here, subscripts stand for *upper* and *lower* envelopes. These could also stand for *unloading* and *loading*. The value x is displacement, while δ is deflection¹.

$$\begin{aligned}F_{env_u} &= k_u x + F_u \\ F_{env_l} &= k_l x + F_l\end{aligned}$$

Thus our system is

$$\dot{F} = \begin{cases} \frac{k_u x + F_u - F}{\beta} \dot{\delta} & \text{under unloading.} \\ \frac{k_l x + F_l - F}{\beta} \dot{\delta} & \text{under loading.} \end{cases}$$

It is from [6] that we work out the final form of our model, and fit the correct parameters for the leaf spring model we ultimately wish to implement. Thus we take the just previously described system, and adapt it for the constants and form detailed in [6]. Figure 5.3 shows the hysteresis diagram for which [6] dictate that leaf springs

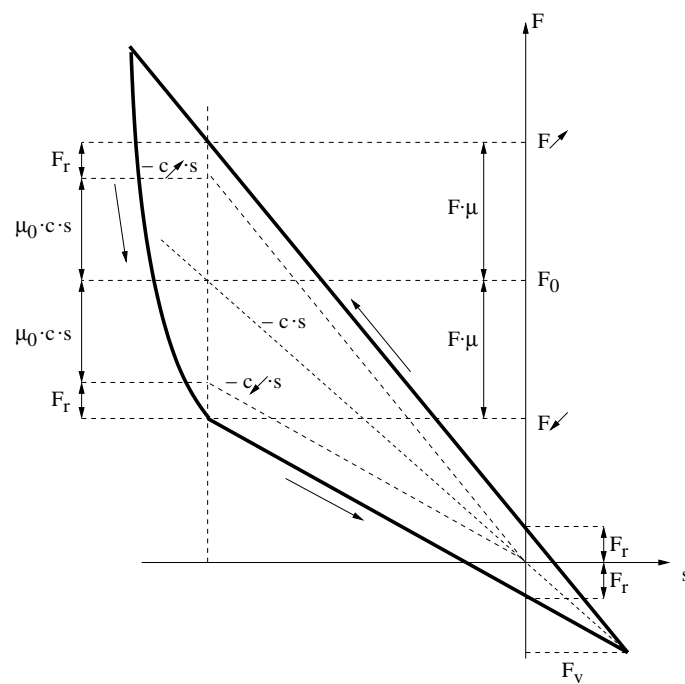


Figure 5.3: A diagram showing the hysteresis loop of the leaf spring according to [6] under a load-unload movement. The loop is counter-clockwise in direction. Keep in mind that the spring constants and F_r are positive values.

behave under, and it is this behaviour we will adapt our model to. This diagram is shown as force versus a displacement s .

We here see that the spring is characterized by two spring constants, namely c_{\nearrow} and c_{\searrow} (which are positive). These indicate the stiffness of the spring under loading and unloading, respectively. The stiffness constant c is an average of these two. A constant μ_0 is used to indicate this relationship, and is defined as follows:

$$\mu_0 = \frac{F_r}{F_v}$$

Where F_v being the pretensioning force in the leaf spring, and F_r is known as the “left over” force in the spring at zero deflection. Thus the loading and unloading stiffnesses can be calculated from the average stiffness c as follows.

$$\begin{aligned} c_{\nearrow} &= c(1 + \mu_0) \\ c_{\searrow} &= c(1 - \mu_0) \end{aligned}$$

The parameters that ultimately need to be known in order to have a working model of the leaf spring are the following positive values:

- Average stiffness c .
- Decay constant β .
- Factor μ_0 .
- “Remainder” force F_r . Alternately, F_v .

Most of these parameters are unknown to us, yet average stiffness can be easily garnered from actual parabolic spring data which will be presented later on. The factor μ_0 is also found in such a fashion. The decay constant is a parameter which we have no data on how to fit, and must ultimately guess our way to. The force F_r then becomes the last unknown, and must be found through a dry friction analysis of the system. This is done in section 5.3.

Thus our system is

$$\dot{F} = \begin{cases} \frac{-c_{\searrow}s + F_r - F}{\beta} |\dot{s}| & \text{when } \dot{s} < 0 \quad (\text{unloading}) \\ \frac{-c_{\nearrow}s - F_r - F}{\beta} |\dot{s}| & \text{when } \dot{s} > 0 \quad (\text{loading}) \end{cases}$$

This mathematical model is implemented and can be used optionally. This model may come in handy in a future version of the parabolic leaf spring model, of which the current version that we use is presented next.

¹ x is orientation preserving, while δ is not.

5.2 Parabolic Spring

The actual vertical suspension on the Hbbills 311 freight wagon is of the parabolic spring type. Similar to the standard leaf spring in that it is comprised of “leaves”, it differs in the construction in that there is less contact between the leaves, and thus less dry friction. Thus we can expect that this spring experiences less damping due to dry friction.

Another significant difference is that a “supplementary” leaf exists in the parabolic spring which comes into play once the spring is loaded enough. This leaf stiffens the spring considerably, and introduces a discontinuity in the first derivative of the stiffness versus load. Figure 5.4 illustrates the general configuration of the parabolic spring, while 5.5 shows the discontinuity previously mentioned as an abrupt change in slope.

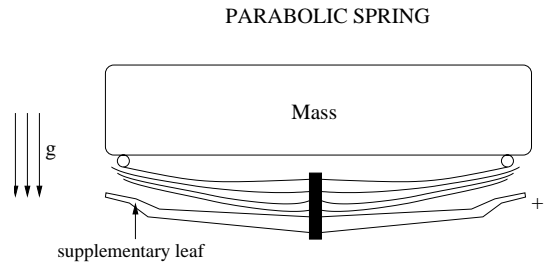


Figure 5.4: A diagram showing the parabolic spring supporting a mass. The diagram also indicates positive directions as well as the gravitational field. Notice the supplementary leaf.

We received parabolic spring data from DSB Drift² which at first glance indicate that it’s behaviour is approximately piecewise linear with respect to stiffness. The data also mentions a deviation of $\pm 7\%$ which could be a guess for factor μ_0 in the standard leaf spring case. From the diagram illustrating the stiffness characteristic given in figure 5.5 we are inspired to model the parabolic spring as a piecewise linear spring-damper system. Stiffnesses were calculated based on slopes in figure 5.5, however determining the damping the springs would provide is a tougher proposition.

Thus our model for the parabolic spring is a piecewise linear spring-damper system:

$$F = \begin{cases} k_{\text{unsupplemented}} \cdot s + d \cdot \dot{s} & \text{when } s < 62.9 \text{ mm} \\ F_0 + k_{\text{supplemented}} \cdot (s - s_0) + d \cdot \dot{s} & \text{when } s \geq 62.9 \text{ mm} \end{cases} \quad (5.1)$$

Where (s_0, F_0) defines the point at which the supplementary leaf begins to act. Furthermore, d is chosen to be either d_{loaded} or d_{unloaded} depending on whether or not the wagon is fully loaded or not to begin with. This is because the damping of the parabolic spring will depend on whether or not the supplementary leaf is involved.

²Danish State Railways.

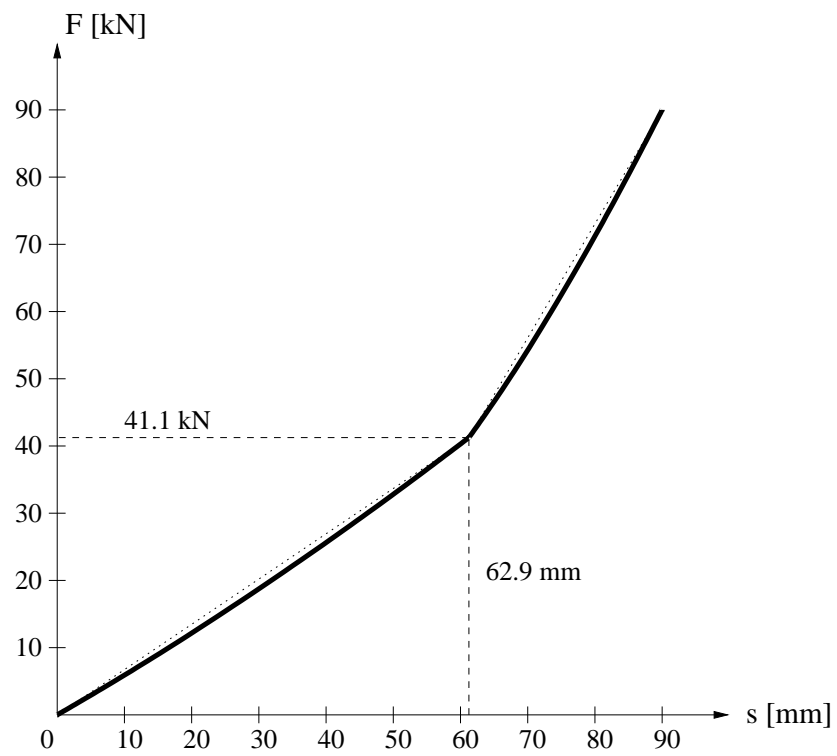


Figure 5.5: A diagram showing the parabolic spring's near piecewise linear stiffness. At 62.9 mm displacement (41.1 kN restoring force), the supplementary leaf comes into play.

5.3 Determining Damping

In order to determine the linear damping of the parabolic spring model, and the force F_r of the standard leaf spring model, we must engage in a simple dry friction analysis of the suspension. It is such that we will fit these parameters with a simple system that dampens using dry friction. This can be done, since we do have data from [6] that indicates to us the average friction in the vertical suspension of a freight wagon. Thus our strategy will be to match damping characteristics of a simple dry friction system, with that of the model we wish to fit parameters for. Firstly, we will describe the simple dry friction system we consider.

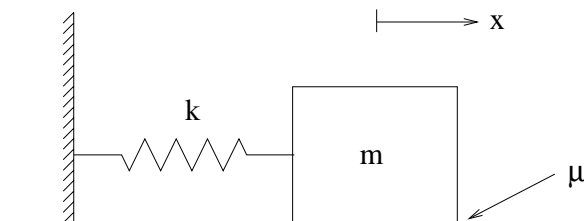


Figure 5.6: A simple system with dry friction.

We consider the system illustrated in figure 5.6. The mathematical model for the system is

$$m\ddot{x} + kx + \mu mg \cdot \text{sign}(\dot{x}) = F(t)$$

where μ is a friction coefficient, and $F(t)$ is a forcing function that influences the position of the mass in that

$$x = a \sin(\omega t)$$

By multiplying by \dot{x} and integrating over one period we get

$$\begin{aligned} m\ddot{x}\dot{x} + kx\dot{x} + \mu mg \cdot \text{sign}(\dot{x})\dot{x} &= F(t)\dot{x} \\ \frac{d}{dt} \left[\frac{1}{2}m(\dot{x})^2 + \frac{1}{2}kx^2 \right] + \mu mg|\dot{x}| &= F(t)\dot{x} \\ \underbrace{\left[\frac{1}{2}m(\dot{x})^2 + \frac{1}{2}kx^2 \right]_0^{\frac{2\pi}{\omega}}}_0 + \mu mg \int_0^{\frac{2\pi}{\omega}} |a\omega \cos(\omega t)| dt &= \int_0^{\frac{2\pi}{\omega}} F(t)\dot{x} dt \end{aligned}$$

This equation basically tells us that the work due to the friction force should correspond to the energy input from the external force, $F(t)$, in order to leave the mechanical energy

unchanged. Furthermore, the dry friction work is found to be

$$\begin{aligned}
 W_\mu &= \mu mg \int_0^{\frac{2\pi}{\omega}} |a\omega \cos(\omega t)| dt \quad \left\{ \begin{array}{l} \phi = \omega t \\ d\phi = \omega dt \end{array} \right\} \\
 &= \mu mg a \omega \int_0^{2\pi} |\cos \phi| d\phi \\
 &= \mu mg a \omega \left[\int_0^{\frac{\pi}{2}} \cos \phi d\phi + \int_{\frac{\pi}{2}}^{\frac{3\pi}{2}} (-\cos \phi) d\phi + \int_{\frac{3\pi}{2}}^{2\pi} \cos \phi d\phi \right] \\
 &= \mu mg a \omega [(1 - 0) - (-1 - 1) + (0 - (-1))] \\
 &= 4a\mu mg
 \end{aligned}$$

Where the coefficient of friction was chosen to be $\mu = 0.13$, since this is what [6] estimates for a *new* set of standard leaf springs³.

5.3.1 Standard Leaf Spring

In looking at the dry friction work for our simple system, we see that the work grows linearly with the amplitude of the excitation. If we were interested in determining parameters for a standard leaf spring, we would first observe the hysteresis loop in figure 5.2, and in the case of *strong* decay constants β , we can approximate this to figure 5.7. Thus we can proceed analytically:

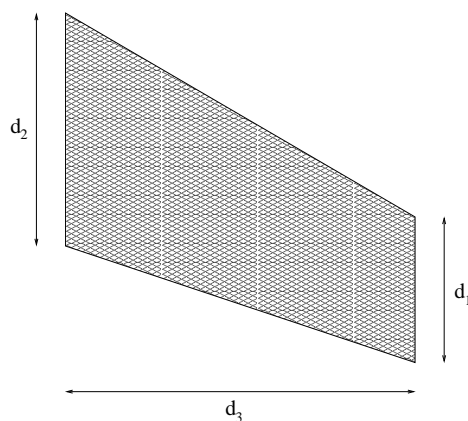


Figure 5.7: The hysteresis for a standard leafspring is approximately quadrilateral, for springs that quickly switch between stiffnesses (have strong decay constants).

³For two and three year old springs, [6] estimates this to $\mu \approx 0.30$.

$$\begin{aligned}
d_1 &= -c_{\nearrow}a + F_r + c_{\searrow}a + F_r = (c_{\searrow} - c_{\nearrow})a + 2F_r \\
d_2 &= c_{\nearrow}a + F_r - c_{\searrow}a + F_r = (c_{\nearrow} - c_{\searrow})a + 2F_r \\
d_3 &= 2a
\end{aligned}$$

The area of the polygon is $\frac{1}{2}d_3(d_1 + d_2)$. This is equated to the work due to the dry friction force:

$$\begin{aligned}
\frac{1}{2}d_3(d_1 + d_2) &= 4a\mu mg \\
\frac{2a}{2}(4F_r) &= 4a\mu mg \\
4F_r &= 4\mu mg
\end{aligned}$$

Thus in the case of a standard leaf spring with strong decay:

$$F_r = \mu mg$$

We now present a series of figures generated by **MatLab** that showcase our model. We refer to files `leafspringharmonic.m` and `leafspringdynamic.m` in the source code. In figure 5.8, we subjected our mathematical model to harmonic movement, and registered the generated restoring force from the leaf spring model. The parameters used in this simulation were the following, which are based on one leaf spring supporting it's quarter share of an empty freight wagon.

```

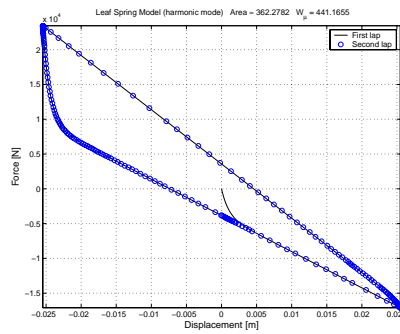
c = 0.65e6; %average spring constant
Fr = 4350; %envelope offset at zero displacement
mu0 = 0.2; %relative difference between envelopes
mu = 0.13; %average friction in leaf spring (fitting purpose)

g = 9.82; %gravitational constant
M = 0.25*13563; %leaf spring bearing load (empty wagon)
k = 0.65e6; %linear spring constant
d = 34440; %linear damping constant

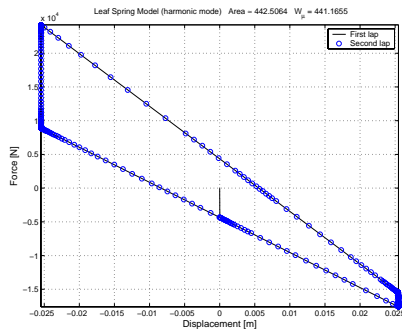
a = 0.5*0.050959; %displacement is half that of settling distance

```

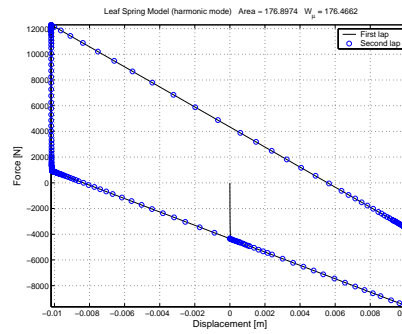
The energy dissipated per cycle by the hard decaying model in figures 5.8(b) and 5.8(c) match that of the simple dry friction system much better than the soft decaying model in figure 5.8(a). This comes about since our analytical approach to estimating F_r was performed under an assumption that the decay constants were strong. An iterative approach can be used in order to better estimate F_r in all cases, but this has not been implemented since the main focus of our project is not the standard leaf spring model.



(a) Harmonic movement for $\beta = 10^{-3}$.



(b) Harmonic movement for $\beta = 10^{-5}$.



(c) Harmonic movement for $\beta = 10^{-5}$, and smaller amplitude.

Figure 5.8: Harmonic movement simulations for the standard leaf spring model.

In figure 5.9, we supply our model with an initial condition of zero displacement, and let it fall under gravity towards the normal equilibrium compression displacement. This is done both for soft and hard decay constants, and we present both a time history of the displacement of the freight wagon vertically, as well as a diagram showing restoring force versus displacement.

We utilized the same parameters as mentioned before, but in varying the decay constant, we obtain different behaviours. Throughout, we compare the movement to that of how a linear spring-damper suspension would move, which has a stiffness of $k = 0.65 \cdot 10^6$ [N m⁻¹], and a damping constant of $d = 34.44 \cdot 10^3$ [N s m⁻¹].

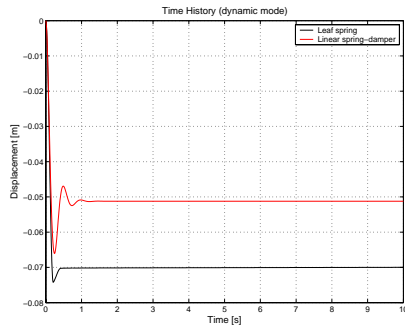
```
k = 0.65e6 %spring constant
d = 34440  %damping constant
```

These parameters will actually be the ones determined for the parabolic spring model in the empty freight wagon case.

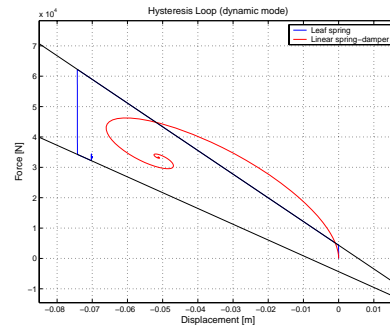
Figures 5.9(a) and 5.9(b) show the movement of a standard leaf spring with a hard decay constant ($\beta = 10^{-5}$). We see that the system behaves in an over damped fashion, coming quite slowly to the equilibrium position after an initial strong damping movement.

In figures 5.9(c) and 5.9(d) we see movement for a softer decay constant $\beta = 10^{-3}$. We see that the system still seems to be over damped.

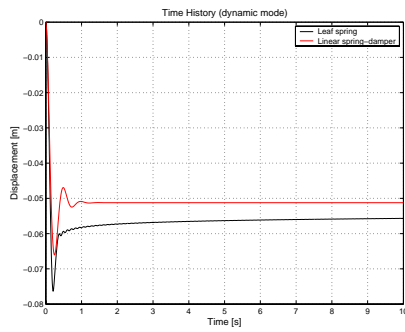
Ultimately, figures 5.9(c) and 5.9(d) show movement for an even softer decay constant $\beta = 5 \cdot 10^{-3}$. Here, the system seems slightly under damped, but we also see that it follows the linear spring-damper movement much more closely, oscillating about the equilibrium point, instead of approaching it from one direction only.



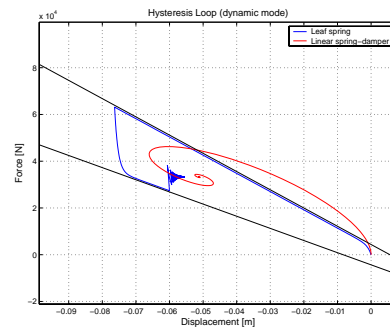
(a) Dynamic movement time series for $\beta = 10^{-5}$.



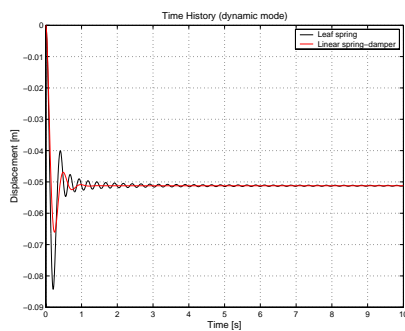
(b) Dynamic movement hysteresis for $\beta = 10^{-5}$.



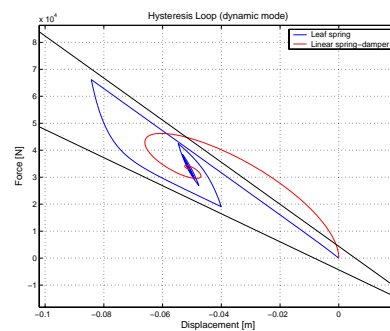
(c) Dynamic movement time series for $\beta = 10^{-3}$.



(d) Dynamic movement hysteresis for $\beta = 10^{-3}$.



(e) Dynamic movement time series for $\beta = 5 \cdot 10^{-5}$.



(f) Dynamic movement hysteresis for $\beta = 5 \cdot 10^{-3}$.

Figure 5.9: Dynamic movement simulations for the standard leaf spring model.

5.3.2 Parabolic Leaf Spring

We keep the coefficient of friction to be $\mu = 0.13$. We figure the standard leaf springs yield an upper bound for what damping the parabolic springs can yield. This assumption comes about from the fact that the standard leaf spring experiences greater surface contact between leaves than the parabolic spring does.

The amplitude of the forcing function on the dry friction system is chosen to be *half* of the distance the car body falls as it settles under its own weight in the unloaded case analysis, and under its own weight plus cargo in the loaded case analysis. Furthermore, the spring stiffness is the piece-wise linear one illustrated in figure 5.5. The mass corresponds to one quarter of the mass of the car body and any freight loaded. With this information, we can work out the friction work performed by the system.

In having found the theoretical dry friction work our system should experience, we force our linear spring-damper mathematical model with an identical sinusoidal forcing function, and thus obtain a hysteresis loop. From this loop, the area calculated indicates the energy dissipated by the system. In that we know the stiffness, we tweak the damping of the system such that the theoretical friction work equals the energy dissipated by our model in one cycle. This is done both for a loaded car wagon, and an unloaded one, and in this way we have parameters for a complete spring-damper mathematical model for our parabolic spring.

In figures 5.10 and 5.11 we illustrate these hysteresis loops of our linear spring-damper model with the correct approximated damping values. The area of the ellipsoid traces indicate the energy dissipated per cycle, and match the friction work W_μ done by our simple dry friction system.

Thus the constants defined in table 5.1 along with the previously mentioned mathematical model (equation 5.1) for the parabolic spring yield our vertical spring suspension. Furthermore, d is fixed to be either d_{loaded} or d_{unloaded} depending on whether or not the wagon is fully loaded or not, respectively, to begin with.

$k_{\text{unsupplemented}}$	$0.65 \cdot 10^6$	[N m ⁻¹]
$k_{\text{supplemented}}$	$1.82 \cdot 10^6$	[N m ⁻¹]
d_{unloaded}	$34.440 \cdot 10^3$	[N m ⁻¹ s]
d_{loaded}	$50.652 \cdot 10^3$	[N m ⁻¹ s]
F_0	$41.1 \cdot 10^3$	[N]
s_0	$62.9 \cdot 10^{-3}$	[m]

Table 5.1: Constants defining the piecewise linear spring-damper system modelling the parabolic spring.

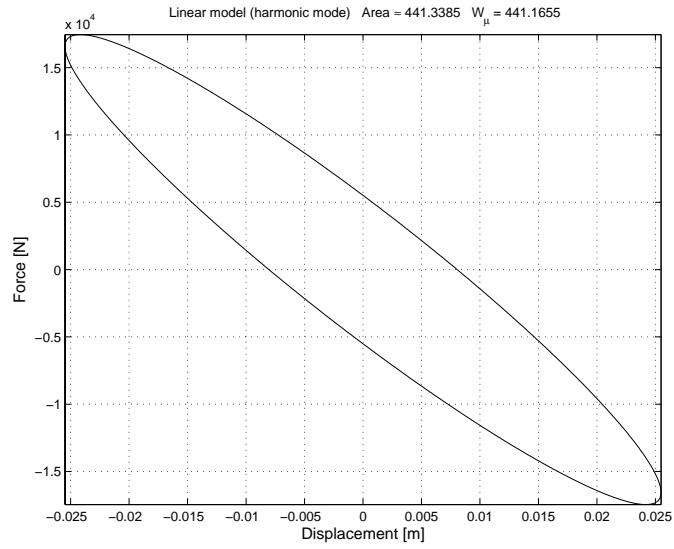


Figure 5.10: A diagram illustrating the force versus displacement our linear vertical suspension model yields with harmonic movement under empty cargo conditions.

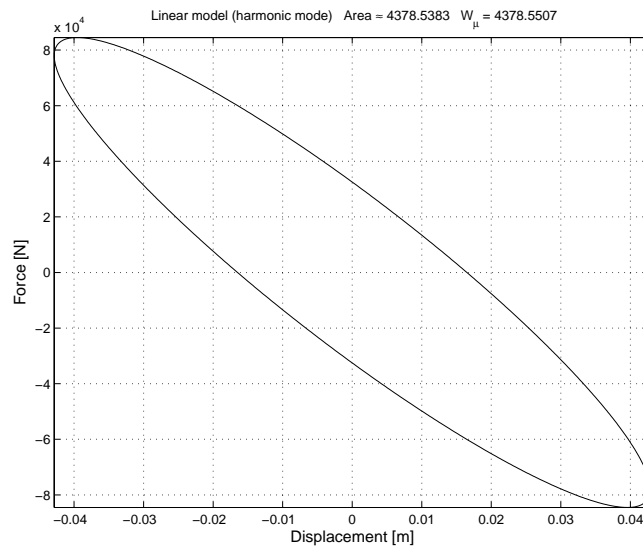


Figure 5.11: A diagram illustrating the force versus displacement our linear vertical suspension model yields with harmonic movement under loaded cargo conditions.

Chapter 6

Impact Model

In this chapter we present the mathematical model which corresponds to the structural elements of the freight wagon that prevent the wheelset from moving too much relative to the actual car body frame itself. Thus the model presented here only deals with the forces involved in the interaction between the wheelset and these structural elements. The actual dimensions and clearances that the wheelset enjoys are illustrated in figure 6.1.

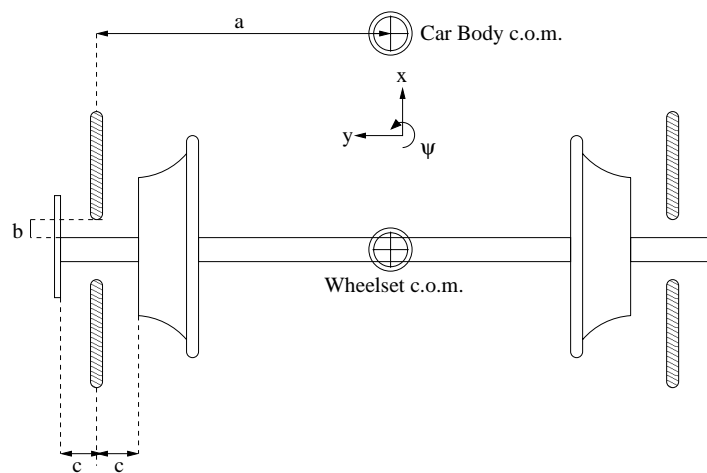


Figure 6.1: Dimensions and clearances for a single wheelset.

6.1 Degrees of Freedom

In our mathematical modelling of the constrained wheelset, we omit the vertical degree of freedom since we assume that in our simulations we will never experience the event in

which the leaf spring compresses to such a degree that the wheelset axle impacts with the car body frame. Furthermore, wheelset pitch is inconsequential for the behaviour of our wheelset in this case. Wheelset roll is also considered to be too small to be of importance. Therefore we have the following degrees of freedom.

x : Wheelset longitudinal

y : Wheelset lateral

ψ : Wheelset yaw

6.2 Mathematical Model

Figures that illustrate the forces on our mathematical model are shown in figures 6.2 and 6.3. From these figures we can determine the equations of motion for our system, based on Newton's second law. The coordinate system for this model can be taken to be (X_r, Y_r, Z_r) , the rail coordinate system. Keep in mind that the lateral and longitudinal displacements of the center of mass of the wheelset will be known as x_d and y_d in this chapter.

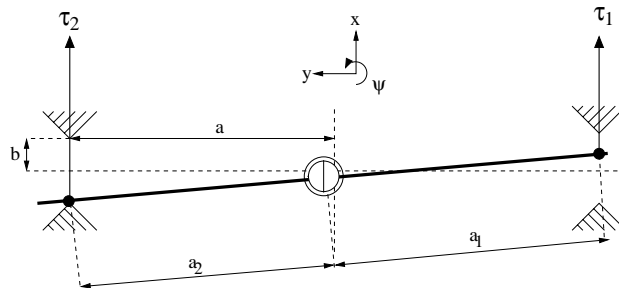


Figure 6.2: Forces and dimensions concerning longitudinal impacts.

The values a_1 and a_2 are given by:

$$a_1 = \frac{a + y_d}{\cos(\psi)}$$

$$a_2 = \frac{a - y_d}{\cos(\psi)}$$

6.2.1 Impact

The forces that arise from impact, τ , come from what we model as linear springs which only exert their restoring force once the wheelset comes into contact with the freight

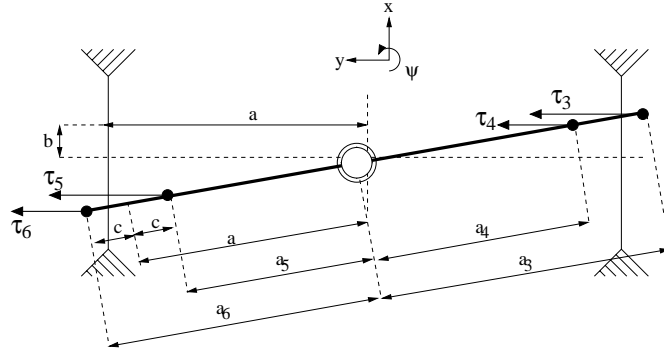


Figure 6.3: Forces and dimensions concerning lateral impacts.

wagon structure. Furthermore, these forces are directed in parallel with the unit vectors that define the x and y coordinates in our mathematical model. These forces are also considered to exist in a plane parallel to the ground plane that the rails rest on.

Thus we need to know the longitudinal penetration of the wheelset that gives rise to forces τ_1 and τ_2 . The positions of the penetrating wheelset points will be known as $p_{x,1}$ and $p_{x,2}$, respectively, while actual penetration will be calculated later. The values $p_{x,1}$ and $p_{x,2}$ are determined by:

$$\begin{aligned} p_{x,1} &= a_1 \sin(\psi) + x_d \\ p_{x,2} &= -a_2 \sin(\psi) + x_d \end{aligned}$$

For τ_3 through τ_6 we will need to know the lateral penetration of the wheelset into the local structure, and the corresponding wheelset penetrating positions will be known as $p_{y,3}$ through $p_{y,6}$. The values $p_{y,3}$ to $p_{y,6}$ are determined by:

$$\begin{aligned} p_{y,3} &= -a_3 \cos(\psi) + y_d \\ p_{y,4} &= -a_4 \cos(\psi) + y_d \\ p_{y,5} &= a_5 \cos(\psi) + y_d \\ p_{y,6} &= a_6 \cos(\psi) + y_d \end{aligned}$$

where a_3 to a_6 are the absolute distances from the center of mass of the wheelset to the impact points.

$$\begin{aligned} a_3 &= a + c \\ a_4 &= a - c \\ a_5 &= a - c \\ a_6 &= a + c \end{aligned}$$

6.2.2 Equations

The physical equations of motion of a wheelset restricted by guidances, are as follows:

$$\begin{aligned} m_w \ddot{x} &= \tau_1 + \tau_2 \\ m_w \ddot{y} &= \tau_3 + \tau_4 + \tau_5 + \tau_6 \\ I_{wz} \ddot{\psi} &= a_1 \tau_1 \cos(\psi) - a_2 \tau_2 \cos(\psi) + a_3 \tau_3 \sin(\psi) + a_4 \tau_4 \sin(\psi) - a_5 \tau_5 \sin(\psi) - a_6 \tau_6 \sin(\psi) \end{aligned}$$

$$\begin{aligned} y_1 &= x \\ y_2 &= \dot{x} \\ y_3 &= y \\ y_4 &= \dot{y} \\ y_5 &= \psi \\ y_6 &= \dot{\psi} \end{aligned}$$

In order to achieve a system of first order ordinary differential equations, we differentiate the previous values, and obtain the following system.

$$\begin{aligned} \dot{y}_1 &= y_2 \\ \dot{y}_2 &= \frac{\tau_1 + \tau_2}{m_w} \\ \dot{y}_3 &= y_4 \\ \dot{y}_4 &= \frac{\tau_3 + \tau_4 + \tau_5 + \tau_6}{m_w} \\ \dot{y}_5 &= y_6 \\ \dot{y}_6 &= \frac{a_1 \tau_1 \cos(y_5) - a_2 \tau_2 \cos(y_5) + a_3 \tau_3 \sin(y_5) + a_4 \tau_4 \sin(y_5) - a_5 \tau_5 \sin(y_5) - a_6 \tau_6 \sin(y_5)}{I_{wz}} \end{aligned}$$

6.2.3 Forces

In order to determine the forces τ that arise under impact, we have following conditional formulas where k represents a linear spring constant. Under actual simulation, the lateral and longitudinal stiffnesses will vary.

$$\begin{aligned} \tau_1 &= \begin{cases} -k(p_{x,1} + b) & \text{if } p_{x,1} < -b \\ -k(p_{x,1} - b) & \text{if } p_{x,1} > b \\ 0 & \text{otherwise} \end{cases} \\ \tau_2 &= \begin{cases} -k(p_{x,2} + b) & \text{if } p_{x,2} < -b \\ -k(p_{x,2} - b) & \text{if } p_{x,2} > b \\ 0 & \text{otherwise} \end{cases} \\ \tau_3 &= \begin{cases} -k(p_{y,3} + a) & \text{if } p_{y,3} > -a \\ 0 & \text{otherwise} \end{cases} \end{aligned}$$

$$\tau_4 = \begin{cases} -k(p_{y,4} + a) & \text{if } p_{y,4} < -a \\ 0 & \text{otherwise} \end{cases}$$

$$\tau_5 = \begin{cases} -k(p_{y,5} - a) & \text{if } p_{y,5} > a \\ 0 & \text{otherwise} \end{cases}$$

$$\tau_6 = \begin{cases} -k(p_{y,6} - a) & \text{if } p_{y,6} < a \\ 0 & \text{otherwise} \end{cases}$$

6.3 Results

The system described in this chapter was modelled in `MatLab` (see `impactode.m` in the source code). An interesting aspect of the introduction of the guidance constraints to the wheelset is that it introduces nonlinearity that could lead to the presence of chaotic behaviour in our freight wagon model. A characteristic property of chaotic systems is that they exhibit sensitivity in the initial condition. In the following we will investigate whether or not the impact model has this characteristic property. In table 6.1 we have shown the parameters used in the first numerical example. The magnitude of both clearances, i.e. b and c , are not realistic, however, they serve to exaggerate the sensitivity of the system for clarity.

Description	Value
Wheelset mass	1022 kg
Wheelset yaw inertia	678 kg m ²
Longitudinal guidance stiffness	10 ¹¹ N m ⁻¹
Lateral guidance stiffness	1.5 · 10 ⁶ N m ⁻¹
a	1.074 m
b	0.5 m
c	0.2 m

Table 6.1: Parameters used in the sensitivity test.

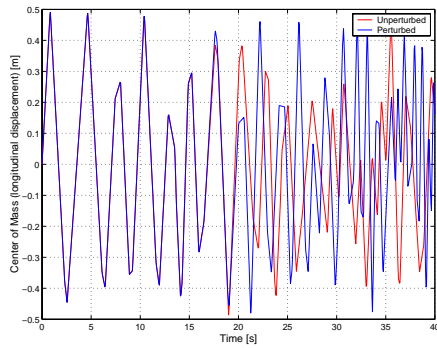
The numerical solution was found with the `MatLab` solver `ode15s`, with absolute and relative tolerances of 10⁻⁸, and the following initial conditions:

$$\mathbf{Y}_{0,1} = [0, 0.6, 0, 0.3, 0, 0]^T \quad (\text{Unperturbed})$$

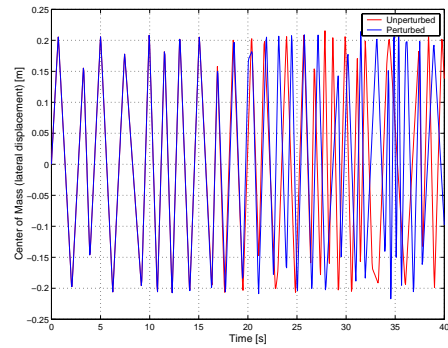
$$\mathbf{Y}_{0,2} = \mathbf{Y}_{0,1} + [0, 0, 10^{-6}, 0, 0, 0]^T \quad (\text{Perturbed})$$

The result is presented in figure 6.4. It is seen that even though the solution start out in almost identical positions, the asymptotic solution is completely different.

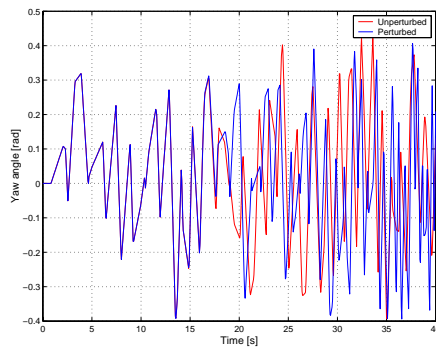
The second numerical example is with the true clearance dimensions, i.e. $b = 0.0225$ m and $c = 0.02$ m. We expect a similar result as in the first numerical example, however, there is a slightly difference as seen in figure 6.5. The sensitivity is clearly visible in the longitudinal displacement as well as the yaw motion, but the lateral displacement is almost the same even after a long time.



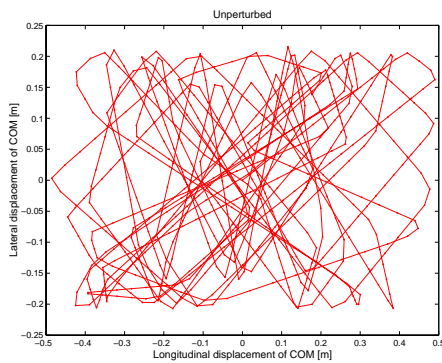
(a) Longitudinal.



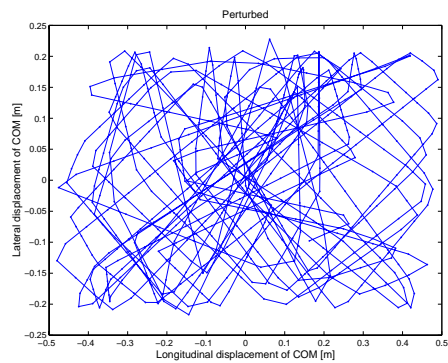
(b) Lateral.



(c) Yaw.

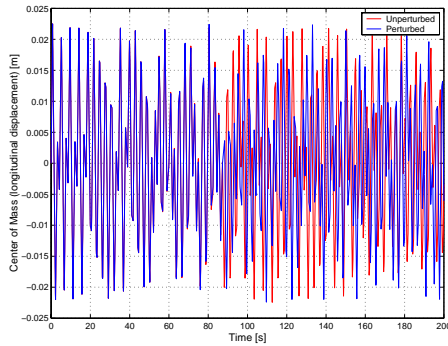


(d) Trace of the center of mass in the test with the unperturbed initial condition.

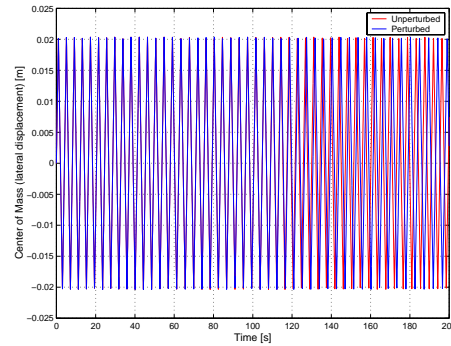


(e) Trace of the center of mass in the test with the perturbed initial condition.

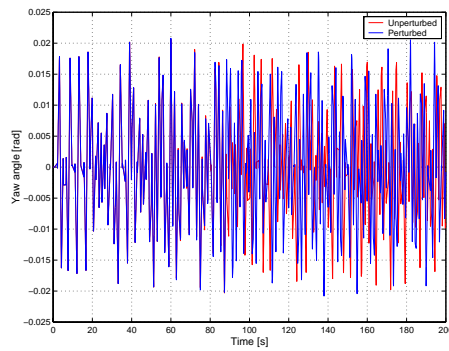
Figure 6.4: Solution of the impact model with exaggerated clearances illustrating the sensitivity in the initial condition.



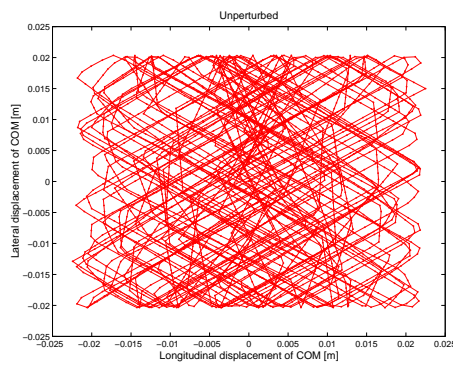
(a) Longitudinal.



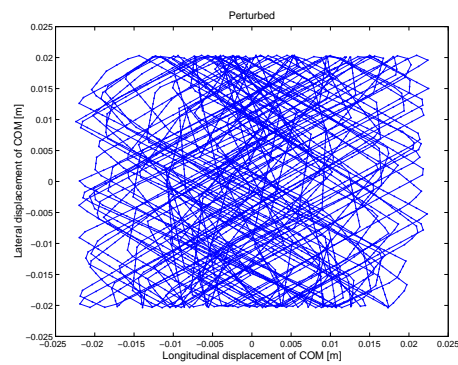
(b) Lateral.



(c) Yaw.



(d) Unperturbed.



(e) Perturbed.

Figure 6.5: Solution of the impact model with true clearance dimensions, i.e. $b = 0.0225$ m and $c = 0.02$ m. The sensitivity in the initial condition is seen in the longitudinal displacement and yaw motion, however, the lateral displacement is more or less the same.

Chapter 7

Freight Wagon Inertia

This chapter deals with calculating the moments of inertia of the Hbbills 311 freight wagon, either empty or loaded. Since explicit data on the moments of inertia were not readily available, these had to be calculated from a table detailing the elements on a Hbbills 311 freight wagon.

7.1 Empty Freight Wagon

Table 7.1 details the quantity and mass of the different elements which we have considered to be a significant part of the empty Hbbills 311 freight wagon.

The center of mass is defined as

$$\begin{aligned}\mathbf{r}_C &= \frac{1}{M} \sum_i m_i \mathbf{r}_i && \text{(discrete)} \\ \mathbf{r}_C &= \frac{1}{M} \int \mathbf{r} \rho \, dS = \frac{1}{A} \int \mathbf{r} \, dS && \text{(continuous)}\end{aligned}$$

The moment of inertia is defined as

$$\begin{aligned}I_z &= \sum_i m_i R_i^2 && \text{(discrete)} \\ I_z &= \int R^2 \rho \, dS = \frac{M}{A} \int R^2 \, dS && \text{(continuous)}\end{aligned}$$

where R is the distance to the z -axis.

We use **Maple** to calculate both the center of mass as well as moments of inertia, and the **Maple** code is given in appendix G. Results are the following:

$$\mathbf{r}_C = (x_0, y_0, z_0) = (8.005 \text{ m}, 1.450 \text{ m}, 0.802 \text{ m})$$

and

$$\begin{aligned} I_{\text{roll}} &= 32675 \text{ kg} \cdot \text{m}^2 \\ I_{\text{yaw}} &= 413097 \text{ kg} \cdot \text{m}^2 \end{aligned}$$

The coordinate system used is shown in figure 7.1. In this figure, I_{roll} and I_{yaw} are the moments of inertia with respect to the lines l_1 and l_2 , respectively.

7.2 Adding Freight

In adding freight, we add a neat 20 tons to the wagon, and assume that the freight is evenly distributed over the floor. This means that the height of the freight measured from the floor is

$$\rho = \frac{M_{\text{freight}}}{h \cdot A} \quad \Rightarrow \quad h = \frac{M_{\text{freight}}}{\rho \cdot d_8 \cdot d_9} < d_4 \approx 2.35 \text{ m}$$

The center of mass of the car body is now placed at

$$\mathbf{r}_C = \left(x_0, y_0, \frac{z_0 M_0 + (\frac{1}{2}h + d_3) M_{\text{freight}}}{M_0 + M_{\text{freight}}} \right)$$

where $d_3 \approx 0.265 \text{ m}$ is the distance from the underframe to the floor. We repeat the calculations for I_{roll} and I_{yaw} with respect to the new center of mass of the car body through the use of Steiner's theorem.

In the dynamic simulations presented later in this report we have used four different types of freight summarized in table 7.2 and 7.3. We have chosen these types in order to be able to simulate what happens when the center of mass of the car body is raised or lowered. Furthermore, we are interested in discussing the difference in the dynamic behaviour between an empty wagon and a loaded wagon.

Element	#	Mass [kg] (each)	Mass [kg] (total)
Underframe	1	6395	6395
Floor	1	662	662
Front wall	2	550	1100
Roof	1	1339	1339
Partition	4	244	976
Sliding panel	2	1024	2048
Rail for sliding panel	2	132	264
Buffer	4	149	596
Center column	1	183	183
Sum	-	-	13563

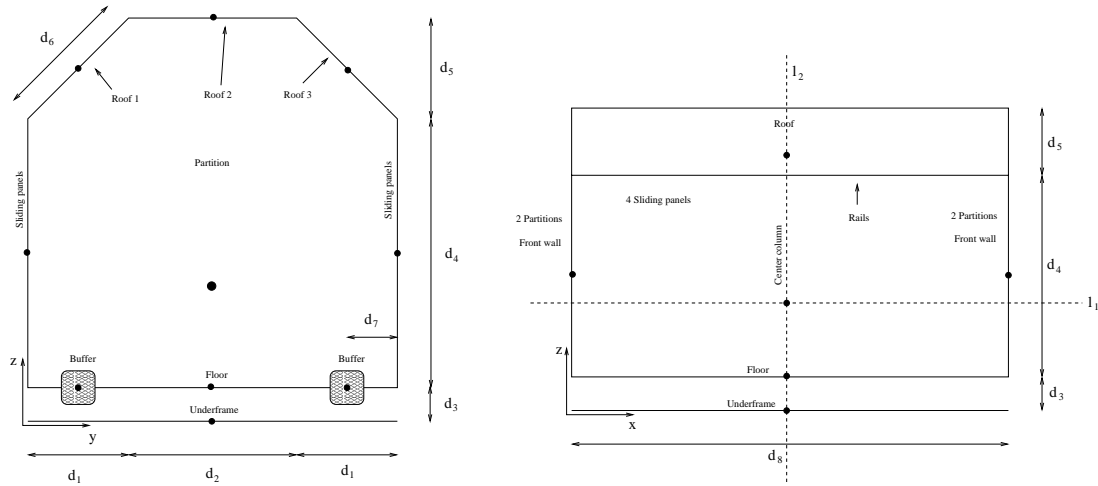
Table 7.1: Quantities and masses of different significant elements of a Hbbills 311 freight wagon.

Freight	Mass [kg]	Density [kg/m ³]
H ₂ O	20000	1000.0
Au	20000	19300.0
Packed	20000	183.3

Table 7.2: A few characteristics of chosen freight compositions.

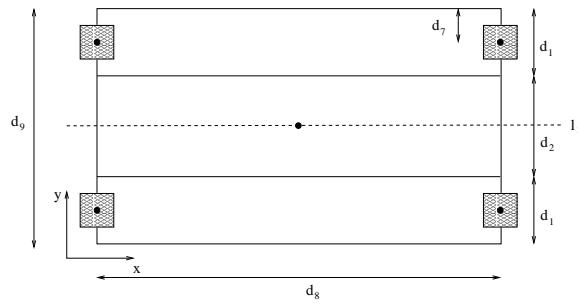
Freight	COM of car body with freight [m]	I_{roll} [kg · m ²]	I_{yaw} [kg · m ²]
Empty	(8.005, 1.450, 0.802)	32675	413097
H ₂ O	(8.005, 1.450, 0.610)	48428	854314
Au	(8.005, 1.450, 0.489)	49893	854314
Packed	(8.005, 1.450, 1.182)	58014	854314

Table 7.3: Center of mass of the whole car body and freight, as well as moments of inertia for different freights.



(a) Front view.

(b) Side view.



(c) Top view.

Figure 7.1: Model pictures used in the determination of the moments of inertia.

Chapter 8

Dry Friction Dynamics

In this section we will briefly look into the dynamics of the basic dry friction element that is used as a model for the UIC link suspension in the lateral and longitudinal directions. The purpose of this is to get some insight in the properties of dry friction, because it might not be that easy to extract this information when analyzing the complete model.

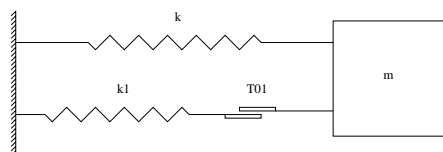


Figure 8.1: Dry friction model under investigation.

We consider a mass connected to a fixed base through the dry friction element (see figure 8.1). This element is comprised of a main spring, with stiffness k , and a secondary spring attached to a dry friction slider. This dry friction slider is central to the dynamics of the element, in that it changes the whole stiffness of the system, depending on whether or not the slider sticks, or is slipping. When sticking, the stiffness of the element is $k + k_1$, and when sliding, only the main spring is left to govern dynamics, and the stiffness is only k .

The dry friction slider can be visualized as two plates pressed against each other, of which can maximally sustain a shearing force equal to T_0 before static friction is overcome and the slider begins to slip. Important to note is that in our model here, and in the freight train itself, we do not distinguish between static and kinetic friction coefficients (figure F.2(a) in appendix validates this assumption). This results in that when sliding, the slider element delivers a maximum force T_0 .

A numerical experiment is performed as follows. For $t < 0$ the mass is at rest, all spring forces are zero, no shear force exists in the slider, and this position defines the

“true” origin of our coordinate system. At $t = 0$ we pull out the mass to the position x_0 and release.

The time history of the simulation is shown in figure 8.2. In the first part of the figure we see damped oscillations. What is characteristic of systems exhibiting dry friction, is that the envelope of the damping motion is linear, and not exponentially decaying, for example.

After a while this damping ceases and the mass oscillates harmonically. This result is not surprising, because the restoring force of the spring connected to the dry friction slider is limited by a threshold force corresponding to the static coefficient of friction. The initial condition is so large that this limit is exceeded, meaning that the dry friction plates begins to slide. As soon as the mass reaches a velocity of 0, the relative velocity in the dry friction slider also reaches 0, and the sliders stick immediately. This stick remains until the displacement of the mass becomes great enough that the force yielded from the spring with stiffness k_1 yet again overcomes the static friction threshold of the slider. This repeated sliding/sticking process yields a damping effect.

Ultimately, when the oscillations are damped to a certain magnitude the dry friction plates will stick permanently since the shear force exerted on the dry friction plates no longer exceeds the threshold mentioned above. At that point, the motion of the mass will appear as pure harmonic motion.

An interesting observation is that this harmonic motion need not necessarily oscillate symmetrically about the origin. This is evident in figure 8.4. This is because that from the system’s true origin, where all spring forces are zero, a band exists about this value where the system can behave as having a new origin upon reaching harmonic motion. This is because as the slider slips when forces exceed its threshold, the origin for the slider spring (stiffness k_1) *moves*. This movement results in a bit of force coming from the slider spring, where before it was 0 at the system’s true origin, it now no longer is so, and thus shifts the center point of oscillation of the collected system.

This behaviour is confirmed in our mathematical model in figure 8.4, as well as in experimental data from Poland. It was previously mentioned how we zero-shifted data in order to more accurately ascertain parameters for the UIC suspension. This behaviour, as we shall see, also emerges in the simulation of the full freight wagon.

An interesting figure of the dynamics of the simple dry friction model is given in figure 8.5. We here see a three dimensional trace of the state of our model. This trace is shown as a time history in figure 8.2, and a hysteresis loop diagram in figure 8.3. We can clearly see the dry friction force is limited by T_0 , since the force plateaus under too great displacement. The figure gives a good overview of the dry friction force as our mass moves from damped motion to harmonic motion.

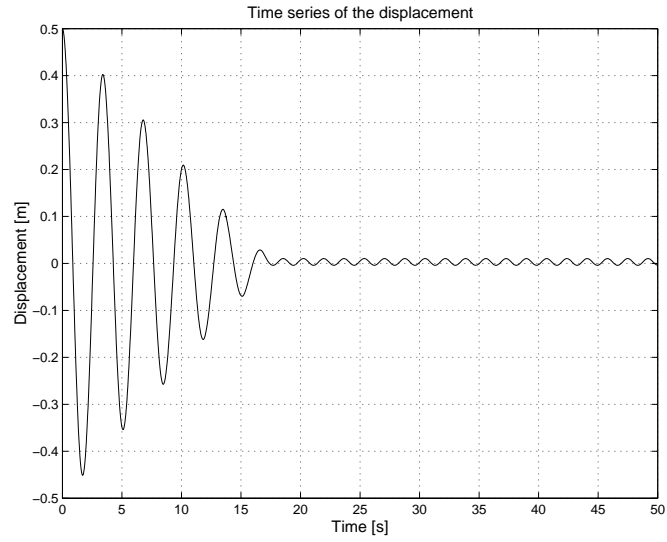


Figure 8.2: Time history for the experiment showing the damping effect of the dry friction.

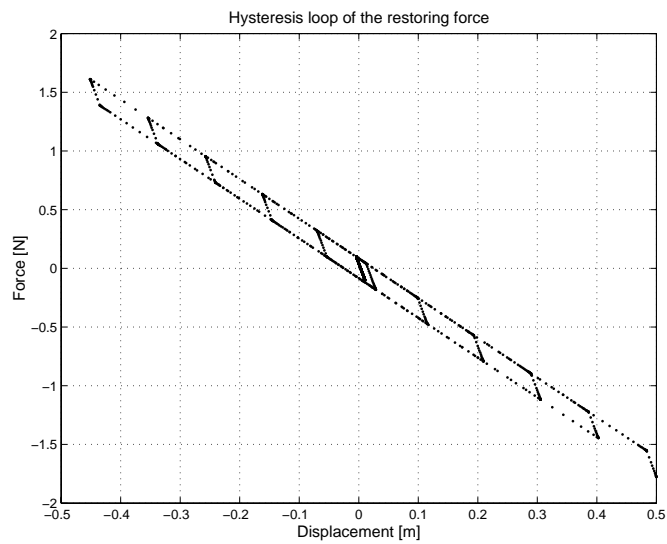


Figure 8.3: Complete hysteresis loop of the experiment.

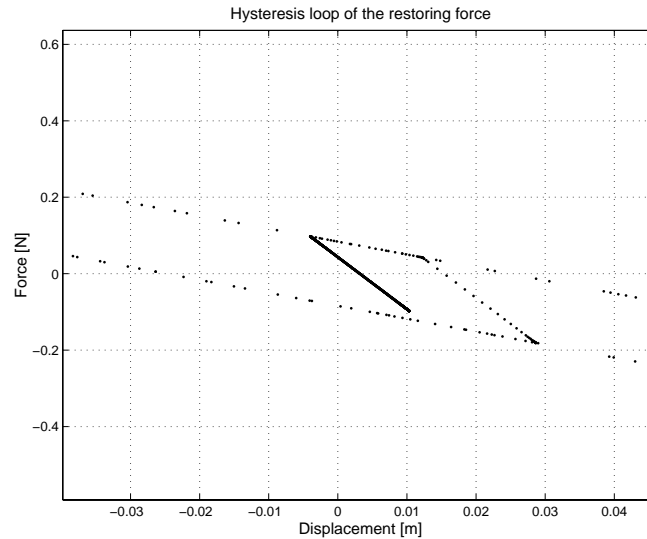


Figure 8.4: Zoomed view of the hysteresis loop. The oscillations is clearly not around zero.

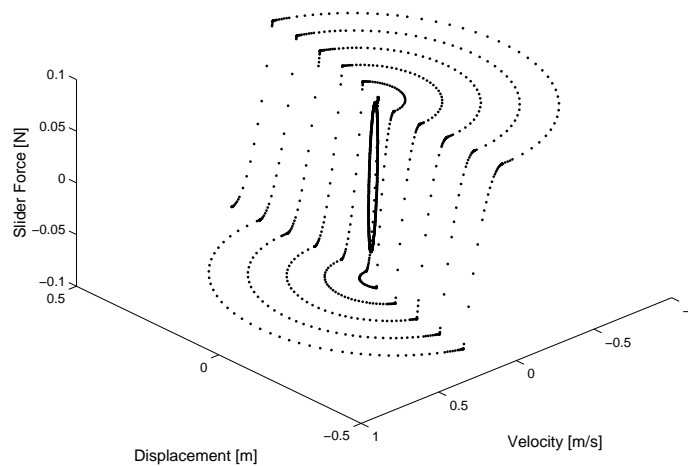


Figure 8.5: This figure shows the dry friction force as a function of the displacement and velocity of the mass. By imagining the slider force versus velocity projection one can see the Coulomb friction relationship between the friction force and sliding velocity. Furthermore, this figure gives an illustration of damping that the mass is exposed to each time dry friction plates slides.

Chapter 9

Numerical Approach

9.1 Implementation

The implementation is done in C++ for three reasons. First, executing programs in C++ can be done efficiently compared to other programming languages such as MatLab and Java. Secondly, C++ allow object oriented programming yielding a better program structure. Thirdly, the numerical solver we were provided with is also programmed in C++, and thus applying the solver to our model is straight forward. The complete program is found in the source code supplement to this thesis.

The model is “built” in the file `FreightWagon.cpp` and is a composition of six objects. These objects are created through six C++ classes also listed in the source code. A short description of the classes are now given.

- **CarBody.** Implementation of the car body model. This object delivers the differential equations regarding the car body given the magnitude of the suspension and impact forces.
- **Impact.** Implementation of the impact model. Through the interface of this object we compute the impact forces given the current position of the wheelsets and the car body.
- **Parameters.** Object through which it is possible to read in parameters from data files.
- **Suspension.** Implementation of the linear, parabolic and leaf spring model. Through the interface of this object we compute the suspension forces given the current position of the wheelsets and the car body.
- **WheelRailContact.** Implementation of the wheel-rail contact model. Through the interface of this object we compute the contact forces between the wheel and rail for one of the wheelsets given the current position of the specific wheelset.

- **Wheelset.** Implementation of the wheelset model. This object delivers the differential equations regarding the wheelset given the magnitude of the suspension, impact and contact forces.

9.2 SDIRK

In the treatment of our problem, we employed the numerical solver SDIRK, as provided by prof. Per Grove Thomsen¹. This solver was employed by [11] and partially by [4]. SDIRK belongs to the Runge-Kutta family of solvers, and more precisely, the singly diagonally implicit Runge-Kutta solvers (which is the origin of the acronym SDIRK). As such, it is an efficient solver for stiff problems, and requires the specification of the Jacobi matrix of our system, as well as the right hand side of our system of first order ODEs.

9.3 Jacobi Matrix

Since we have to calculate the Jacobi matrix of the complete system, we investigate this step here. It is very important from an efficiency point of view to optimize the calculation of the Jacobi matrix in order to minimize computer time during simulations. The reason calculation of the Jacobi matrix is time consuming is that in each integration step the numerical integrator requires several approximations of the system in order to approximate the next solution point. In that the Jacobi matrix has numerous elements, multiple calculations of its elements for every time step translates into a heavy computational load.

The definition of the (i, j) 'th element in the Jacobi matrix is

$$J_{ij} = \frac{\partial f_i}{\partial y_j} \quad (9.1)$$

Some of the elements we have to evaluate numerically because the forces governing the motion of the vehicle are determined by non analytic functions. A naïve and extremely inefficient method is to go through all elements in the Jacobi matrix and numerically estimate the derivative. This is inefficient because the Jacobi matrix is a sparse matrix, meaning that most of the entries are zero. In figures 9.1(a), 9.1(b) and 9.1(c) we have illustrated the sparsity pattern of the Jacobi matrix for our system using suspension types 1, 2 and 3, respectively. However, to find the nonzero entries we have to look into the dependencies in each equation in the complete system for the corresponding suspension type. In section 9.4 these dependencies are listed.

¹Institute for Informatics and Mathematical Modelling, Technical University of Denmark.

By knowing the dependencies we can efficiently evaluate the Jacobi matrix in the following manner. We characterise each element in the Jacobi matrix by how the value of the element is provided. We distinguish between the entries that are zero, one and those we have to approximate numerically. This characterization is done before the simulation starts, meaning that the only time consuming part in the determination of the Jacobi matrix under the simulation is the special entries that we need to approximate numerically, which only form a minor part of the complete matrix.

The numerical approximation to the derivative in equation (9.1) is done by a central difference estimate. To make this estimate we calculate the function value of f_i for a positive and negative perturbation of the variable y_j . The central difference is then formed by

$$\frac{\partial f_i}{\partial y_j} \approx \frac{f_{i,+} - f_{i,-}}{2\delta} \quad (9.2)$$

where δ is the perturbation.

To make this numerical approximation procedure efficient, with respect to processing time, we proceed columnwise² through the Jacobi matrix and follow the scheme:

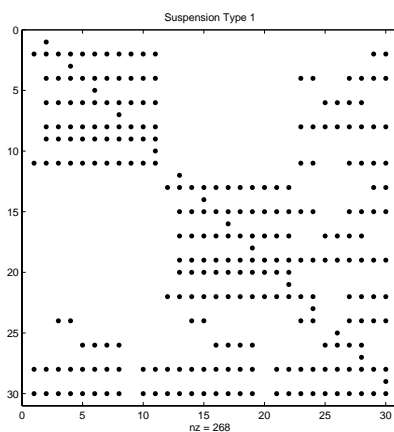
1. Perturb y_j positively by δ
2. Calculate the interacting forces
3. Calculate and store all $f_{i,+}$
4. Perturb y_j negatively by δ
5. Calculate the interacting forces
6. Calculate and store all $f_{i,-}$
7. Calculate the central difference by equation (9.2)

This is advantageous because we only have to determine the interacting forces between the elements in the freight wagon twice for each y_j .

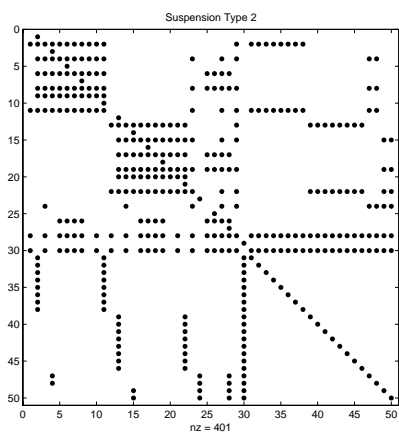
A consequence of our central differences strategy is that elements are perturbed with a constant value throughout simulation. Since scale between Jacobi matrix elements differ greatly, we optimized roughly the perturbation magnitude with respect to what Jacobi matrix element we were estimating, but this magnitude remained unchanged with time. Since the scale of Jacobi elements change with respect to themselves over time, poor estimation of certain elements can happen, with the result of the simulation hanging. A desirable strategy would be a Jacobi matrix estimator that optimizes the magnitude of perturbation, much like `numjac` can do for `MatLab` implemented systems.

²Programming language specific optimization. Fortran would be optimized to proceed row by row.

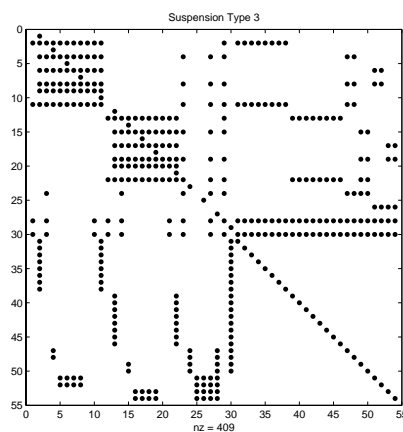
This may have enabled us to simulate without much user intervention to overcome hung simulations. Ultimately, we did not have the time to experiment and develop such an efficient numerical Jacobi matrix estimator.



(a) Suspension type 1. 30×30 .



(b) Suspension type 2. 50×50 .



(c) Suspension type 3. 54×54 .

Figure 9.1: Non-zero elements for Jacobi matrices using suspension types (a) 1, (b) 2, and (c) 3.

9.4 Dependencies

9.4.1 Front Wheelset

The calculation of the contact forces

$$C_{lx}^r, C_{rx}^r, C_{ly}^r, C_{ry}^r, C_{lz}^r, C_{rz}^r, C_{lx}^w, C_{rx}^w, C_{ly}^w, C_{ry}^w, C_{lz}^w, C_{rz}^w$$

is a function of

$$f(y_2, y_3, y_4, y_5, y_6, y_7, y_8, y_9, y_{10}, y_{11})$$

We write this dependency as follows

$$\left| \begin{array}{l} C_{lx}^r, C_{rx}^r, C_{ly}^r, C_{ry}^r, C_{lz}^r, C_{rz}^r, C_{lx}^w, C_{rx}^w, C_{ly}^w, C_{ry}^w, C_{lz}^w, C_{rz}^w \\ f(y_{2 \rightarrow 11}) \end{array} \right.$$

Furthermore, we have

S_{lx}^r, S_{rx}^r $f(y_1, y_2, y_{10}, y_{11}, y_{29}, y_{30})$ $f(y_1, y_{10}, y_{29}, y_{31 \rightarrow 38})$ $f(y_1, y_{10}, y_{29}, y_{31 \rightarrow 38})$	Suspension type 1 Suspension type 2 Suspension type 3	
S_{ly}^r, S_{ry}^r $f(y_3, y_4, y_{23}, y_{24}, y_{27 \rightarrow 30})$ $f(y_3, y_{23}, y_{27}, y_{29}, y_{47}, y_{48})$ $f(y_3, y_{23}, y_{27}, y_{29}, y_{47}, y_{48})$	Suspension type 1 Suspension type 2 Suspension type 3	
S_{lz}^r, S_{rz}^r $f(y_{5 \rightarrow 8}, y_{25 \rightarrow 28})$ $f(y_{5 \rightarrow 8}, y_{25 \rightarrow 28})$ $f(y_{51}, y_{52})$	Suspension type 1 Suspension type 2 Suspension type 3	
S_{lx}^w, S_{rx}^w $f(y_{1 \rightarrow 4}, y_{10}, y_{11}, y_{23}, y_{24}, y_{27 \rightarrow 30})$ $f(y_1, y_3, y_{10}, y_{23}, y_{27}, y_{29}, y_{31 \rightarrow 38}, y_{47}, y_{48})$ $f(y_1, y_3, y_{10}, y_{23}, y_{27}, y_{29}, y_{31 \rightarrow 38}, y_{47}, y_{48})$	Suspension type 1 Suspension type 2 Suspension type 3	
S_{ly}^w, S_{ry}^w $f(y_{1 \rightarrow 8}, y_{10}, y_{11}, y_{23 \rightarrow 30})$ $f(y_1, y_3, y_{5 \rightarrow 8}, y_{10}, y_{23}, y_{25 \rightarrow 29}, y_{31 \rightarrow 38}, y_{47}, y_{48})$ $f(y_1, y_3, y_7, y_{10}, y_{23}, y_{27}, y_{29}, y_{31 \rightarrow 38}, y_{47}, y_{48}, y_{51}, y_{52})$	Suspension type 1 Suspension type 2 Suspension type 3	
S_{lz}^w, S_{rz}^w $f(y_{3 \rightarrow 8}, y_{23 \rightarrow 30})$ $f(y_3, y_{5 \rightarrow 8}, y_{23}, y_{25 \rightarrow 29}, y_{47}, y_{48})$ $f(y_3, y_7, y_{23}, y_{27}, y_{29}, y_{47}, y_{48}, y_{51}, y_{52})$	Suspension type 1 Suspension type 2 Suspension type 3	
$\delta_{lx}^r, \delta_{rx}^r$ $f(y_1, y_{10}, y_{29})$	$\delta_{ly}^r, \delta_{ry}^r$ $f(y_3, y_{23}, y_{27}, y_{29})$	$\delta_{lz}^r, \delta_{rz}^r$ 0
$\delta_{lx}^w, \delta_{rx}^w$ $f(y_1, y_3, y_{10}, y_{23}, y_{27}, y_{29})$	$\delta_{ly}^w, \delta_{ry}^w$ $f(y_1, y_3, y_7, y_{10}, y_{23}, y_{27}, y_{29})$	$\delta_{lz}^w, \delta_{rz}^w$ $f(y_3, y_7, y_{23}, y_{27}, y_{29})$

9.4.2 Rear Wheelset

For the rear wheelset we have the following dependencies.

$$\begin{array}{l}
 \left| \begin{array}{l} C_{lx}^r, C_{rx}^r, C_{ly}^r, C_{ry}^r, C_{lz}^r, C_{rz}^r, C_{lx}^w, C_{rx}^w, C_{ly}^w, C_{ry}^w, C_{lz}^w, C_{rz}^w \\ f(y_{13 \rightarrow 22}) \end{array} \right. \\
 \\
 \left| \begin{array}{l} S_{lx}^r, S_{rx}^r \\ f(y_{12}, y_{13}, y_{21}, y_{22}, y_{29}, y_{30}) \\ f(y_{12}, y_{21}, y_{29}, y_{39 \rightarrow 46}) \\ f(y_{12}, y_{21}, y_{29}, y_{39 \rightarrow 46}) \end{array} \right. \begin{array}{l} \text{Suspension type 1} \\ \text{Suspension type 2} \\ \text{Suspension type 3} \end{array} \\
 \\
 \left| \begin{array}{l} S_{ly}^r, S_{ry}^r \\ f(y_{14}, y_{15}, y_{23}, y_{24}, y_{27 \rightarrow 30}) \\ f(y_{14}, y_{23}, y_{27}, y_{29}, y_{49}, y_{50}) \\ f(y_{14}, y_{23}, y_{27}, y_{29}, y_{49}, y_{50}) \end{array} \right. \begin{array}{l} \text{Suspension type 1} \\ \text{Suspension type 2} \\ \text{Suspension type 3} \end{array} \\
 \\
 \left| \begin{array}{l} S_{lz}^r, S_{rz}^r \\ f(y_{16 \rightarrow 19}, y_{25 \rightarrow 28}) \\ f(y_{16 \rightarrow 19}, y_{25 \rightarrow 28}) \\ f(y_{53}, y_{54}) \end{array} \right. \begin{array}{l} \text{Suspension type 1} \\ \text{Suspension type 2} \\ \text{Suspension type 3} \end{array} \\
 \\
 \left| \begin{array}{l} S_{lx}^w, S_{rx}^w \\ f(y_{12 \rightarrow 15}, y_{21 \rightarrow 24}, y_{27 \rightarrow 30}) \\ f(y_{12}, y_{14}, y_{21}, y_{23}, y_{27}, y_{29}, y_{39 \rightarrow 46}, y_{49}, y_{50}) \\ f(y_{12}, y_{14}, y_{21}, y_{23}, y_{27}, y_{29}, y_{39 \rightarrow 46}, y_{49}, y_{50}) \end{array} \right. \begin{array}{l} \text{Suspension type 1} \\ \text{Suspension type 2} \\ \text{Suspension type 3} \end{array} \\
 \\
 \left| \begin{array}{l} S_{ly}^w, S_{ry}^w \\ f(y_{12 \rightarrow 19}, y_{21 \rightarrow 30}) \\ f(y_{12}, y_{14}, y_{16 \rightarrow 19}, y_{21}, y_{23}, y_{25 \rightarrow 29}, y_{39 \rightarrow 46}, y_{49}, y_{50}) \\ f(y_{12}, y_{14}, y_{18}, y_{21}, y_{23}, y_{27}, y_{29}, y_{39 \rightarrow 46}, y_{49}, y_{50}, y_{53}, y_{54}) \end{array} \right. \begin{array}{l} \text{Suspension type 1} \\ \text{Suspension type 2} \\ \text{Suspension type 3} \end{array} \\
 \\
 \left| \begin{array}{l} S_{lz}^w, S_{rz}^w \\ f(y_{14 \rightarrow 19}, y_{23 \rightarrow 30}) \\ f(y_{14}, y_{16 \rightarrow 19}, y_{23}, y_{25 \rightarrow 29}, y_{49}, y_{50}) \\ f(y_{14}, y_{18}, y_{23}, y_{27}, y_{29}, y_{49}, y_{50}, y_{53}, y_{54}) \end{array} \right. \begin{array}{l} \text{Suspension type 1} \\ \text{Suspension type 2} \\ \text{Suspension type 3} \end{array}
 \end{array}$$

$$\left| \begin{array}{l} \delta_{lx}^r, \delta_{rx}^r \\ f(y_{12}, y_{21}, y_{29}) \end{array} \right.$$

$$\left| \begin{array}{l} \delta_{ly}^r, \delta_{ry}^r \\ f(y_{14}, y_{23}, y_{27}, y_{29}) \end{array} \right.$$

$$\left| \begin{array}{l} \delta_{lz}^r, \delta_{rz}^r \\ 0 \end{array} \right.$$

$$\left| \begin{array}{l} \delta_{lx}^w, \delta_{rx}^w \\ f(y_{12}, y_{14}, y_{21}, y_{23}, y_{27}, y_{29}) \end{array} \right.$$

$$\left| \begin{array}{l} \delta_{ly}^w, \delta_{ry}^w \\ f(y_{12}, y_{14}, y_{18}, y_{21}, y_{23}, y_{27}, y_{29}) \end{array} \right.$$

$$\left| \begin{array}{l} \delta_{lz}^w, \delta_{rz}^w \\ f(y_{14}, y_{18}, y_{23}, y_{27}, y_{29}) \end{array} \right.$$

9.4.3 Car Body

For the car body the dependencies are found to be

$S_{flx}^r, S_{frrx}^r, S_{rlx}^r, S_{rrx}^r$ $f(y_1, y_2, y_{10 \rightarrow 13}, y_{21}, y_{22}, y_{29}, y_{30})$ $f(y_1, y_{10}, y_{12}, y_{21}, y_{29}, y_{31 \rightarrow 46})$ $f(y_1, y_{10}, y_{12}, y_{21}, y_{29}, y_{31 \rightarrow 46})$	Suspension type 1 Suspension type 2 Suspension type 3
$S_{fly}^r, S_{fry}^r, S_{rly}^r, S_{rry}^r$ $f(y_3, y_4, y_{14}, y_{15}, y_{23}, y_{24}, y_{27 \rightarrow 30})$ $f(y_3, y_{14}, y_{23}, y_{27}, y_{29}, y_{47 \rightarrow 50})$ $f(y_3, y_{14}, y_{23}, y_{27}, y_{29}, y_{47 \rightarrow 50})$	Suspension type 1 Suspension type 2 Suspension type 3
$S_{flz}^r, S_{frrz}^r, S_{rlz}^r, S_{rrz}^r$ $f(y_{5 \rightarrow 8}, y_{16 \rightarrow 19}, y_{25 \rightarrow 28})$ $f(y_{5 \rightarrow 8}, y_{16 \rightarrow 19}, y_{25 \rightarrow 28})$ $f(y_{51 \rightarrow 54})$	Suspension type 1 Suspension type 2 Suspension type 3
$S_{flx}^b, S_{frrx}^b, S_{rlx}^b, S_{rrx}^b$ $f(y_{1 \rightarrow 4}, y_{10 \rightarrow 15}, y_{21 \rightarrow 24}, y_{27 \rightarrow 30})$ $f(y_1, y_3, y_{10}, y_{12}, y_{14}, y_{21}, y_{23}, y_{27}, y_{29}, y_{31 \rightarrow 50})$ $f(y_1, y_3, y_{10}, y_{12}, y_{14}, y_{21}, y_{23}, y_{27}, y_{29}, y_{31 \rightarrow 50})$	Suspension type 1 Suspension type 2 Suspension type 3
$S_{fly}^b, S_{fry}^b, S_{rly}^b, S_{rry}^b$ $f(y_{1 \rightarrow 8}, y_{10 \rightarrow 19}, y_{21 \rightarrow 30})$ $f(y_1, y_3, y_{5 \rightarrow 8}, y_{10}, y_{12}, y_{14}, y_{16 \rightarrow 19}, y_{21}, y_{23}, y_{25 \rightarrow 29}, y_{31 \rightarrow 50})$ $f(y_1, y_3, y_{10}, y_{12}, y_{14}, y_{21}, y_{23}, y_{27}, y_{29}, y_{31 \rightarrow 54})$	Suspension type 1 Suspension type 2 Suspension type 3
$S_{flz}^b, S_{frrz}^b, S_{rlz}^b, S_{rrz}^b$ $f(y_{3 \rightarrow 8}, y_{14 \rightarrow 19}, y_{23 \rightarrow 30})$ $f(y_3, y_{5 \rightarrow 8}, y_{14}, y_{16 \rightarrow 19}, y_{23}, y_{25 \rightarrow 29}, y_{47 \rightarrow 50})$ $f(y_3, y_{14}, y_{23}, y_{27}, y_{29}, y_{47 \rightarrow 54})$	Suspension type 1 Suspension type 2 Suspension type 3
$\delta_{flx}^r, \delta_{frrx}^r, \delta_{rlx}^r, \delta_{rrx}^r$ $f(y_1, y_{10}, y_{12}, y_{21}, y_{29})$	$\delta_{fly}^r, \delta_{fry}^r, \delta_{rly}^r, \delta_{rry}^r$ $f(y_3, y_{14}, y_{23}, y_{27}, y_{29})$
$\delta_{flz}^r, \delta_{frrz}^r, \delta_{rlz}^r, \delta_{rrz}^r$ 0	$\delta_{flx}^b, \delta_{frrx}^b, \delta_{rlx}^b, \delta_{rrx}^b$ $f(y_1, y_3, y_{10}, y_{12}, y_{14}, y_{21}, y_{23}, y_{27}, y_{29})$
$\delta_{fly}^b, \delta_{fry}^b, \delta_{rly}^b, \delta_{rry}^b$ $f(y_1, y_3, y_{10}, y_{12}, y_{14}, y_{21}, y_{23}, y_{27}, y_{29})$	$\delta_{flz}^b, \delta_{frrz}^b, \delta_{rlz}^b, \delta_{rrz}^b$ $f(y_3, y_{14}, y_{23}, y_{27}, y_{29})$

9.4.4 Dry Friction Elements

$$\begin{aligned}
 \dot{y}_i &= f(y_2, y_{11}, y_{30}, y_i) & i &= 31 \dots 38 \\
 \dot{y}_i &= f(y_{13}, y_{22}, y_{30}, y_i) & i &= 39 \dots 46 \\
 \dot{y}_i &= f(y_4, y_{24}, y_{28}, y_{30}, y_i) & i &= 47, 48 \\
 \dot{y}_i &= f(y_{15}, y_{24}, y_{28}, y_{30}, y_i) & i &= 49, 50 \\
 \dot{y}_i &= f(y_{5 \rightarrow 8}, y_{25 \rightarrow 28}, y_i) & i &= 51, 52 \\
 \dot{y}_i &= f(y_{16 \rightarrow 19}, y_{25 \rightarrow 28}, y_i) & i &= 53, 54
 \end{aligned}$$

Chapter 10

Results

10.1 Method of Attack

In this chapter we present results from various simulations on our freight wagon under different conditions. This encompasses both suspension parameter sets, as well as different cargo conditions. The suspension setup in all cases was the model for the UIC links in longitudinal and lateral direction, whereas the parabolic spring model was used in the vertical direction. Fancher's model describing standard leaf springs was simulated, but we did not produce any meaningful results in that the extreme stiffness of the system lengthened simulation execution times significantly. The results were generated with the SDIRK solver using the `SC_PI`¹ step control option, as well as a maximal error tolerance of 10^{-6} .

We have generated bifurcation traces using the following algorithm:

1. Find stationary solution at a certain velocity v .
2. Simulate 5 or 10 seconds running at v .
3. Capture maximum amplitude over the last 3 seconds.
4. $v = v \pm 0.05$ m/s and goto 2.

We have used the bifurcation diagrams as a starting point for further analysis of the model. Thus, we first present bifurcation diagrams followed by specific simulations digesting the information from the diagrams. This is done for both suspension parameter sets. Finally, we do a frequency analysis capturing the main frequencies in the model.

¹SC_PI is short for Proportional-Integral step control.

10.2 Suspension Parameter Set 1

10.2.1 Critical Velocities

In figure 10.1(a) we show a bifurcation trace performed on an empty freight wagon. We started at 15 m/s with all elements being in centered position. Since we are under the linear critical velocity the equilibrium in the center of track is stable and thus the elements remain in centered position. By increasing the velocity slowly we moved from 15 m/s up to 23 m/s, and we observe that the stable equilibrium in the center of the track has turned into an unstable equilibrium, which indicates that we have passed the linear critical velocity. This happens around 20 m/s, and from our knowledge from railway dynamics this bifurcation is expected to be a subcritical Hopf bifurcation, at what is known as the linear critical velocity. That it is truly a Hopf bifurcation is seen in the eigenvalue analysis shown in figure 10.2. This figure shows how the eigenvalues migrate for velocities around $v = 18.4$ m/s. One interesting thing about this migration is that there exists two eigenvalues, which are complex conjugates of each other, that cross the imaginary axis (see figure 10.2(c)), and thus we can be certain that a Hopf bifurcation takes place. Another interesting aspect to comment is that the bifurcation trace analysis hinted at us that the Hopf bifurcation is about 20 m/s, but this is in contrast to the correct eigenvalue analysis that clearly shows that the Hopf bifurcation is at $v = 18.4$ m/s.

The problem is our criteria for judging a solution to have reached its asymptotic behaviour. In principle one should simulate infinitely long, but in practice this is not possible, so we have to stop the simulation at a certain point. The consequence of doing this is that we might not have reached the asymptotic solution, which is the situation in the bifurcation trace at 18.5 m/s, for example. This is also illustrated in figure 10.2(d). We see that the equilibrium in the center of the track has a repelling tendency after the Hopf bifurcation.

To determine the type of the Hopf bifurcation we investigated what happens right after the Hopf bifurcation. In contrast to our expectations we found that the Hopf bifurcation actually is supercritical. This is based in that there exists a stable growing limit cycle after the bifurcation. The limit cycle is found by doing simulations at velocities just above $v = 18.4$ m/s with initial conditions at the center of the track. The result is that the solution after a while is repelled to the limit cycle (see figure 10.3(a) and 10.3(b)).

However, by increasing the velocity further, this limit cycle is destroyed in a saddle node bifurcation at around $v = 18.6$ m/s. Simulating at $v = 18.7$ m/s we found the result in figure 10.3(c) and 10.3(d). This figure convinced us that the limit cycle is destroyed in a saddle node bifurcation, because what the figures show is a bottleneck effect typical from the *ghost* right after a saddle node bifurcation. The solution trajectory finally escapes the bottleneck and ends up on the hunting attractor found in the bifurcation

diagram in figure 10.1(a). After this analysis we were convinced that the true bifurcation diagram must exhibit a double saddle node bifurcation something like the diagram shown in figure 10.1(b), where the ghost we encountered is the one on the right.

One could argue that we have to increase our simulation time in the bifurcation trace simulation. However, the amount of simulation time needed in order to get repelled from the centered position of the track is surprisingly large (see for example figure 10.3(a)). Thus, in order to be able to make the bifurcation diagrams at all (due to its extremely time consuming process) we have used simulation times between 5 and 10 seconds, but we have to be aware that it introduces at certain amount of delay.

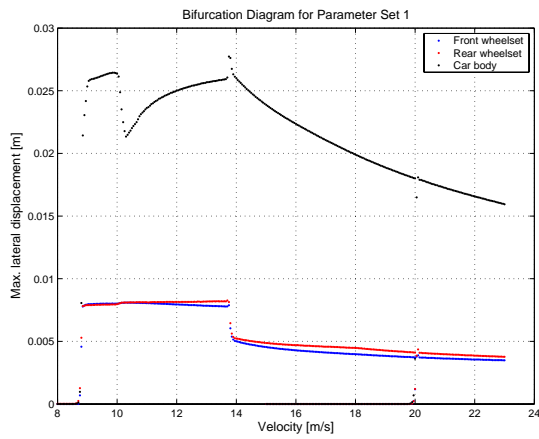
From 23 m/s, we then slowly decelerated to 8 m/s and observed that the hunting motion exists even for velocities under the critical value at $v = 18.4$ m/s. Thus the system exhibits hysteresis. The hunting motion eventually disappears when the velocity becomes less than another critical velocity known as the nonlinear critical velocity. This happens in a saddle node bifurcation about 9 m/s. The delay problem also occurs in the determination of the nonlinear critical velocity, but only in the sense of the ghost attractor as previously discussed.

This same method was applied to the water loaded and packed freight wagon, and we achieved the bifurcation traces in figures 10.1(c) and 10.1(d). Regarding the water loaded wagon we estimated the linear critical velocity to be under 23 m/s, and the nonlinear critical velocity was found to be just over 9 m/s. For the packed freight wagon we see a qualitatively changed bifurcation diagram in that the hunting attractor simply disappears at about $v = 17$ m/s (at least we were not able to follow any attractor different from zero for velocities lower than $v = 17$ m/s). The linear critical velocity in this case were about $v = 25$ m/s.

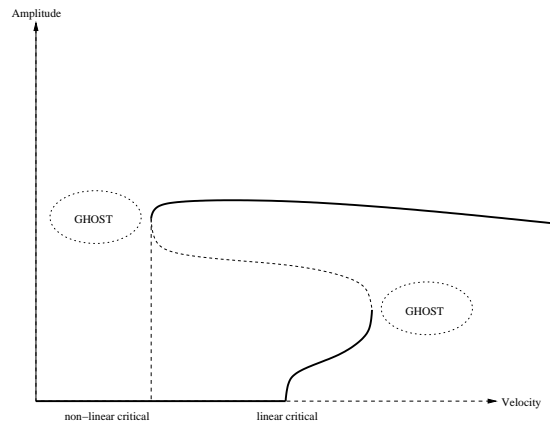
An immediate effect we can see in adding freight to the wagon is a stabilizing one. The Hopf bifurcation defining the linear critical velocity is raised by approximately 3 m/s and 5 m/s, however, the nonlinear critical velocity is about the same in the water loaded wagon case as for an empty wagon.

The bifurcation diagrams reveal an interesting conclusion on the dynamics of the freight wagon, namely, that the worst dynamic behaviour is actually present at medium velocities, since the hunting attractor has a tendency to increase in amplitude towards the nonlinear critical velocity. Furthermore, we see a sharp discontinuity in the bifurcation trace for the empty wagon at about 14 m/s, and for the water loaded wagon at 19 m/s. In these transition windows the motion did not reach any fixed amplitude oscillation and thus many different amplitudes are present in the bifurcation diagram. This is illustrated in figure 10.4(a) and 10.4(b). These figures show a simulation with the water loaded wagon running at $v = 18.85$ m/s. The conclusion from the figures is that the chaotic looking discontinuities in the bifurcation diagrams actually is *periodic* with the period of approximately 25 seconds.

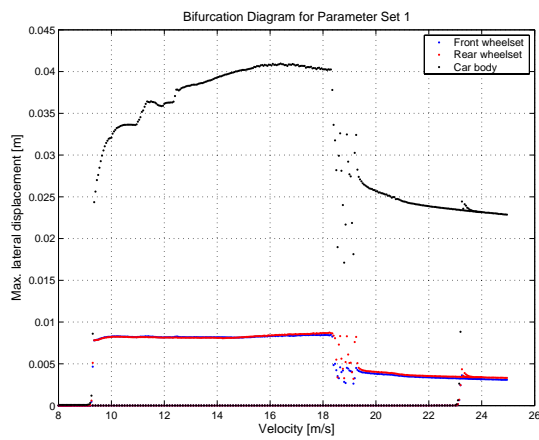
The origin of these discontinuities is investigated in the subsection to come.



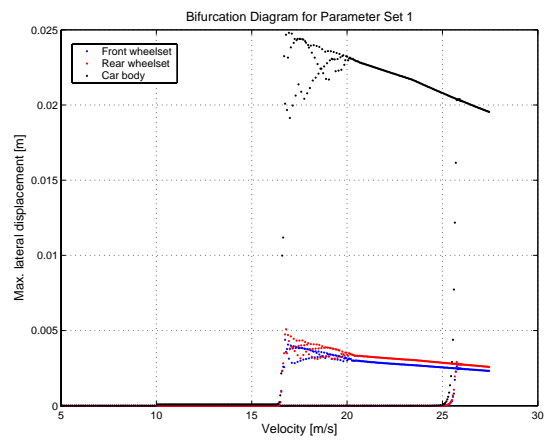
(a)



(b)

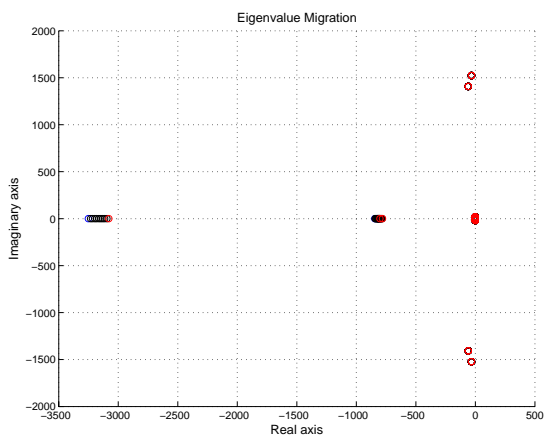


(c)

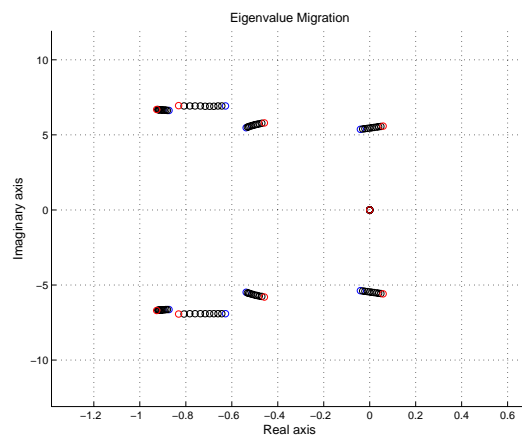


(d)

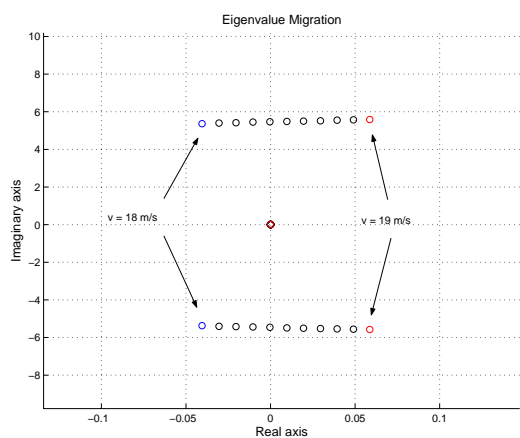
Figure 10.1: (a) Bifurcation diagram for the empty freight wagon. (b) Schematic of how two saddle node bifurcations for one of the elements may lie in our system. (c) Bifurcation diagram for the water loaded freight wagon. (d) Bifurcation diagram for the packed freight wagon.



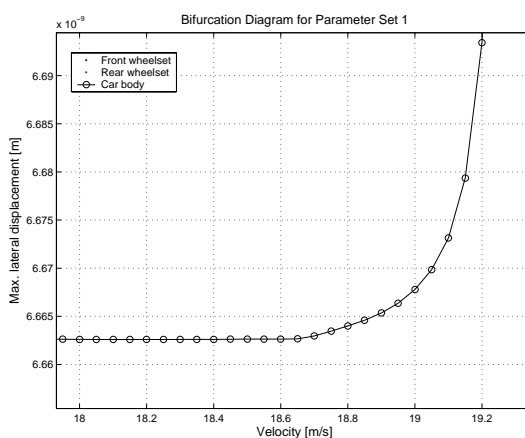
(a)



(b)



(c)



(d)

Figure 10.2: (a) All eigenvalues. (b) Zoomed view. The eigenvalue migration is clearly visible. (c) Zoomed view illustrating the Hopf bifurcation at $v = 18.4$ m/s. (d) delay effect.

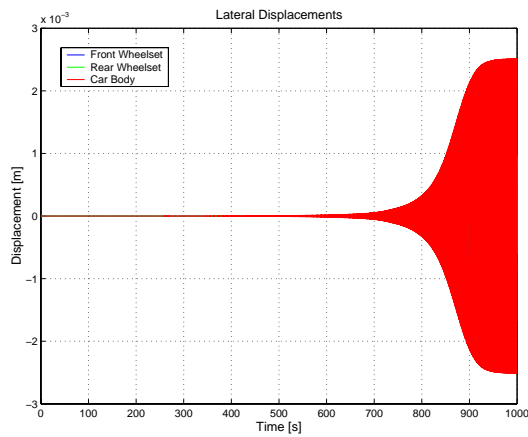
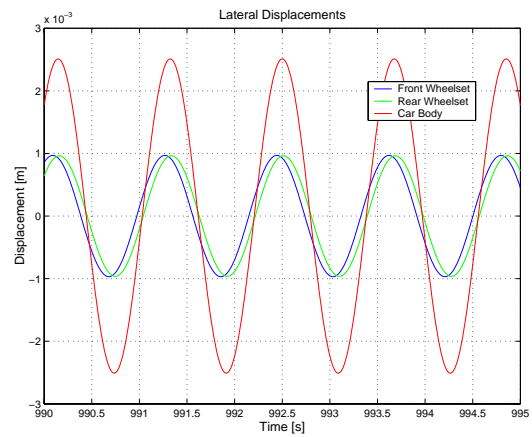
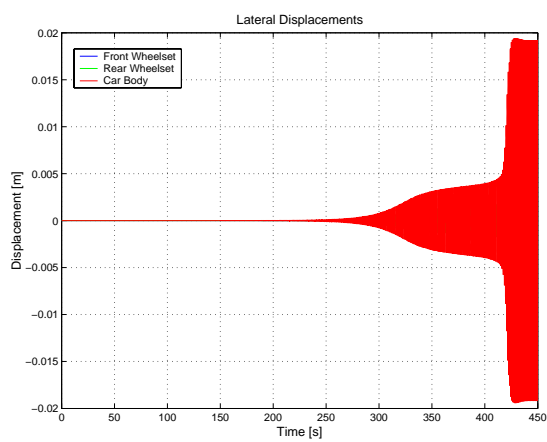
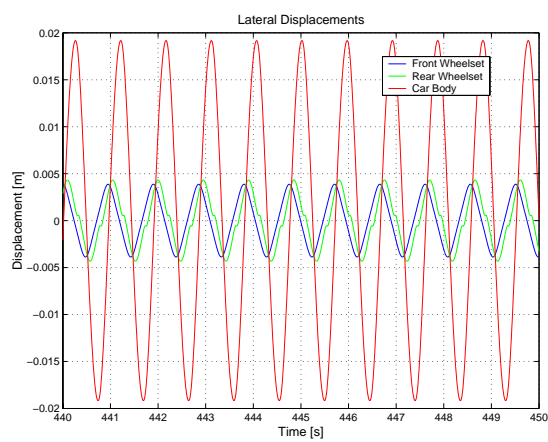
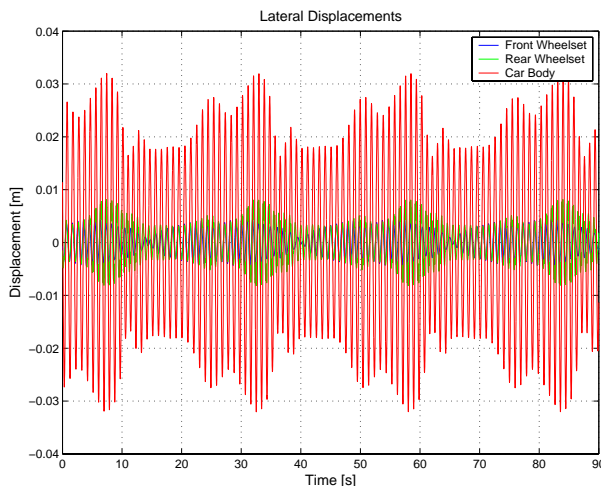
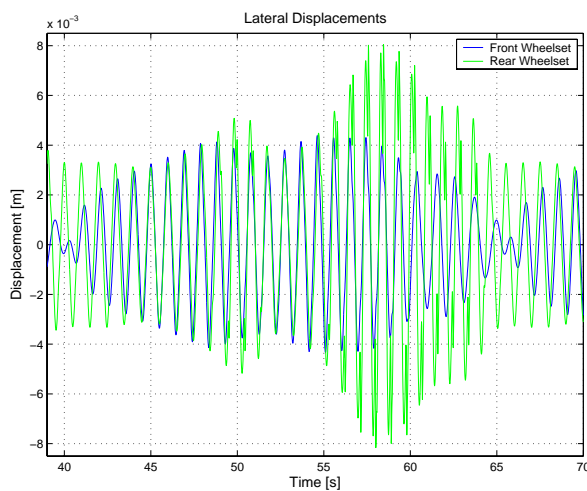
(a) $v = 18.5$ m/s.(b) $v = 18.5$ m/s zoomed.(c) $v = 18.7$ m/s.(d) $v = 18.7$ m/s zoomed.

Figure 10.3: Simulation of the empty wagon with the initial condition in the center of the track. The analysis shows that the Hopf-bifurcation is supercritical followed by a saddle node bifurcation. The ghost from the saddle node bifurcation causes the bottleneck effect seen in figure (c).



(a) Lateral motion in the ‘strange’ region of the water loaded bifurcation diagram. $v = 18.85$ m/s.



(b) A zoomed view, illustrating lateral motion of the wheelsets showing a period of about 25 seconds. $v = 18.85$ m/s.

Figure 10.4: These figures illustrate the periodic nature of the solutions in the ‘strange’ region ($v = 18.85$ m/s) of the water loaded bifurcation diagram. The bifurcation diagram has a strange region as a consequence of the 3 second sampling time, and in this region, solutions oscillate with longer periods.

10.2.2 Guidance Impact Behaviour

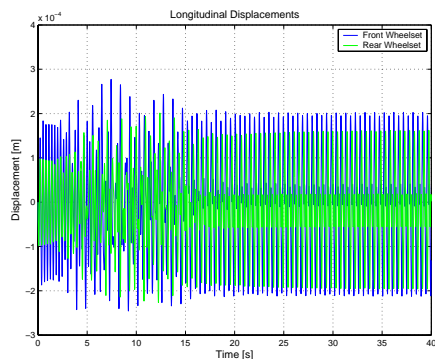
We here present a series of figures which will serve to illustrate the effect of the wheelset guidance structures. At first, we disable the guidance structures, and simulate the freight wagon, pretending that no wheelset guidance exists. Figures 10.5(a) and 10.5(b) show the stable hunting behaviour that the freight wagon experiences at 25 m/s. However, as we lower the velocity, the periodic lateral hunting motion increases in amplitude, as discussed previously, and this is evident in figure 10.5(c) and 10.5(d) where we see the hunting motion grow at 20 m/s. Furthermore, at this speed, the wheelsets will actually begin to lose contact with the rails! This is why the simulation goes no further than it does.

When we enable the wheelset guidances, at 20 m/s, we see that the hunting amplitude no longer seems to grow unbounded, but actually achieves a stable amplitude of about 4 mm lateral movement for both wheelsets. This is illustrated in figures 10.5(e) and 10.5(e). This simulation is also supported by figure 10.6 in which we show an impact analysis. The top four figures show time histories of the impact forces in longitudinal and lateral direction on both wheelsets. The bottom two figures show the relative distances to the guidances. It is seen that only the rear wheelset impacts laterally.

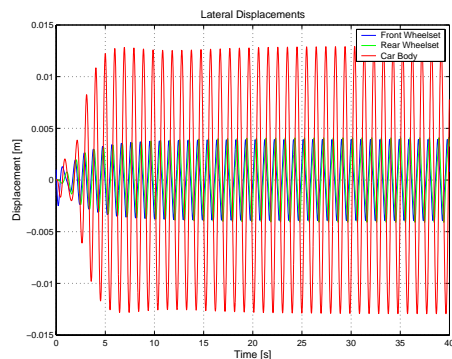
By simulating the empty wagon at $v = 40$ m/s with guidances we achieved the results in figure 10.7. Due to the contraction of the hunting attractor we do not see any impact in this case.

We now examine more closely some strange looking phenomena, observed in the bifurcation diagrams generated earlier. The bifurcation diagram for the empty wagon has what seems to be two interesting discontinuities. The first interesting transition point occurs at around 10 m/s, and the second one at just under 14 m/s. Regarding the bifurcation diagram for the water loaded wagon we saw a discontinuity at about $v = 19$ m/s, and finally for the packed wagon we saw some strange behaviour at about $v = 17$ m/s.

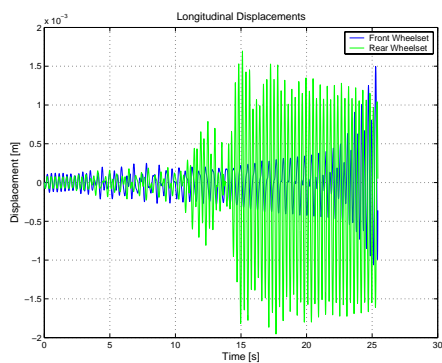
A series of results is presented for this investigation, and which are laid out in in the rest of this section. These results illustrate time series for the motion of the wheelsets and car body, as well as the impact characteristics of the wheelsets. For the empty wagon we show simulations at $v = 15$ m/s, $v = 13$ m/s, $v = 11$ m/s and $v = 9.5$ m/s, in that order. This is followed by simulating the water loaded wagon at $v = 20$ m/s and $v = 18$ m/s. Finally, we have the packed wagon running at $v = 17$ m/s.



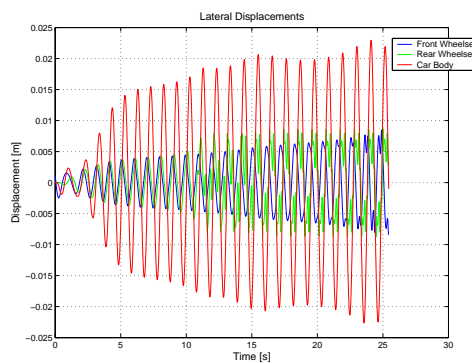
(a) Longitudinal, $v = 25$ m/s.



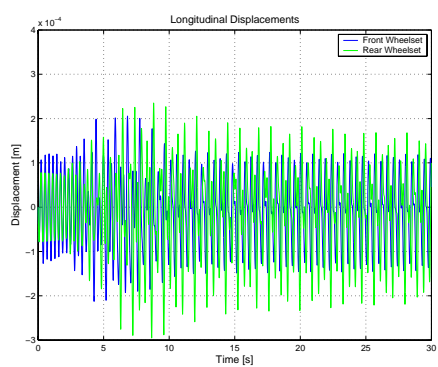
(b) Lateral, $v = 25$ m/s.



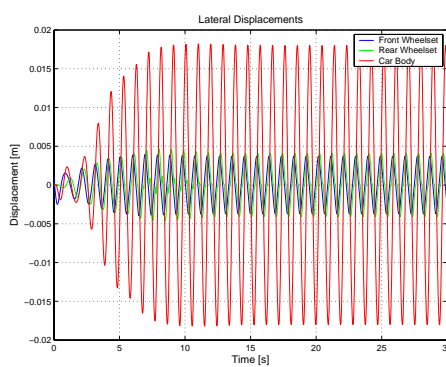
(c) Longitudinal, $v = 20$ m/s.



(d) Lateral, $v = 20$ m/s.



(e) Longitudinal, $v = 20$ m/s.



(f) Lateral, $v = 20$ m/s.

Figure 10.5: (a),(b),(c) and (d) are simulations without guidances. (e) and (f) are simulations with guidances.

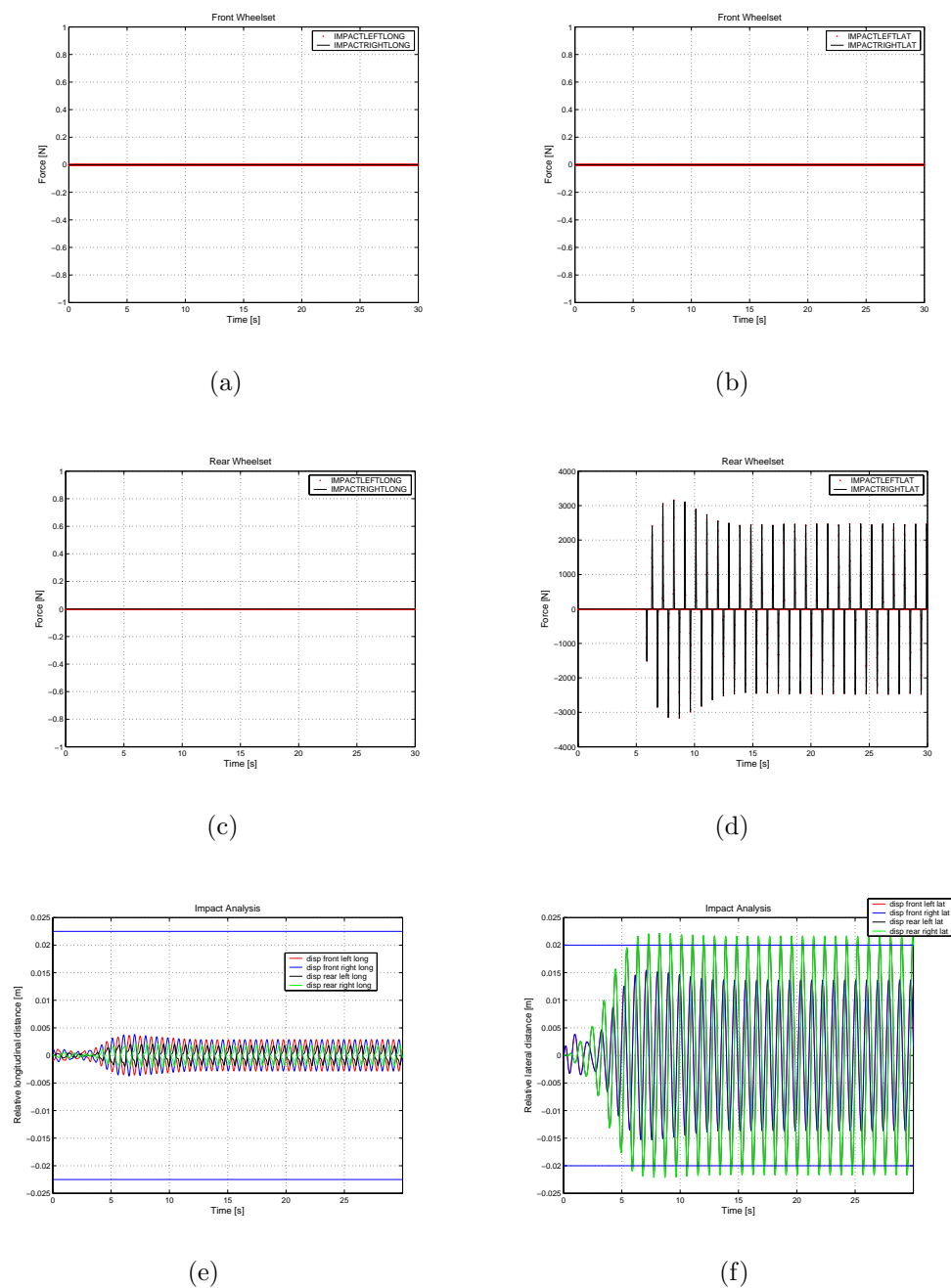
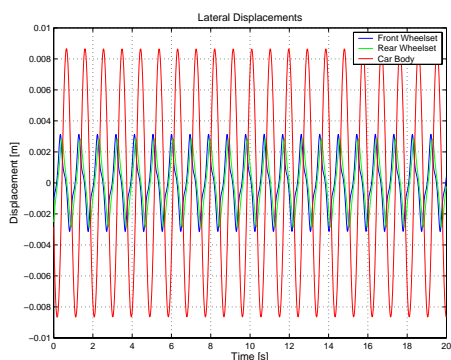
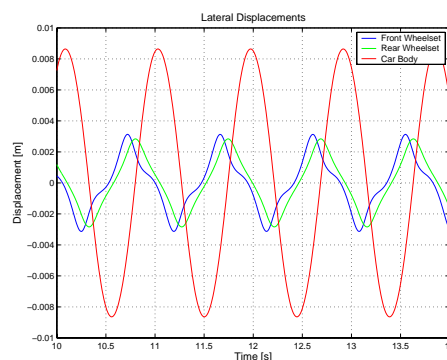


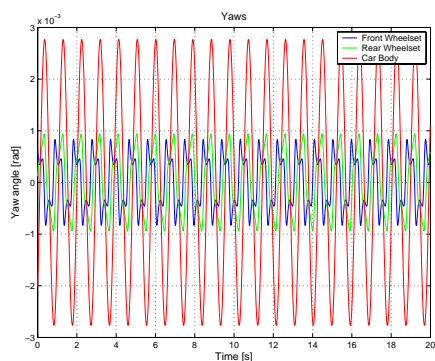
Figure 10.6: Simulation of the empty wagon with guidances. The velocity is $v = 20$ m/s. Regarding the clearance figures, we have illustrated the guidances by horizontal lines. (a) Front wheelset longitudinal impact forces. (b) Front wheelset lateral impact forces. (c) Rear wheelset longitudinal impact forces. (d) Rear wheelset lateral impact forces. (e) Longitudinal clearance illustrating no impact. (f) Lateral clearance illustrating impact on the rear wheelset.



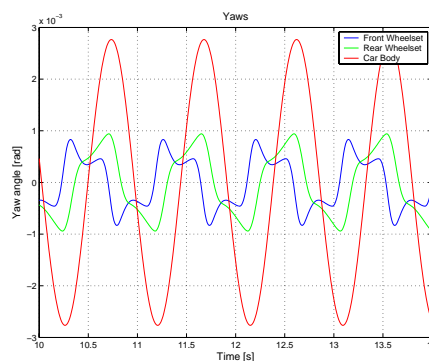
(a) Lateral.



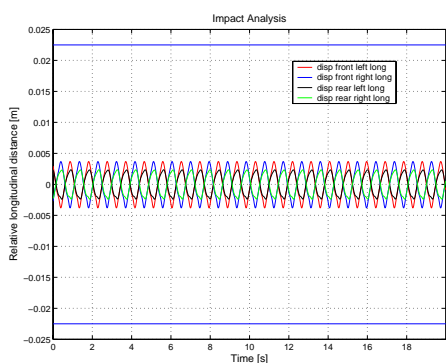
(b) Zoomed lateral.



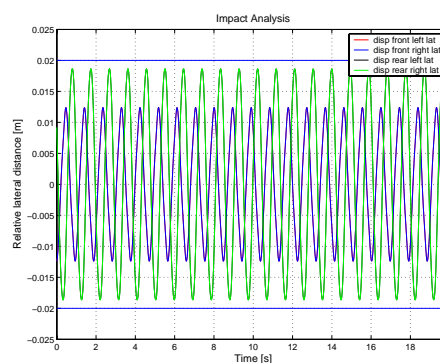
(c) Yaw.



(d) Zoomed yaw.



(e) Longitudinal clearance.



(f) Lateral clearance.

Figure 10.7: Simulation of the empty wagon with guidances. The velocity is $v = 40$ m/s. We do not see any impact at this velocity, because the hunting attractor contracts for increasing velocity.

Empty wagon running at $v = 15$ m/s

We can observe in the following figures that lateral movement of the wheelsets is relatively smooth, and that only the rear wheelset experiences impact with the freight wagon.

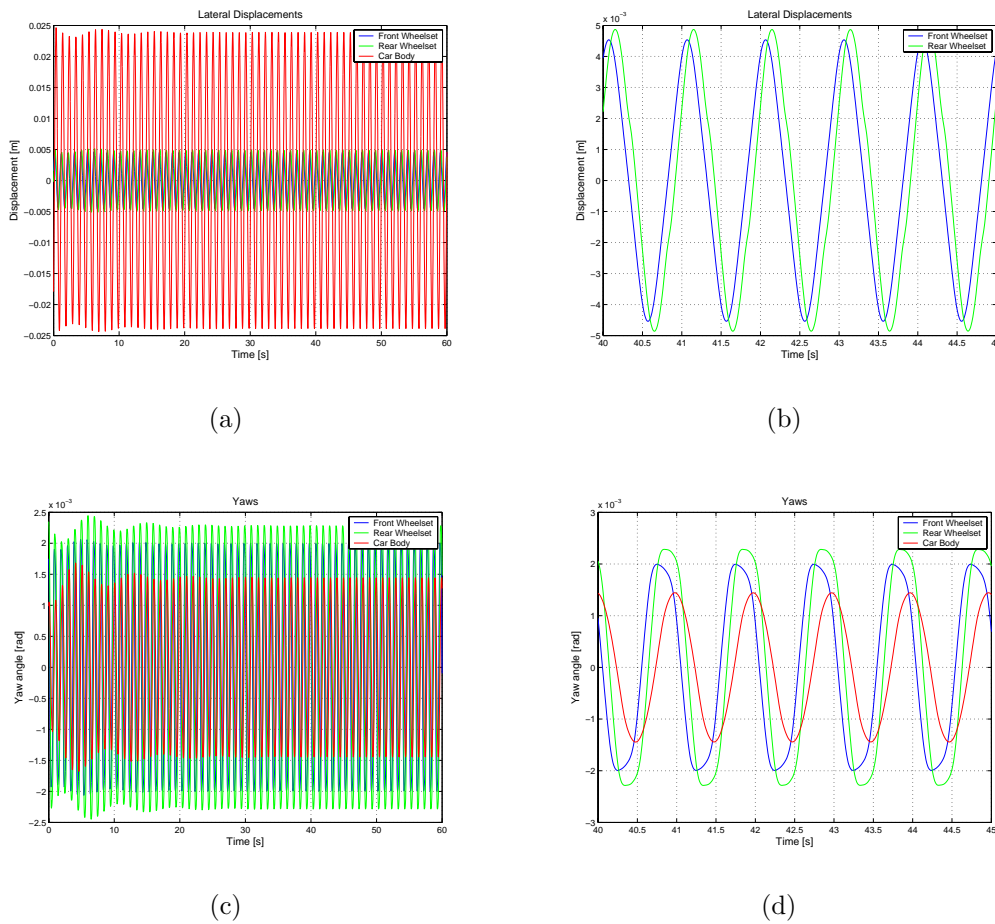
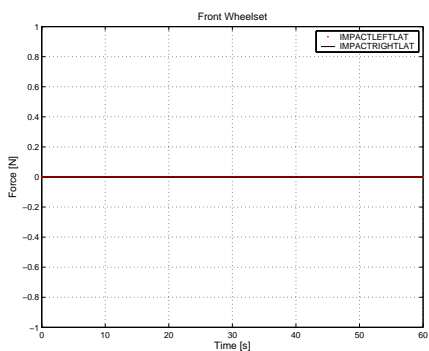
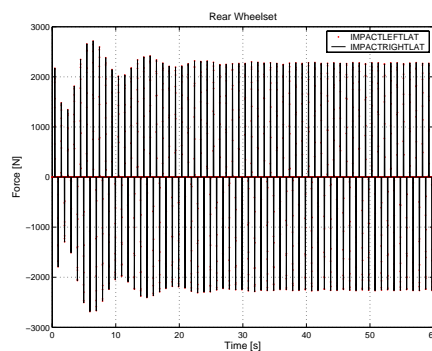


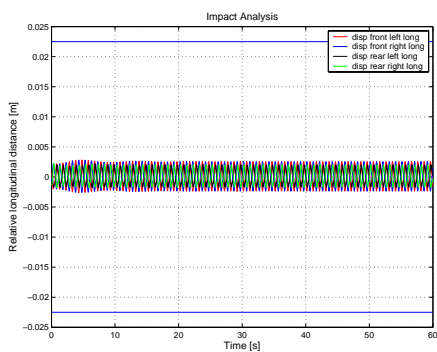
Figure 10.8: Simulation results of the empty wagon running at $v = 15$ m/s. (a) Lateral displacement. (b) Zoomed lateral displacement, excluding car body lateral displacement. (c) Yaw angle. (d) Zoomed yaw angle.



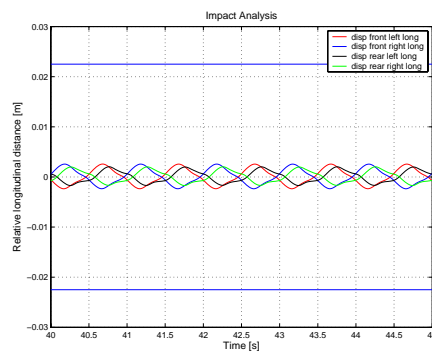
(a)



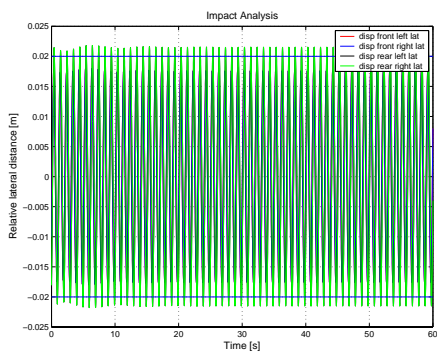
(b)



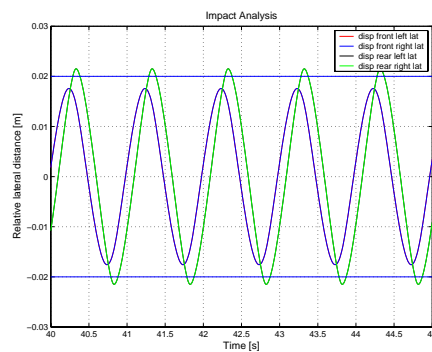
(c)



(d)



(e)



(f)

Figure 10.9: Impact analysis of the empty wagon running at $v = 15$ m/s. (a) Front wheelset lateral impact forces. (b) Rear wheelset lateral impact forces. (c) Longitudinal clearances. (d) Zoomed longitudinal clearance. (e) Lateral clearances. (f) Zoomed lateral clearances.

Empty wagon running at $v = 13$ m/s

We observe in the following figures that lateral movement of the front wheelsets is no longer smooth, especially the movement of the rear wheelset.

In observing the lateral clearances, we see that both wheelsets now impact, and the forces are comparable to each other, although the rear wheelset impacts with greater force. Thus the discontinuity at about 14 m/s is probably brought about a transition from only the rear wheelset impacting, to both wheelsets impacting.

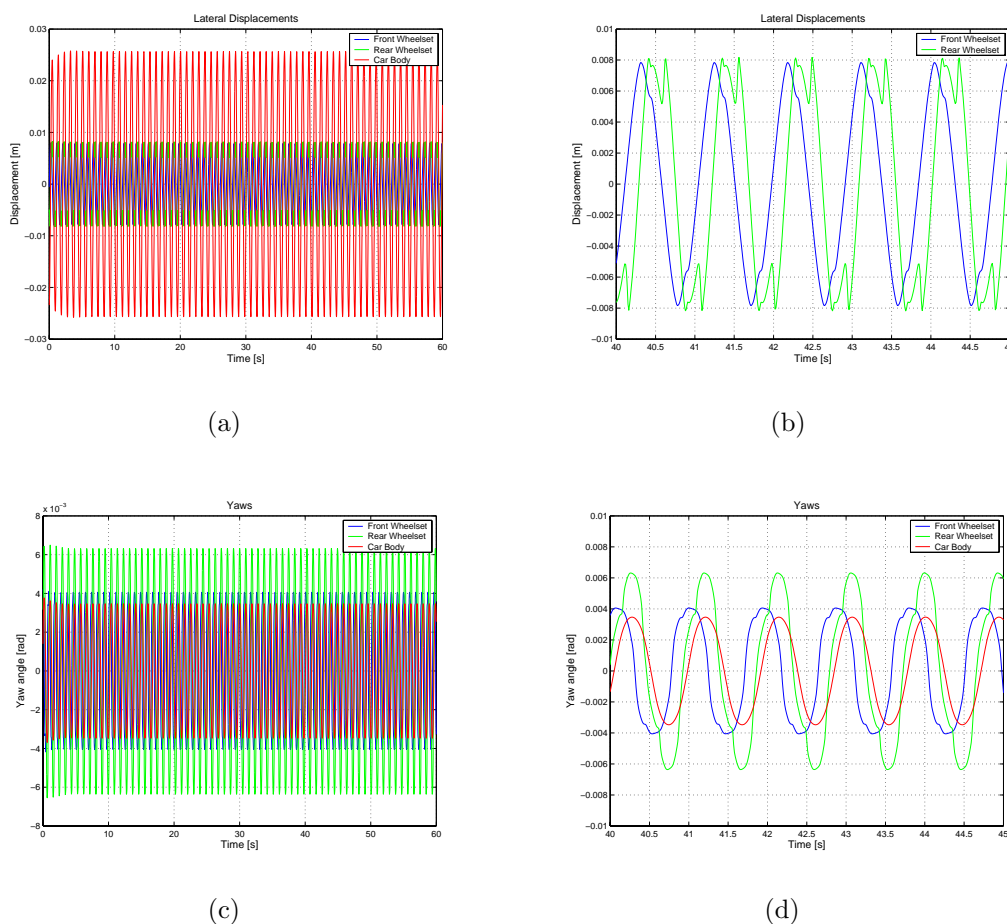
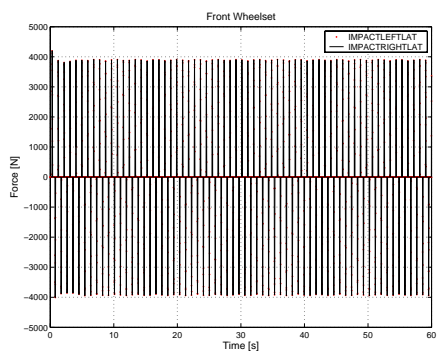
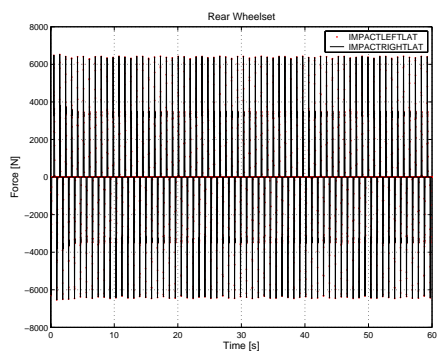


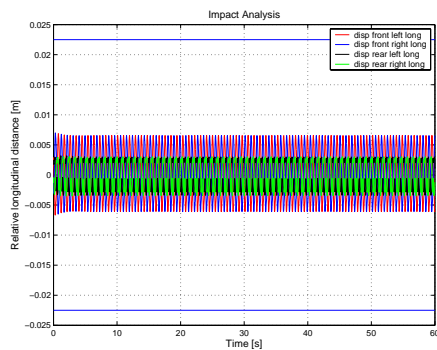
Figure 10.10: Simulation results of the empty wagon running at $v = 13$ m/s. (a) Lateral displacement. (b) Zoomed lateral displacement, excluding car body lateral displacement. (c) Yaw angle. (d) Zoomed yaw angle.



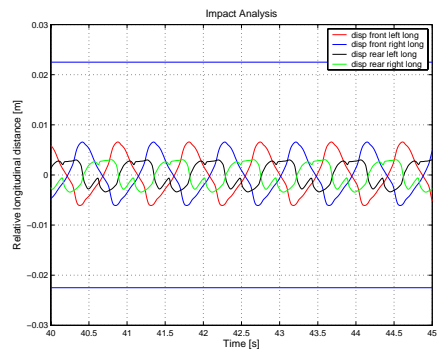
(a)



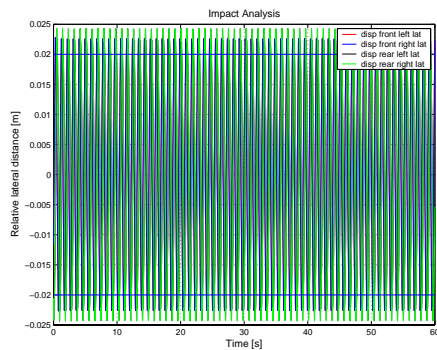
(b)



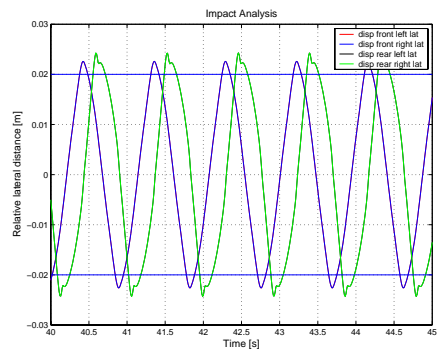
(c)



(d)



(e)



(f)

Figure 10.11: Impact analysis of the empty wagon running at $v = 13$ m/s. (a) Front wheelset lateral impact forces. (b) Rear wheelset lateral impact forces. (c) Longitudinal clearances. (d) Zoomed longitudinal clearance. (e) Lateral clearances. (f) Zoomed lateral clearances.

Empty wagon running at $v = 11$ m/s

In order to investigate the discontinuity at about 10 m/s in the lateral behaviour of the freight wagon body, we performed simulations for 11 m/s and 9.5 m/s. Here, at 11 m/s, we can ascertain that behaviour is relatively similar to that for 13 m/s. Chiefly, both wheelsets are impacting against the freight wagon body, and with more or less the same intensity. In particular, the movement of the rear wheelset laterally is still erratic at its extrema.

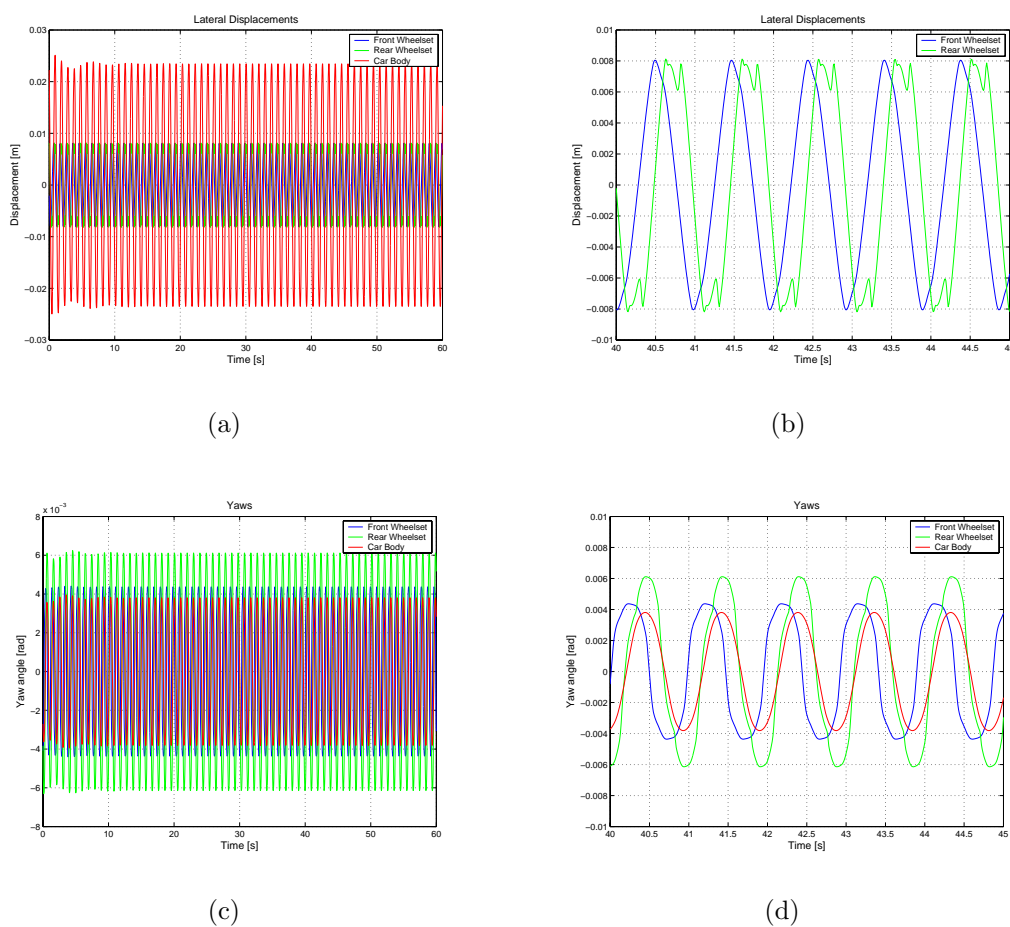


Figure 10.12: Simulation results of the empty wagon running at $v = 11$ m/s. (a) Lateral displacement. (b) Zoomed lateral displacement, excluding car body lateral displacement. (c) Yaw angle. (d) Zoomed yaw angle.

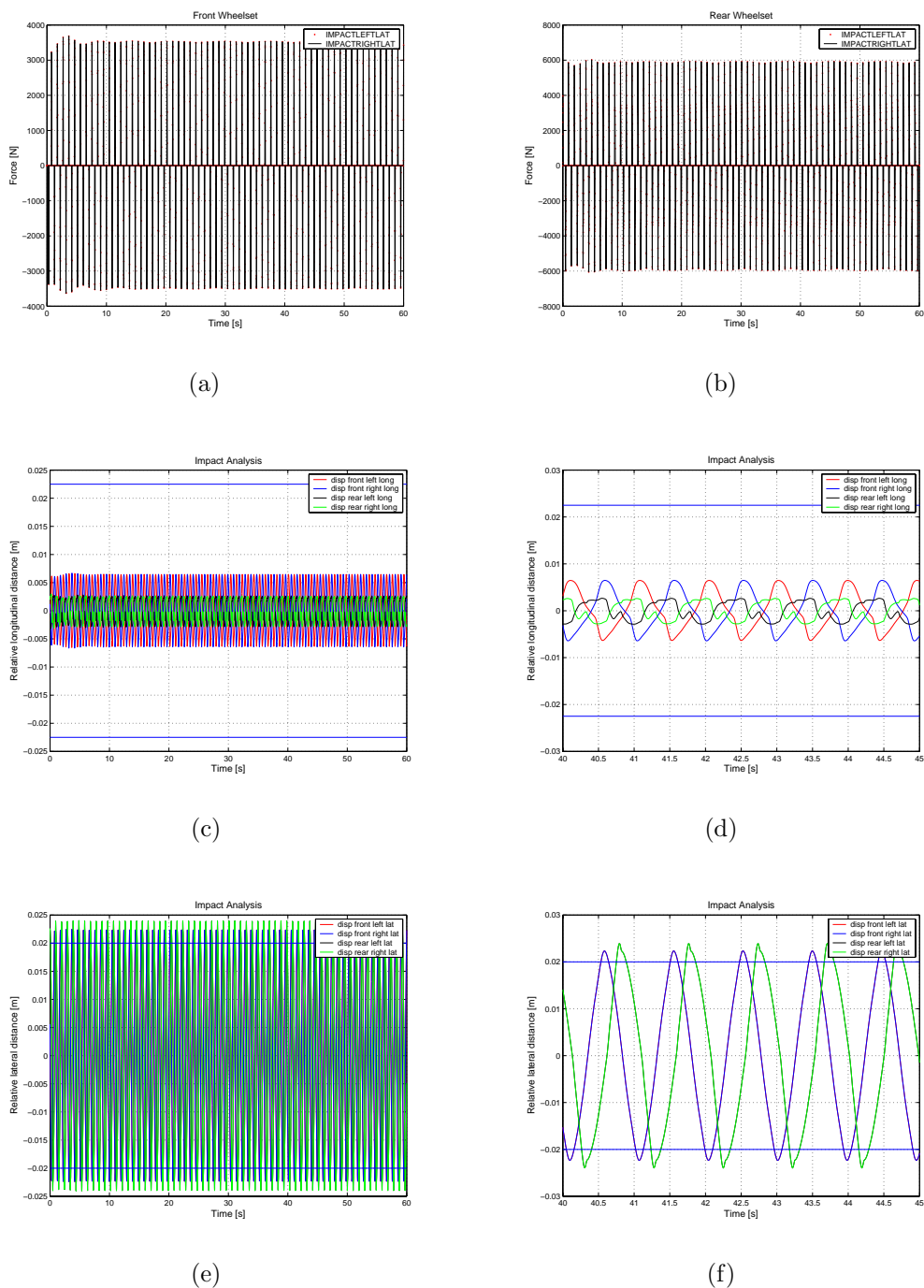


Figure 10.13: Impact analysis of the empty wagon running at $v = 11$ m/s. (a) Front wheelset lateral impact forces. (b) Rear wheelset lateral impact forces. (c) Longitudinal clearances. (d) Zoomed longitudinal clearance. (e) Lateral clearances. (f) Zoomed lateral clearances.

Empty wagon running at $v = 9.5$ m/s

At $v = 9.5$ m/s we can observe that behaviour is different that for $v = 11$ m/s. Of interest is the fact that although both wheelset still impact laterally against the freight wagon body, the rear wheelset no longer behaves erratically at its extrema.

In that both wheelsets still impact laterally, no significant effect is seen on the bifurcation trace of any discontinuity with respect to either wheelset hunting, but the discrepancy is located with the lateral hunting of the car body. This jump can come about due to a change in the way forces are imparted upon the car body from the wheelsets during impact, in that now they are smoother than the erratic rear wheelset impacts experienced at $v = 11$ m/s.

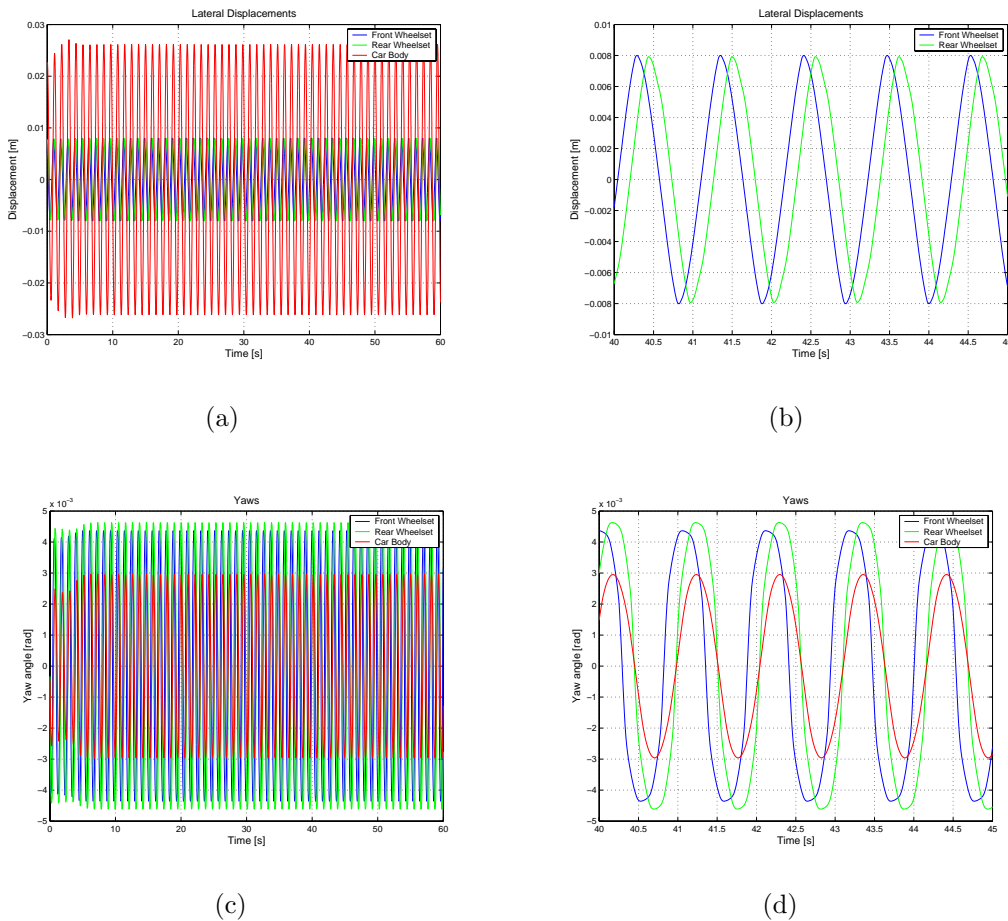


Figure 10.14: Simulation results of the empty wagon running at $v = 9.5$ m/s. (a) Lateral displacement. (b) Zoomed lateral displacement, excluding car body lateral displacement. (c) Yaw angle. (d) Zoomed yaw angle.

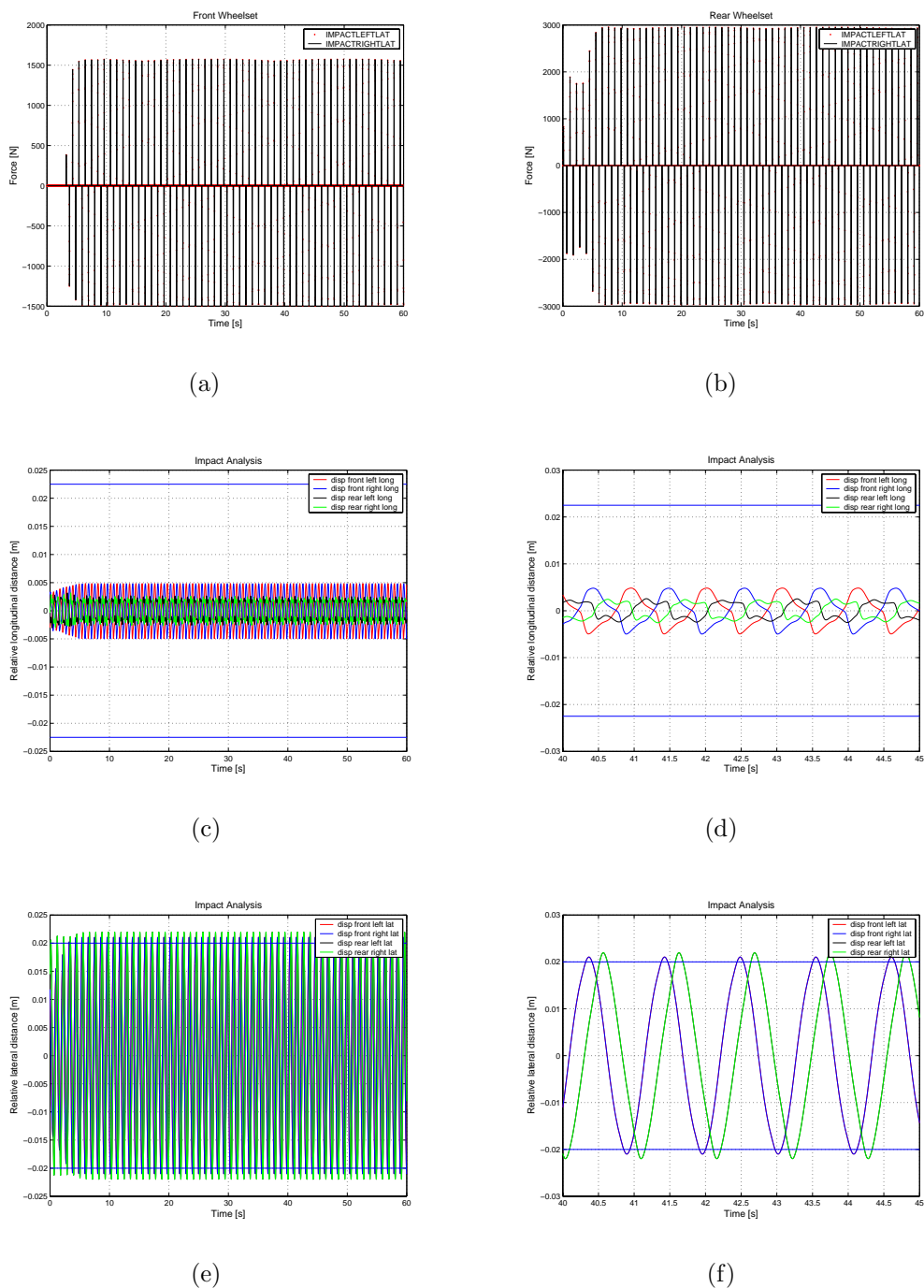


Figure 10.15: Impact analysis of the empty wagon running at $v = 9.5$ m/s. (a) Front wheelset lateral impact forces. (b) Rear wheelset lateral impact forces. (c) Longitudinal clearances. (d) Zoomed longitudinal clearance. (e) Lateral clearances. (f) Zoomed lateral clearances.

Water loaded wagon running at $v = 20$ m/s

We here present time series data for a water loaded freight wagon running at $v = 20$ m/s. After an initial transient, we see that the wagon settles into a low frequency hunting oscillation.

What merits special attention here is the impact behaviour of the wheelsets. The rear wheelset dominates in this role, since it is clearly the one impacting hardest. The front wheelset impacts, but not as hard as the rear wheelset. In fact, as velocity increases, the front wheelset will not impact at all with the freight wagon structure. Eventually, the rear wheelset won't either, given sufficient velocity.

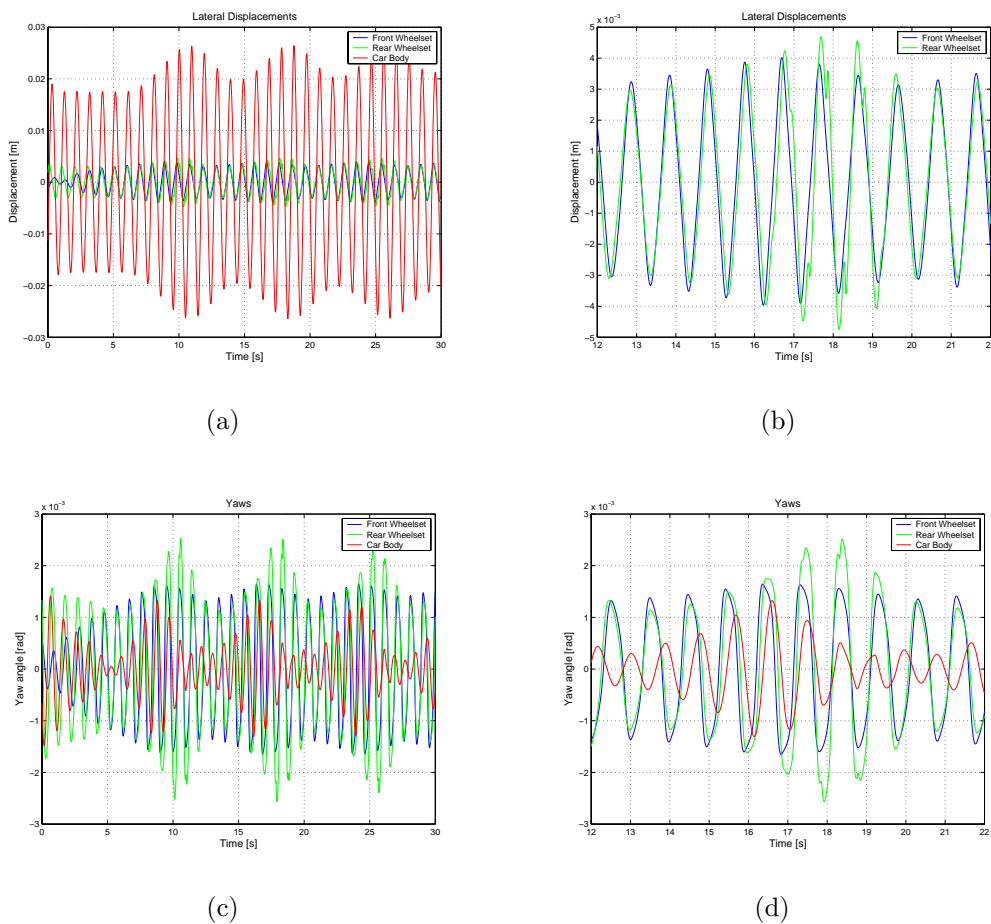
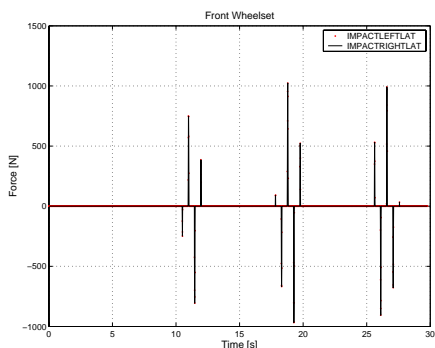
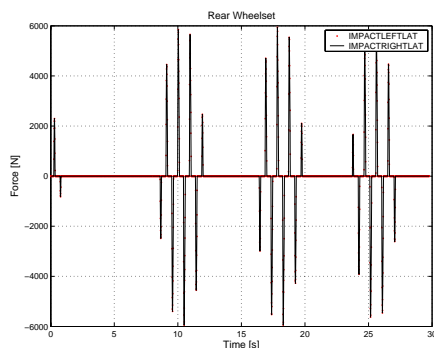


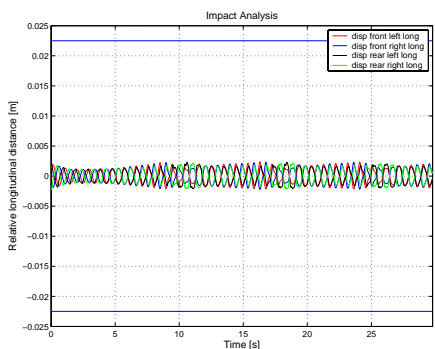
Figure 10.16: Simulation results of the water loaded wagon running at $v = 20$ m/s. (a) Lateral displacement. (b) Zoomed lateral displacement, excluding car body lateral displacement. (c) Yaw angle. (d) Zoomed yaw angle.



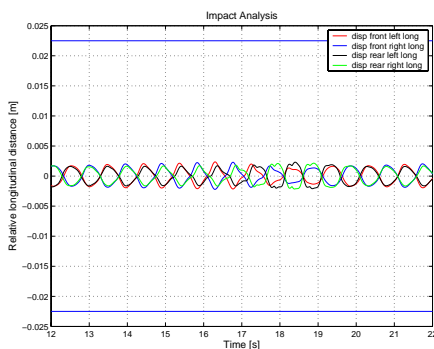
(a)



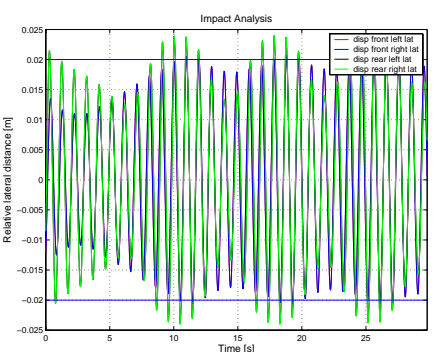
(b)



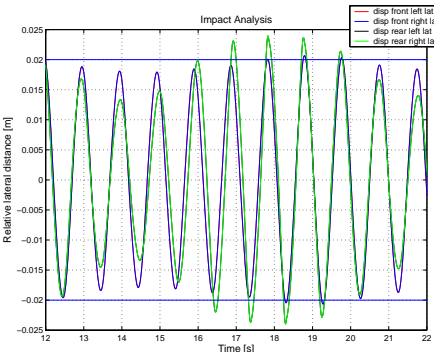
(c)



(d)



(e)

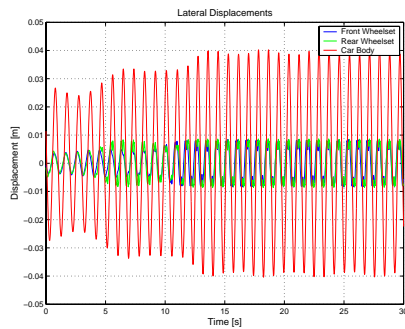


(f)

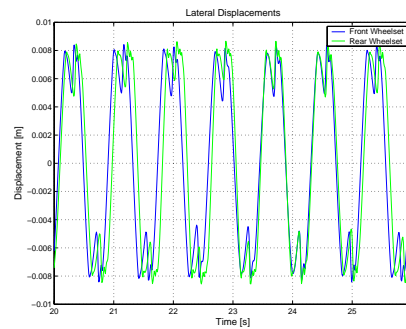
Figure 10.17: Impact analysis of the water loaded wagon running at $v = 20$ m/s. (a) Front wheelset lateral impact forces. (b) Rear wheelset lateral impact forces. (c) Longitudinal clearances. (d) Zoomed longitudinal clearance. (e) Lateral clearances. (f) Zoomed lateral clearances.

Water loaded wagon running at $v = 18$ m/s

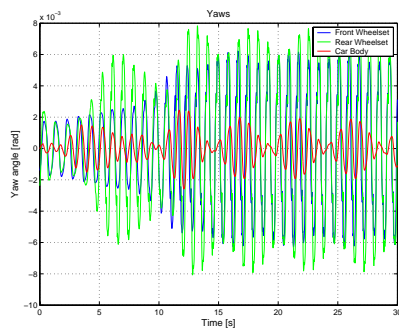
After an initial transient, we see that the wagon settles into a low frequency hunting oscillation. Here, we take special note of the impact behaviour of the wheelsets. Both wheelsets now impact forcefully with the freight wagon structure, with nearly equal vigour. This indicates to us that the transition that takes place near the $v = 19$ m/s mark on the bifurcation trace figure 10.1(c) is one where the front wheelset begins to irritate the dynamics of the freight wagon more and more as it begins to impact, and its impacts increase in strength. Furthermore, the long period behaviour is what seems to lend a chaotic pattern to the bifurcation trace figure 10.1(c), but since we only sample the values for the bifurcation traces over a 3 second interval, we evade considering an entire wavelength of data, and thus we produce what seems to be a chaotic transition in the bifurcation trace.



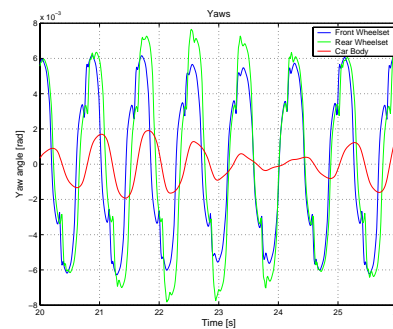
(a)



(b)



(c)



(d)

Figure 10.18: Simulation results of the water loaded wagon running at $v = 18$ m/s. (a) Lateral displacement. (b) Zoomed lateral displacement, excluding car body lateral displacement. (c) Yaw angle. (d) Zoomed yaw angle.

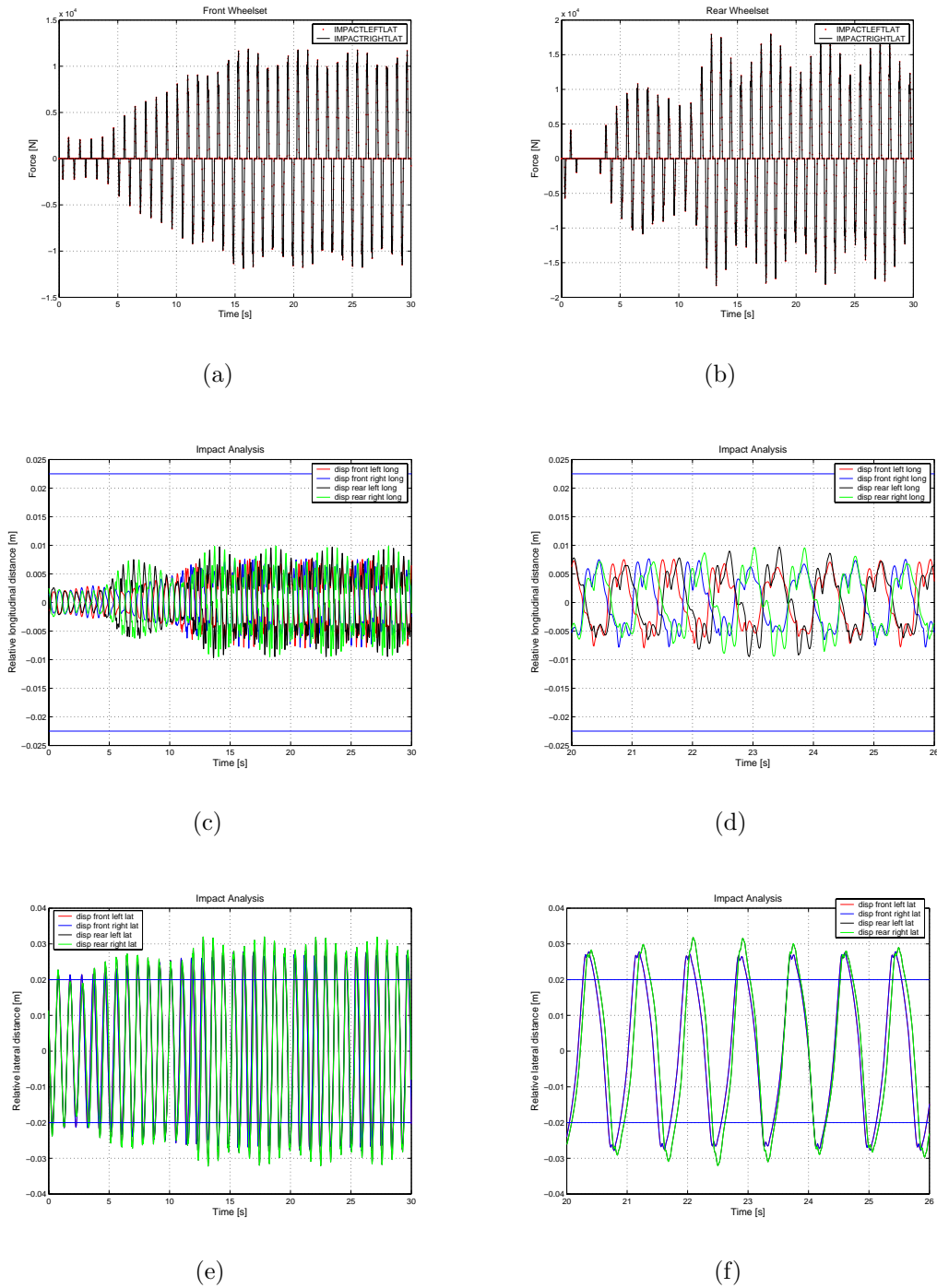


Figure 10.19: Impact analysis of the water loaded wagon running at $v = 18$ m/s. (a) Front wheelset lateral impact forces. (b) Rear wheelset lateral impact forces. (c) Longitudinal clearances. (d) Zoomed longitudinal clearance. (e) Lateral clearances. (f) Zoomed lateral clearances.

Packed wagon running at $v = 17$ m/s

The strange behaviour in the bifurcation trace in the case of the packed wagon occurs as we slow down towards the nonlinear critical velocity. What actually occurs is that a new frequency is introduced in the lateral hunting motion. The period of this is beyond the 3 second sampling time, and introduces this strange behaviour in the bifurcation diagram. Had the sampling time been longer, we could have avoided this behaviour, but may have missed the fact that the hunting period begins to change.

In this section, we present a series of figures which illustrate the behaviour of the packed freight wagon at $v = 17$ m/s, which resides in this ‘strange’ region on the bifurcation trace. We clearly see that the period is about 8 seconds, which is clearly larger than the 3 second sampling time we use.

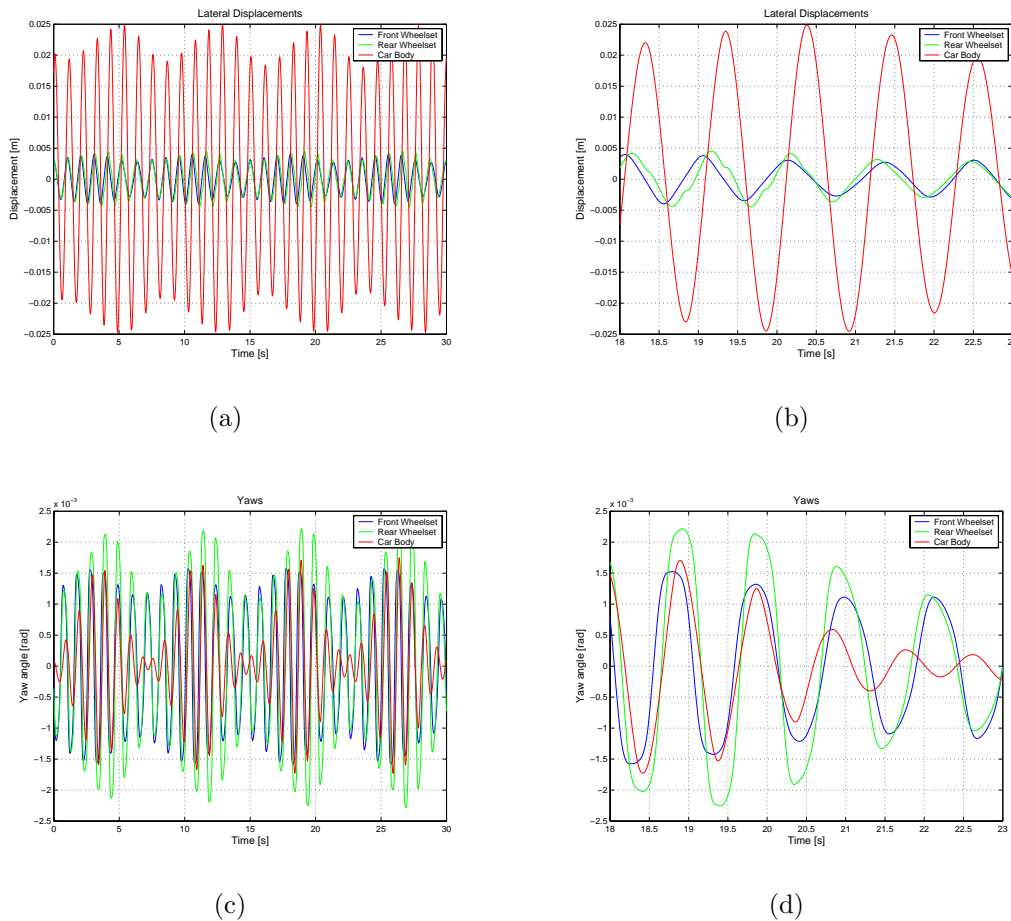
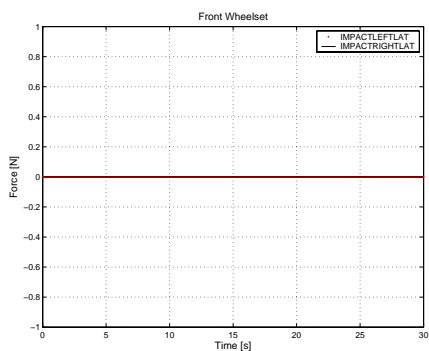
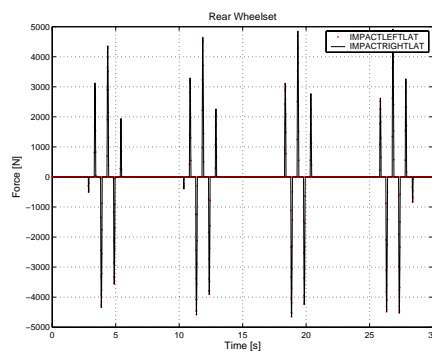


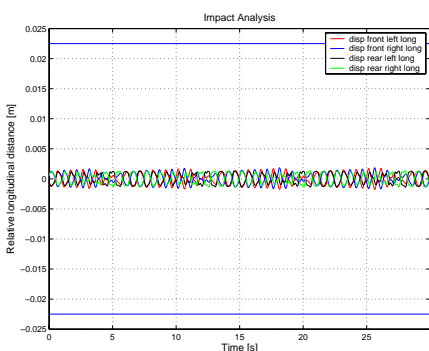
Figure 10.20: Simulation results of the packed wagon running at $v = 17$ m/s. (a) Lateral displacement. (b) Zoomed lateral displacement, excluding car body lateral displacement. (c) Yaw angle. (d) Zoomed yaw angle.



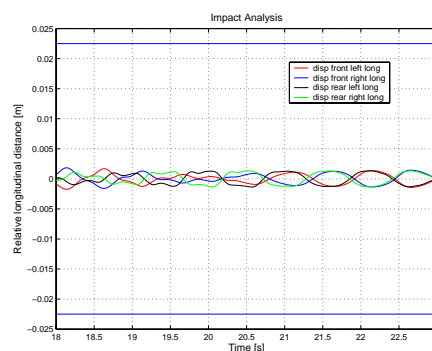
(a)



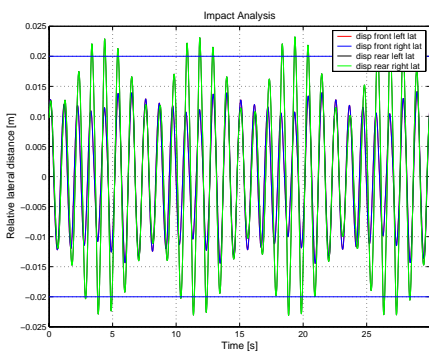
(b)



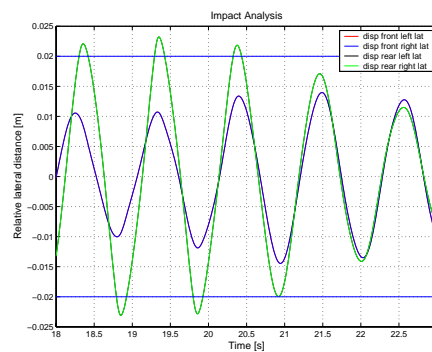
(c)



(d)



(e)



(f)

Figure 10.21: Impact analysis of the packed wagon running at $v = 17$ m/s. (a) Front wheelset lateral impact forces. (b) Rear wheelset lateral impact forces. (c) Longitudinal clearances. (d) Zoomed longitudinal clearance. (e) Lateral clearances. (f) Zoomed lateral clearances.

10.3 Suspension Parameter Set 2

10.3.1 Critical Velocities

We have here calculated bifurcation traces for a freight wagon using suspension parameter set 2. These are presented in figures 10.22 and 10.23. Similar to the bifurcation traces for suspension parameter set 1 we see that the amplitude of the hunting motion increases as the velocity is lowered towards the nonlinear critical velocity in the empty and water loaded case. For the packed wagon, the situation is quite different in that the large hysteresis loop seems to be gone.

In contrast to the bifurcation diagrams for the first suspension parameter set we do not see any discontinuities in the bifurcation diagram. The general picture now is a better dynamic behaviour for the freight wagon. Especially, the amplitude of the hunting motion for the car body is reduced.

This tendency is, however, not surprising. We described in the chapter 4 that the characteristic difference between the two suspension parameter sets is that suspension parameter set 2 dissipates more energy. Thus when comparing two freight wagons with different dissipation abilities in the suspension it might be reasonable to expect that the wagon with best dissipation capability has the best running properties.

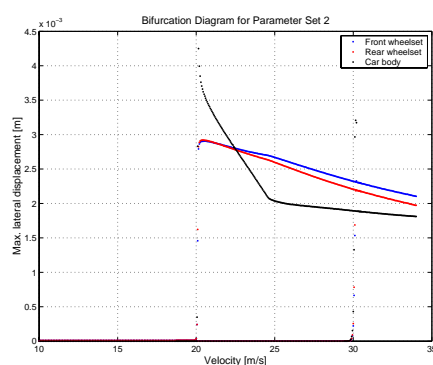
Furthermore, figure 10.22(b) details the bifurcation trace for the front wheelset in the empty freight wagon case. An interesting view is to zoom in on this figure (see 10.22(c)), because it illustrates the effect of dry friction present in the suspension. The effect is that the stable equilibrium in the center of the track is shifted slightly after one revolution in the hysteresis loop. This behaviour is similar to the one predicted by the simple dry friction system earlier investigated, and we see its effect here.

As we proceed to analyse the packed wagon, the qualitative behaviour changed completely as shown in the bifurcation trace in figure 10.23(b). The saddle node bifurcation that defines the nonlinear critical velocity seems to be gone, although it still looks like there is some hysteresis present. However, the prediction of the hysteresis loop is not correct, because it is created by the delay phenomenon in our bifurcation trace method. This conclusion was revealed in the following manner.

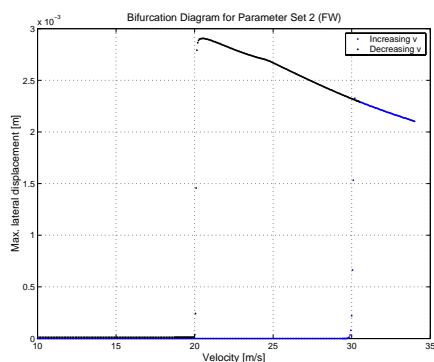
By making an eigenvalue analysis of the centered position we found that there is a Hopf bifurcation taking place at $v = 33.7$ m/s. Figure 10.24 shows how the eigenvalues cross the imaginary axis just around the critical velocity. At this point we do not know whether the Hopf bifurcation is supercritical or subcritical. By examining the asymptotic solution for velocities slightly greater than the critical velocity we found an increasing limit cycle corresponding to the one shown in the bifurcation diagram. An example of this is shown in figure 10.25. This figure illustrates two important properties of the system. First, it is shown how long time it takes to reach the asymptotic solution (which in fact is the origin of the delay problem in the bifurcation trace method). Secondly, by comparing amplitudes (see zoomed view in figure 10.25(b)) we see that the asymptotic

solution is the one predicted in the bifurcation diagram in figure 10.23(b). The conclusion from this is that the Hopf bifurcation is supercritical.

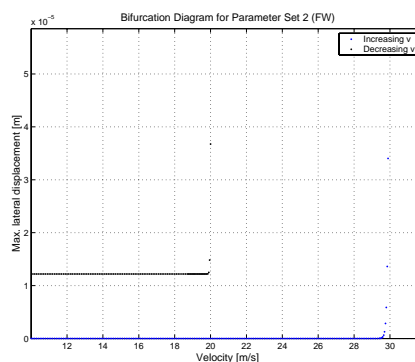
Although not found, we emphasize the existence of a distant, undiscovered hunting attractor is possible in the case of the packed wagon.



(a)

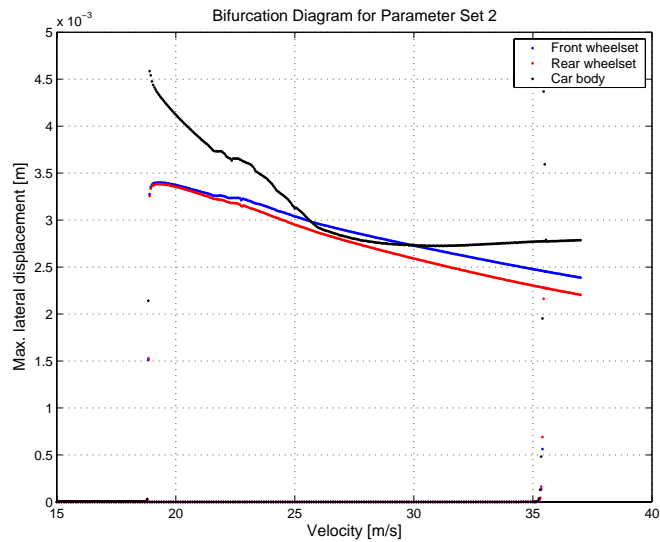


(b)

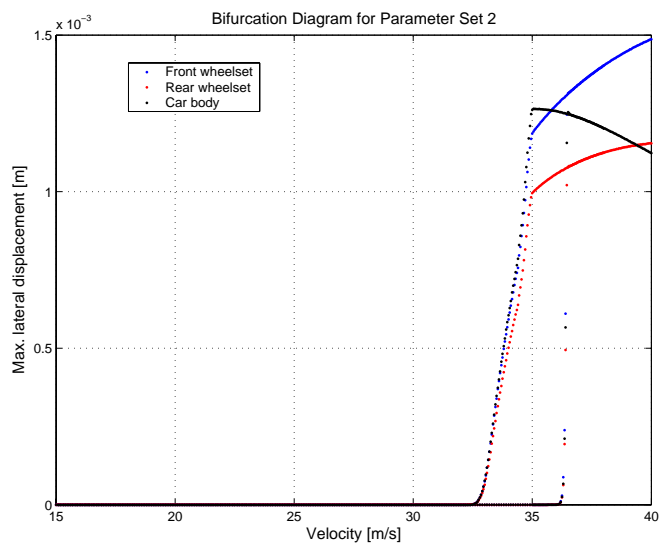


(c)

Figure 10.22: (a) Bifurcation diagram for the empty freight wagon. (b) Bifurcation diagram for the front wheelset emphasizing the different behaviour between increasing and decreasing the velocity. Especially, it is seen that the stable equilibrium in the center of track has changed after one lap in the hysteresis loop.

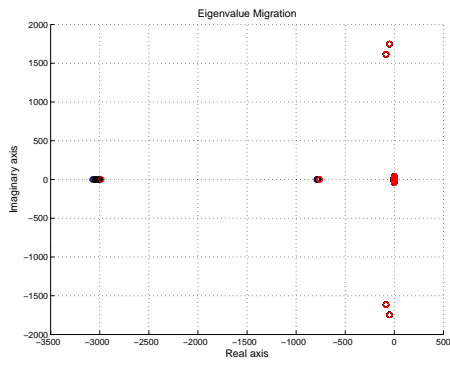


(a)

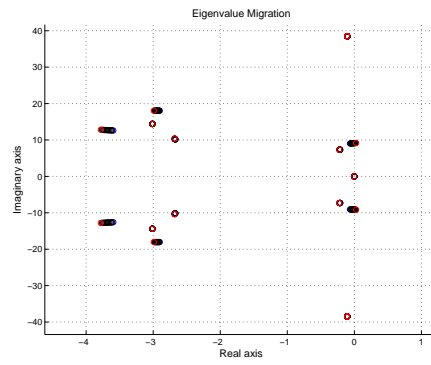


(b)

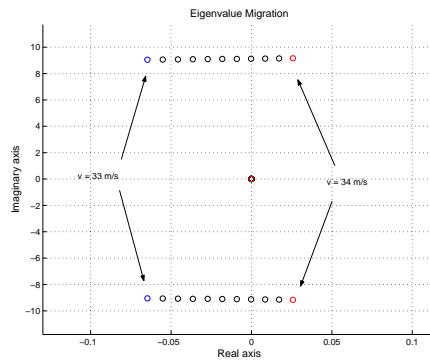
Figure 10.23: (a) Bifurcation diagram for the water loaded wagon. (b) Bifurcation diagram for the packed freight wagon. Regarding the packed freight wagon we observe a small hysteresis loop, however, further analysis revealed that we have a supercritical Hopf bifurcation exhibiting no hysteresis. The hysteresis loop observed is a consequence of the delay phenomenon present in our bifurcation trace method.



(a) All eigenvalues.

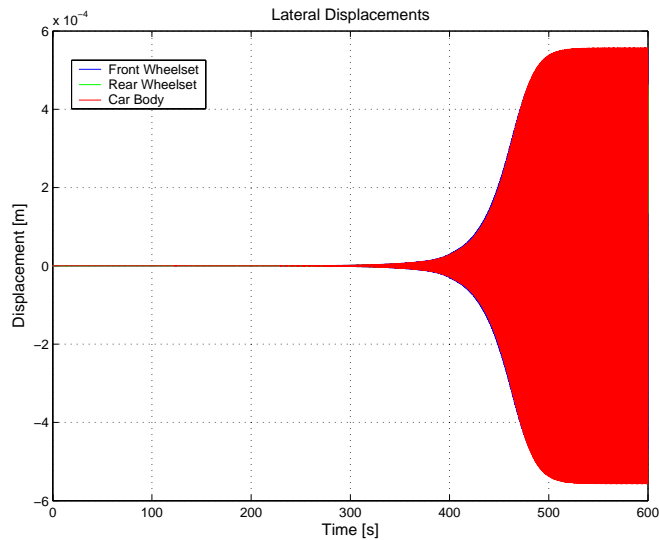


(b) Zoomed view. The eigenvalue migration is clearly visible.

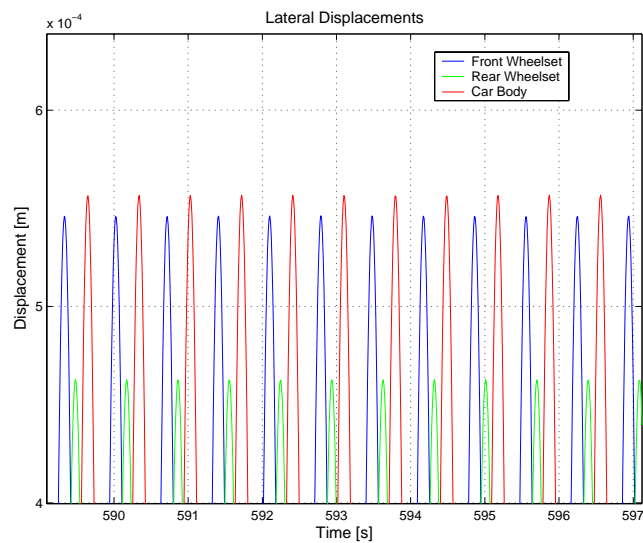


(c) Zoomed view illustrating the hopf bifurcation at $v = 33.7$ m/s.

Figure 10.24: Eigenvalue migration for the packed freight wagon using suspension parameter set 2.



(a)



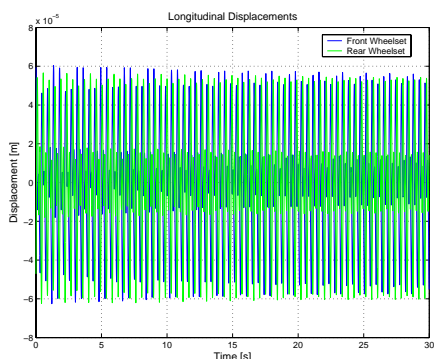
(b)

Figure 10.25: (a) Time history at $v = 34$ m/s which is just above the Hopf bifurcation. The center of the track is the initial condition and the figure illustrates how long time it takes to reach the hunting attractor. In this case it is approximately 530 s of simulation time. (b) Zoomed view of the time history. By comparing amplitudes it becomes evident that the attractor reached is the one shown in the bifurcation diagram in figure 10.23(b).

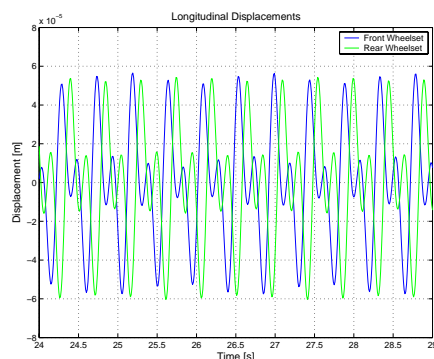
10.3.2 Guidance Impact Behaviour

Figure 10.26 illustrates the movement for the empty freight wagon at a velocity of 21 m/s, close to the maximum lateral amplitude hunting movement in this case. In this figure, we can observe that the wheelset keeps itself well within the clearances afforded to it, and no impact occurs. This was in fact the result for all simulations with suspension parameter set 2.

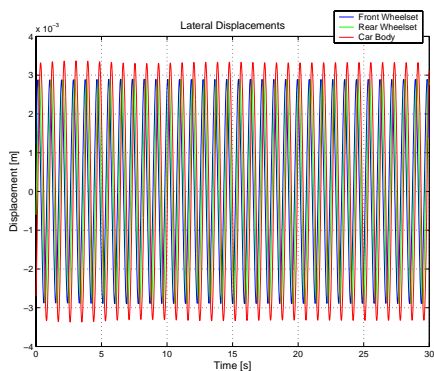
The fact that we did not observe any impact for suspension parameter set 2 divides the to suspension parameter set dramatically regarding the dynamic behaviour of the freight wagon. Our explanation for this difference, in modelling the suspension links with the two parameter sets, is the fundamental difference in the dry friction damping capability between the two parameter sets.



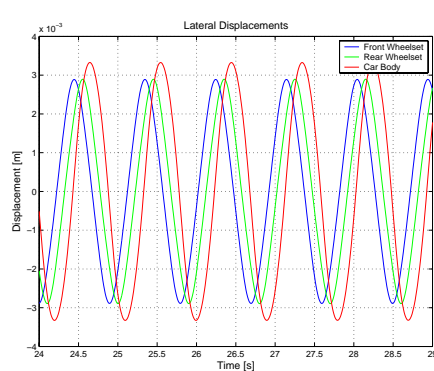
(a) Longitudinal.



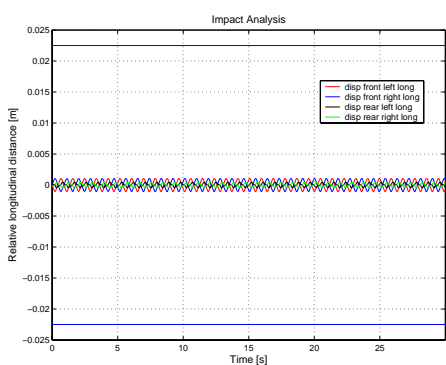
(b) Zoomed longitudinal.



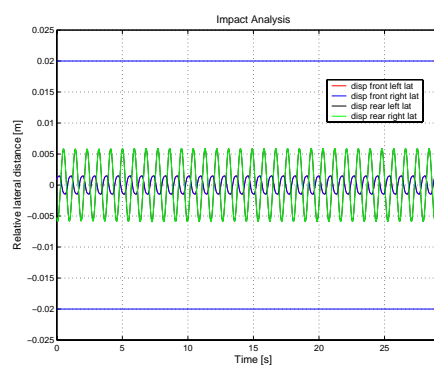
(c) Lateral.



(d) Zoomed lateral.



(e) Longitudinal clearance.



(f) Lateral clearance.

Figure 10.26: Impact investigation for the empty freight wagon using suspension parameter set 2. The velocity is $v = 21$ m/s.

10.4 Frequency Analysis

In this section we will investigate which frequencies that are characteristic in the hunting motion of our model. The result of the analysis is shown in table 10.1 and table 10.2. We have found the frequencies through a power spectrum analysis of each of the motion variables given in the tables. The tables are supported by figures 10.27 to 10.30 that illustrates this frequency analysis for some of the motion variables.

By looking at the results shown in the tables it becomes evident that given a certain configuration² of the model leads to phase locked oscillations in the lateral and yaw motion of both wheelsets and car body as well as the roll motion of the car body. This characteristic phase locked frequency at about 1 Hz is, however, not present in the longitudinal displacement of wheelset. Regarding the longitudinal motion we see several characteristic frequencies between 2 Hz and 6 Hz, but none as low as 1 Hz.

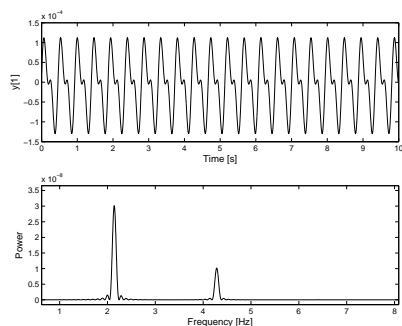
DOF	Empty	Water	Packed
y_1, y_{12}	2.14 Hz, 4.28 Hz	2.07 Hz, 4.15 Hz	1.93 Hz, 3.86 Hz, 5.30 Hz
y_3, y_{14}, y_{23}	1.07 Hz	1.04 Hz	0.96 Hz
y_{10}, y_{21}, y_{29}	1.07 Hz	1.04 Hz	0.96 Hz
y_{27}	1.07 Hz	1.04 Hz	0.96 Hz

Table 10.1: Characteristic frequencies at $v = 24$ m/s for suspension parameter set 1.

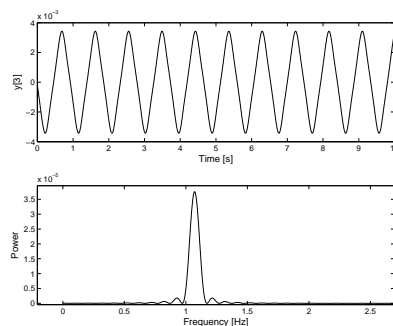
DOF	Empty	Water	Packed
y_1, y_{12}	2.7 Hz, 3.9 Hz	2.6 Hz, 5.2 Hz, 6.1 Hz	2.9 Hz, 5.8 Hz
y_3, y_{14}, y_{23}	1.36 Hz	1.31 Hz	1.46 Hz
y_{10}, y_{21}, y_{29}	1.36 Hz	1.31 Hz	1.46 Hz
y_{27}	1.36 Hz	1.31 Hz	1.46 Hz

Table 10.2: Characteristic frequencies at $v = 38$ m/s for suspension parameter set 2.

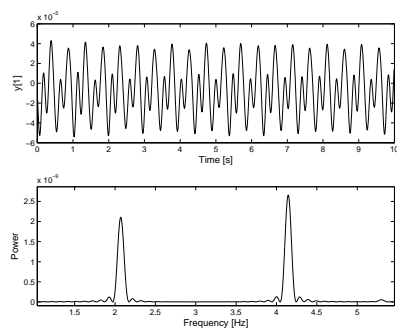
²i.e. suspension parameter set and cargo



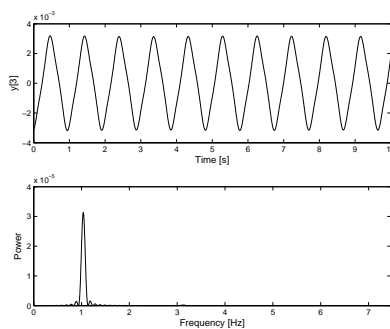
(a) Empty wagon.



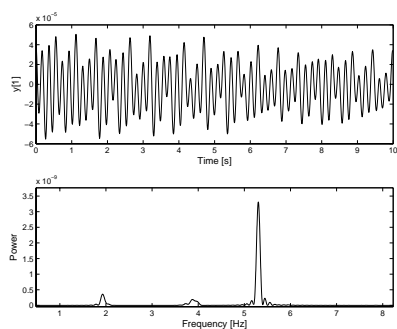
(b) Empty wagon.



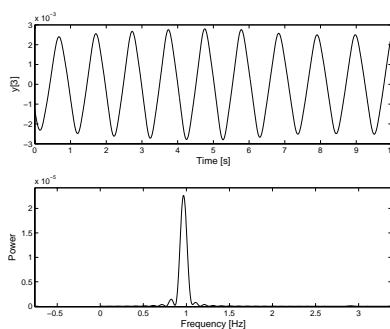
(c) Water loaded wagon.



(d) Water loaded wagon.

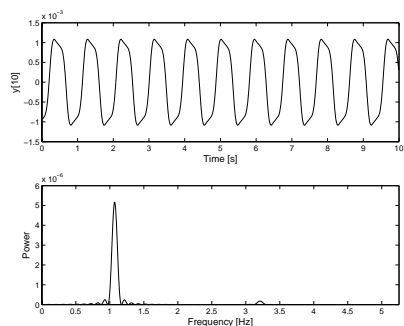


(e) Packed wagon.

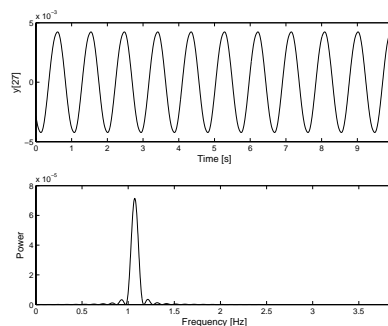


(f) Packed wagon.

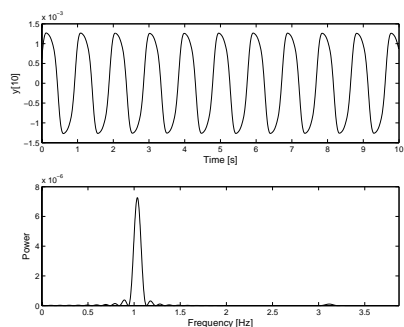
Figure 10.27: Frequency analysis at $v = 24$ m/s for suspension parameter set 1. (a), (c) and (e) illustrates the longitudinal displacement and frequency analysis for the front wheelset. (b), (d) and (f) illustrates the lateral displacement and frequency analysis for the front wheelset.



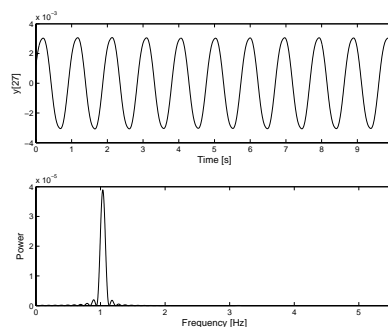
(a) Empty wagon.



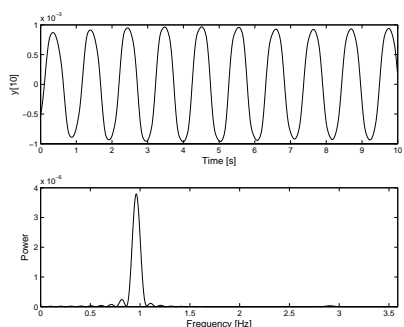
(b) Empty wagon.



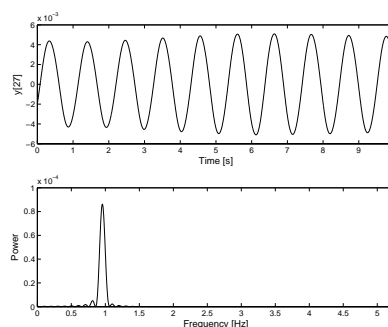
(c) Water loaded wagon.



(d) Water loaded wagon.

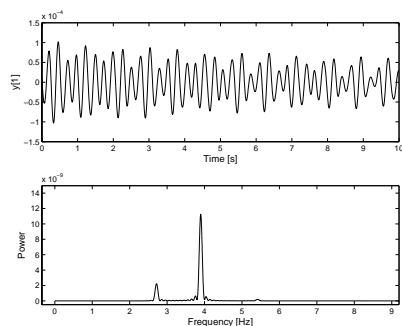


(e) Packed wagon.

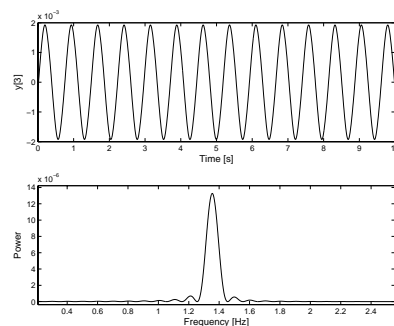


(f) Packed wagon.

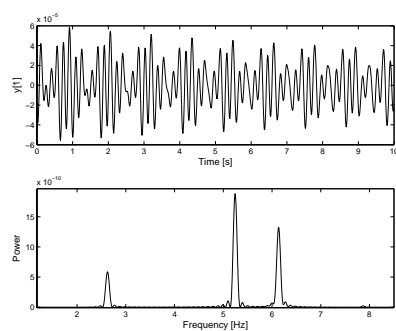
Figure 10.28: Frequency analysis at $v = 24$ m/s for suspension parameter set 1. (a), (c) and (e) illustrates the yaw motion and frequency analysis for the front wheelset. (b), (d) and (f) illustrates the roll motion and frequency analysis for the car body.



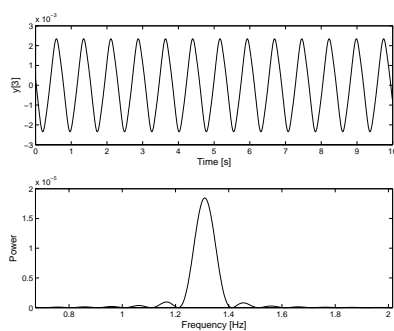
(a) Empty wagon.



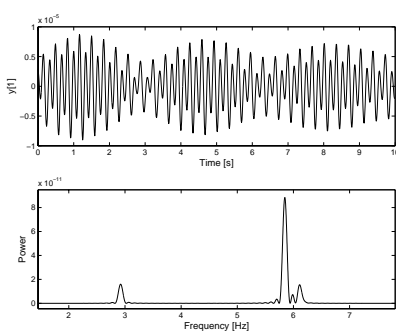
(b) Empty wagon.



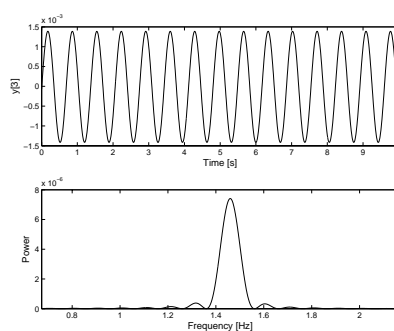
(c) Water loaded wagon.



(d) Water loaded wagon.

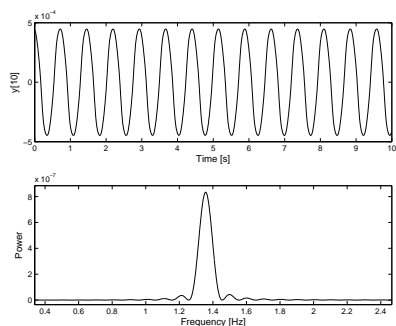


(e) Packed wagon.

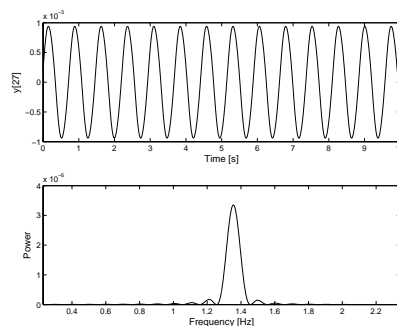


(f) Packed wagon.

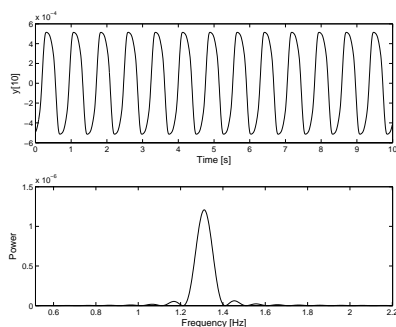
Figure 10.29: Frequency analysis at $v = 38$ m/s for suspension parameter set 2. (a), (c) and (e) illustrates the longitudinal displacement and frequency analysis for the front wheelset. (b), (d) and (f) illustrates the lateral displacement and frequency analysis for the front wheelset.



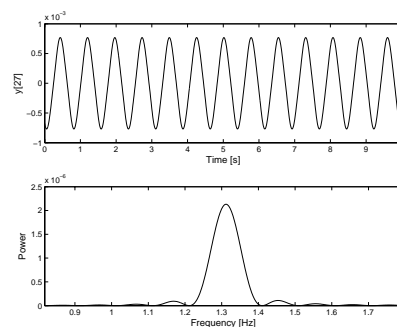
(a) Empty wagon.



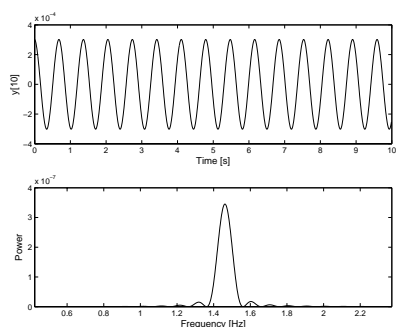
(b) Empty wagon.



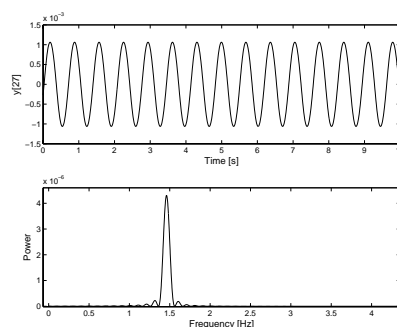
(c) Water loaded wagon.



(d) Water loaded wagon.



(e) Packed wagon.



(f) Packed wagon.

Figure 10.30: Frequency analysis at $v = 38$ m/s for suspension parameter set 2. (a), (c) and (e) illustrates the yaw motion and frequency analysis for the front wheelset. (b), (d) and (f) illustrates the roll motion and frequency analysis for the car body.

10.5 Summary

In this chapter we presented results in running the freight wagon model using the parabolic vertical UIC suspension model, under varying cargo conditions and UIC suspension parameters. This was all done on a straight and level track composed of UIC60 rails and a track gauge of 1435 mm. The freight wagon was equipped with S1002 wheel profiles. We here present a summary and commentary of results achieved.

In calculating bifurcation traces, we observed that there was a delay effect. We have showed that this effect may prevent seeing the fine structure in what a true bifurcation diagram of the system would look like, and without further analysis one can easily misdiagnose the type of Hopf bifurcations at the linear critical velocities.

The linear critical velocity is most correctly measured by observing the transition of conjugate eigenvalue pairs from the Jacobian across the imaginary axis. The nonlinear critical velocity does not seem to suffer from the delay effect as much as the linear critical velocity does, however this can not be completely discarded due to the possibility of ghost effects which saddle node bifurcations are known for, and thus yielding lengthy transient motion.

An interesting observation that yielded strange results in our bifurcation traces was that the period of oscillations grew large in certain intervals, and our choice to simulate for only 10 or 5 seconds at a time and sample the last 3 seconds did not permit us to sample over an entire period. This yielded maximum amplitudes which varied from step to step in the bifurcation traces, and could have been avoided by simulating for longer and sampling larger intervals for maximum amplitudes. However, had we done this, we would have perhaps missed this interesting period lengthening behaviour.

In observing the bifurcation diagrams, we see that adding load serves to improve the running behaviour of the freight wagon, at least in the linear sense. This is concluded based on that the linear critical velocity tends to increase. With respect to the nonlinear critical velocities in the cases of the empty and water loaded wagons, we can conclude that it is resistant to changes in load since it does not change much.

We also observed that simulations showed the worst stability of the Hbbills 311 wagon to reside in the medium fast velocity range between the linear and nonlinear critical velocities. At high speeds, no lateral impact of the wheelsets was observed, while at these medium speeds, we observed that hunting amplitudes increased and that the wheelset guidances were critical preventing derailment, at least when running with suspension parameter set 1.

With respect to the strange discontinuities in the bifurcation traces for suspension parameter set 1, we attributed these to how the wheelsets begin to impact against the car body. Simulations also confirmed that for parameter set 2 no lateral impact occurs. With respect to longitudinal impact, none was detected throughout all simulations and in all cases.

In the case with a packed wagon, the bifurcation type related to the linear critical

velocity changed significantly in the case of suspension parameter set 2, in that an expected subcritical bifurcation actually was supercritical. This surprise was also matched by the determination of a supercritical bifurcation in the case of an empty wagon running a suspension using parameter set 1. Both of these results were obscured by the delay effect, which could easily have prevented both facts from being discovered.

This leads us to the fact that in order to yield true bifurcation diagrams, time, processing power and care is needed, and none of them can come in too lacking an amount. This also raises questions about the actual bifurcation diagrams calculated, but the attractors traced on them *do* exist. However, the traces do *not* exclude the possibility of others existing.

In a general comparison between suspension types, we observed that motion tends to dampen out more strongly using suspension parameter set 2 (geometry matched) rather than parameter set 1 (frequency matched). This case was strengthened by the fact that amplitudes recorded in the bifurcation diagrams tend to be larger for parameter set 1 than for parameter set 2. Furthermore, the critical velocities for parameter set 2 are also larger than those for parameter set 1.

With respect to effect of dry friction, We have also been able to determine that the system does find new equilibria. This was evident in how a bifurcation trace did not return to the original low velocity center-track stable position that it started out with.

Ultimately, frequency analysis of the system indicated that components in the system do behave in a phase-locked manner, with some components oscillating at 2, 3 or 4 times the frequency of other components.

Chapter 11

Future Work

Possible improvements on our project reside mainly in alterations to a specific part of the C++ source code, namely the numerical Jacobi matrix estimator. In performing correctly scaled perturbations, and if still optimized for sparse Jacobi matrices, the simulation time would decrease and be more autonomous. This would mean we wouldn't have to restart simulations that hang on sudden poor estimations of the numerical Jacobi matrix.

An improvement can also be made in the wheel-rail tangential forces algorithm. Although SHE works fine in our case, if we wish to incorporate a model for running our freight wagon in low curvature radius curves, a better algorithm would be necessary. This is due to SHE's deficiency in predicting forces well in extreme motions of wheelsets. The RSGEO table would also be inaccurate to use, since our version relies on small yaw angles of the wheelsets. An option resides in incorporating Kalker's FASTSIM into the simulation, which would generate more accurate values as it is called continuously under simulation.

SDIRK itself can be improved upon, and Per Grove Thomsen has mentioned a solver named GERK (Generalized Runge-Kutta) that seems to offer better performance. This code is currently for MatLab only, but in the future may be converted to C++ and combined with an improved numerical Jacobi matrix estimator.

Mathematical models of the wheelsets and freight wagon elements could be modified in order to investigate medium and high frequency dynamic effects. This would necessitate modelling the wheelsets as an elastic structure, since it has vibrational modes in these frequency regimes. Truthfully, these considerations are only necessary for high velocities (circa 200 km/h and above), in which rail corrugation and wheel polygonization becomes significant. However, the point is not moot since Swedish railways plan on running freight wagons at 160 km/h on overnight service connections.

Future experimental work can be made in various fields, but mainly improvements on UIC double link suspension experimentation would be in order. Realistic loading of the linkages would be desirable, in order to perhaps avoid depending on an assumption of a

linear relation between freight load and suspension stiffness. The experimentation should be performed on UIC double linkages with correct pivot and hub profile geometries, both for linkages that are both new as well as worn.

It would also be desirable to improve analysis on longitudinal rolling and sliding conditions in the UIC link suspension. As it stands, this is not a significant deficiency in the case of straight and level track simulations, but negotiating curves can introduce incidents where the accuracy of the individual parameters come into play.

The element in the freight train model that further investigation would serve well is the damping in the vertical parabolic spring. A better vertical spring model is of interest, since linear damping in this direction is assumed, and which may not be accurate enough. A dry friction model combining Fancher's leaf spring model, and the data from DSB Drift on the parabolic spring could be combined in order to yield hysteresis loops for the parabolic spring as found in [6]. This has been tested in preliminary form in the **MatLab** source code, but ultimately accurate parameters for whatever model is chosen is of central interest.

In incorporating these improvements and suggestions, future work can be initiated on the behaviour of the freight wagon in negotiating curved track, where it is known from experience that the dynamics of rail vehicles worsen. Irregular track is also an option for study, but may necessitate changing the model of the freight wagon significantly, in order to consider medium and high frequency dynamics.

Finally, it would also be interesting to see the effect of asymmetry in the parameters of the suspension in the freight wagon, since different linkages could be in different states of maintenance. This might affect dynamics of the freight wagon significantly. Asymmetric analysis can also be extended to non uniform distribution of cargo within the freight car.

Chapter 12

Conclusion

This thesis presented a mathematical model of a Hbbills 311 freight wagon, and we were able to carry out various simulations on it. Various cargo configurations were examined, as well as different suspension parameters were tested.

It was seen that running characteristics are worst in the medium speed range, between the linear and nonlinear critical velocities. As velocities increase, the running characteristics improve in that the hunting motion decreases in amplitude, and wheelsets eventually cease impacting the wheelset guidance structures (suspension parameter set 1). This medium speed misbehaviour is known to exist in freight wagons running the UIC suspension.

Interestingly, it is evident that the wheelset guidance structures are important for the stability of the freight wagon. Without them, at least under suspension parameter set 1, the freight wagon derails in the medium speed range, where running characteristics seems worst.

A significant dynamic effect observed in our model is that of lateral impacts of the wheelset with the freight wagon guidance structures. On the other hand, longitudinal impacts do not occur.

Thus we can conclude that our model has yielded further insight into the running behaviour of the freight wagon investigated, and can be expanded upon in the future for further investigation.

Appendix A

Symbols

A.1 Latin Symbols

This section reintroduces and describes a series of mathematical symbols used throughout the text. This section concentrates solely on symbols based on the Latin alphabet. If a symbol lacks a value, it generally means that value is variable.

A.1.1 A to B

Symbol	Description	Value	Units
a	Lateral distance from center of mass of wheelset to suspension elements.	1.074	[m]
$a_{1..6}$	Distances from the center of mass of the wheelset to the contact forces $\tau_{1..6}$, respectively.		[m]
a_e	Contact ellipse major semi-axis.		[m]
$a_{e,0}$	Contact ellipse major semi-axis under static load from wheelset.		[m]
$a_{e,dyn}$	Contact ellipse major semi-axis under dynamic load from wheelset.		[m]
a_l	Distance from center of mass of the wheelset to the left contact point.		[m]
a_r	Distance from center of mass of the wheelset to the right contact point.		[m]
b	Lateral distance from center of mass of railcar to wheelset suspension elements.	1.074	[m]
b	Longitudinal clearance between wheelset and wheelset guidance.	0.025	[m]
b_e	Contact ellipse minor semi-axis.		[m]
$b_{e,0}$	Contact ellipse minor semi-axis under static load from wheelset.		[m]
$b_{e,dyn}$	Contact ellipse minor semi-axis under dynamic load from wheelset.		[m]

A.1.2 C to E

c	Lateral clearance between wheelset and wheelset guidance.	0.02 [m]
c	Average stiffness	[N m ⁻¹]
c_{\nearrow}	Loading stiffness.	[N m ⁻¹]
c_{\searrow}	Unloading stiffness.	[N m ⁻¹]
C_{11}	Kalker creepage coefficient.	[1]
C_{22}	Kalker creepage coefficient.	[1]
C_{23}	Kalker creepage coefficient.	[1]
C_l^r	Left wheel-rail contact force in the --direction of the rail coordinate system.	[N]
C_r^r	Right wheel-rail contact force in the --direction of the rail coordinate system.	[N]
C_l^w	Left wheel-rail contact force in the --direction of the wheelset coordinate system.	[N]
C_r^w	Right wheel-rail contact force in the --direction of the wheelset coordinate system.	[N]
d	Damping constant.	[N s m ⁻¹]
d_3	Height from the wagon underframe to the wagon floor.	0.265 [m]
d_4	Height from the wagon floor to the top of vertical wagon walls.	2.35 [m]
d_8	Car body cargo space length.	16.01 [m]
d_9	Car body cargo space width.	2.9 [m]
\mathbf{e}	Unit vector. See appendix C.	[1]

A.1.3 F to L

$F_{\cdot,ext}^r$	Exterior forces in the $\cdot = x, y, z$ coordinate direction of the inertial rail reference frame.	[N]
F_{res}	Restoring force.	[N]
F_x	Creep force in the x -direction of the contact coordinate system.	[N]
F_y	Creep force in the y -direction of the contact coordinate system.	[N]
\mathbf{F}_τ	Adjusted tangential creep force after adjustment by Shen-Hedrick-Elkins.	[N]
$\tilde{\mathbf{F}}_\tau$	Resulting tangential creep force prior to Shen-Hedrick-Elkins adjustment.	[N]
g	Acceleration due to gravity.	9.82 [m s ⁻²]
G	Shear modulus of steel.	$8.27 \cdot 10^{10}$ [N m ⁻²]
h	Vertical distance from center of mass of railcar to wheelset suspension elements	0.802* [m]
I_c	Moment of inertia for the car body about the $\cdot = x, y, z$ axis.	[kg m ²]
I_w	Moment of inertia for the wheelset about the $\cdot = x, y, z$ axis.	[kg m ²]
$I_{l1..2}$	Moment of inertia for the car body under roll and yaw. Used in the Maple code.	[kg m ²]
J_{ij}	The (i, j) 'th element in the Jacobi matrix.	[1]
k	Spring constant.	[N m ⁻¹]
$k_{1..4}$	Spring constants in the UIC suspension's lateral and longitudinal dynamics.	[N m ⁻¹]
l	Longitudinal distance from center of mass of railcar to wheelset suspension elements.	5.0 [m]
\mathbf{L}_C	Angular momentum about the center of mass and principal axes of the wheelset.	[kg m ² s ⁻¹]

A.1.4 M to Q

m_i	The i 'th particle's mass.	[kg]
m_c	Car body mass. Includes freight.	13563* [kg]
m_w	Wheelset mass.	1022 [kg]
M	Mass.	[kg]
M_0	Mass of the empty car body.	[kg]
M_{freight}	Mass of freight.	[kg]
${}_a\mathbf{M}_b$	Coordinate transformation matrix from a coordinates to b coordinates.	[1]
N	Normal force.	[N]
N_0	Normal force from static wheelset load.	[N]
N_{dyn}	Normal force from dynamic wheelset load.	[N]
$p_{x,1..2}$	Penetrations of the wheelset longitudinally, that give rise to contact forces $\tau_{1..2}$.	[m]
$p_{y,3..6}$	Penetrations of the wheelset laterally, that give rise to contact forces $\tau_{3..6}$.	[m]
q	Total penetration of a wheelset into the rail at a contact point.	[m]
q_0	Penetration of a wheelset into the rail at a contact point corresponding to the static load of the wheelset.	[m]
q_{dyn}	Penetration of a wheelset into the rail at a contact point corresponding to the dynamic load of the wheelset.	[m]
Δq	The difference in penetration (additional penetration) between a static and a dynamic load of the wheelset.	[m]
Δq_l	The left wheel's additional penetration.	[m]
Δq_r	The right wheel's additional penetration.	[m]

A.1.5 R to V

r_0	Basic rolling radius of the wheelset.	[m]
r_l	Rolling radius of the left wheel.	[m]
r_r	Rolling radius of the right wheel.	[m]
\mathbf{r}	Vector from the center of mass of the wheelset to the contact point.	[m]
\mathbf{r}_C	Vector from the origin to the center of mass of an object.	[m]
\mathbf{r}_i	Vector from the origin to the i 'th particle's center of mass.	[m]
R	Radius. Distance from point to center of consideration (moment of inertia calculations).	[m]
\mathbf{R}	Vector to the contact point on the $\cdot = w, r$ (wheel, rail).	[m]
s	Parametric variable used in differential succession.	[1]
S_l^r	Spring forces from the UIC suspension on the left side in the rail coordinate system in the $\cdot = x, y, z$ -directions.	- [N]
S_r^r	Spring forces from the UIC suspension on the right side in the rail coordinate system in the $\cdot = x, y, z$ -directions.	- [N]
T	Dry friction slider force.	[N]
$T_{0,1..4}$	Dry friction slider threshold forces for lateral and longitudinal UIC suspension models.	[N]
v_s	Rail car velocity.	[m s ⁻¹]
V	Rail car velocity.	[m s ⁻¹]
\mathbf{V}_c	Velocity of a contact point.	[m s ⁻¹]
\mathbf{V}_{trans}	Translational velocity of the wheelset.	[m s ⁻¹]
\mathbf{V}_{rot}	Rotational velocity of the wheelset.	[m s ⁻¹]

A.1.6 X to Y

x_d	Displacement of the wheelset in the x -coordinate of the rail coordinate system.	[m]
(X_r, Y_r, Z_r)	Euclidean coordinates in the rail reference frame. Inertial.	[1]
(X_w, Y_w, Z_w)	Euclidean coordinates in the wheelset reference frame. Not inertial.	[1]
(X_b, Y_b, Z_c)	Euclidean coordinates in the car body reference frame. Not inertial.	[1]
(X_c, Y_c, Z_c)	Euclidean coordinates in the contact point reference frame. Not inertial.	[1]
y_d	Displacement of the wheelset in the y -coordinate of the rail coordinate system.	[m]

A.2 Greek Symbols

This section reintroduces and describes a series of mathematical symbols used throughout the text. This section concentrates solely on symbols based on the Greek alphabet.

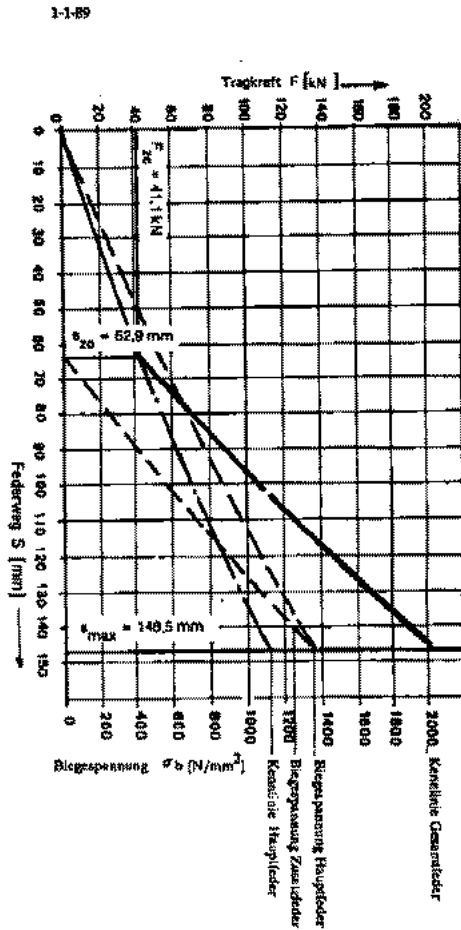
Symbol	Description	Value	Units
α	Angle between UIC links and vertical.		[1]
β	Angular velocity perturbation.		[s]
δ	Perturbation.		[·]
δ_l	Left wheel conicity.		[1]
δ_r	Right wheel conicity.		[1]
δ_l^r	Impact force, rail coordinate system, left wheel, $\cdot = x, y, z$ directions.		[N]
δ_r^r	Impact force, rail coordinate system, right wheel, $\cdot = x, y, z$ directions.		[N]
δ_l^w	Impact force, wheel coordinate system, left wheel, $\cdot = x, y, z$ directions.		[N]
δ_r^w	Impact force, wheel coordinate system, right wheel, $\cdot = x, y, z$ directions.		[N]
ϵ	$ \mathbf{F}_\tau / \tilde{\mathbf{F}}_\tau $		[1]
μ	Coefficient of friction.	0.15	[1]
μ_0	Deviation of c_{\nearrow} and c_{\searrow} stiffnesses from c .	0.07	[1]
ξ_l	Left wheel contact creep for $\cdot = x, y, s$: longitudinal, lateral and spin creeps.		[1], [1], [m^{-1}]
ξ_r	Right wheel contact creep for $\cdot = x, y, s$: longitudinal, lateral and spin creeps.		[1], [1], [m^{-1}]
ρ	Density.		[kg m^{-3}]
$\tau_{1..6}$	Impact forces on the wheelset.		[N m]
$\tau_{C,ext}$	Exterior torques on a center of mass.		[N m]
$\tau_{\cdot,ext}^w$	Exterior torque, wheelset coordinates, $\cdot = x, y, z$ directions.		[N m]
ϕ	Roll angle. Phase.		[1]
χ	Pitch angle.		[1]
ψ	Yaw angle.		[1]
ω	Angular frequency.		[s^{-1}]
ω_{rolling}	The UIC suspension's frequency when stick occurs in all joints.		[s^{-1}]
ω_{sliding}	The UIC suspension's frequency when sliding occurs in all joints.		[s^{-1}]
$\hat{\omega}$	Angular velocity of the wheelset coordinate system.		[s^{-1}]

Appendix B

Parabolic Spring Data

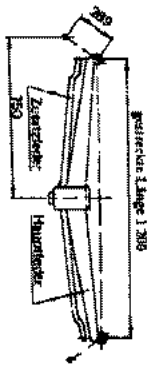
We here present the data curves which provided the stiffness parameters for the parabolic spring model. These curves, as can easily be seen, were inspirational to the fact that we used a piecewise linear spring-damper system to represent the parabolic spring model.

Parabolfeder mit progressiver Kennlinie für 22,5 t Radsetlast für Wagen mit zwei Radsetzen - Verwendungsmerkmale -



Federkennwerte im DS-Cataloge		Symbol	Einheit	Wert
Max. zulässige Radsetlast im S- und SS-Vorteil		P	t	22,5
Mittlere spezifische Federung *		C ₂₁	mm/kN	1,25 (0,55) ± 7%
Mittlere Radsetlast *		C ₂₂	mm/kN	0,55 (0,25) ± 7%
Federhöhe bei 20 kN Belastung		S ₂₀	mm	41,1
Federhöhe bei Eingriff der Zusatzfeder		S _{2c}	mm	62,9
Durchbiegung bei Eingriff der Zusatzfeder		H _{2Dz}	mm	150
Federhöhe bei 20 kN Belastung		H _{2Dz}	mm	150
Max. zulässige Durchbiegung seitlich		f _{max}	mm	146,5
sprichend der zulässigen Höchstbelastung (* f _{max} zul = 1500 N/mm ²)				

* Nach Prüfverfahren UIC-Merkblatt Nr. 321



5 1 7
V E
ANLAGE 10c

Figure B.1: Parabolic spring data.

Appendix C

Coordinate Transformations

In this chapter we derive the transformation matrices which provide the connection between the coordinate systems we use to describe the model. This is a matter of changing basis in a three dimensional Euclidean vector space.

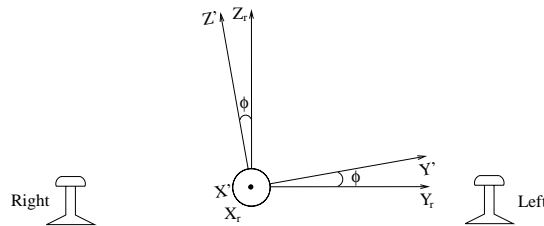


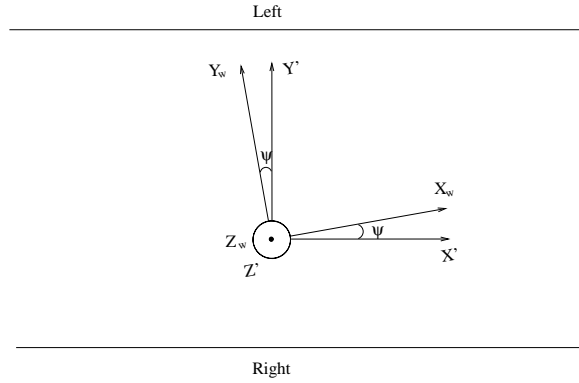
Figure C.1: Rotate the angle ϕ around x .

Firstly, we find the transformation matrix between the rail coordinate system and the wheelset coordinate system. We rotate the rail coordinate system with the angle ϕ around its own x axis, and end up with the coordinate system denoted (X', Y', Z') (see figure C.1). Let the canonical basis for the rail and (X', Y', Z') coordinate system be $\{\mathbf{e}_{rx}, \mathbf{e}_{ry}, \mathbf{e}_{rz}\}$ and $\{\mathbf{e}_{x'}, \mathbf{e}_{y'}, \mathbf{e}_{z'}\}$, respectively. The matrix M_ϕ that switches rail coordinates to (X', Y', Z') coordinates is the coordinate matrix for $\{\mathbf{e}_{rx}, \mathbf{e}_{ry}, \mathbf{e}_{rz}\}$ with respect to the basis $\{\mathbf{e}_{x'}, \mathbf{e}_{y'}, \mathbf{e}_{z'}\}$. Thus

$$\mathbf{e}_x = \begin{bmatrix} 1 \\ 0 \\ 0 \end{bmatrix} \quad \mathbf{e}_y = \begin{bmatrix} 0 \\ \cos \phi \\ -\sin \phi \end{bmatrix} \quad \mathbf{e}_z = \begin{bmatrix} 0 \\ \sin \phi \\ \cos \phi \end{bmatrix}$$

i.e.

$$\mathbf{M}_\phi = \begin{bmatrix} 1 & 0 & 0 \\ 0 & \cos \phi & \sin \phi \\ 0 & -\sin \phi & \cos \phi \end{bmatrix}$$

Figure C.2: Rotation ψ around z' .

We now proceed by rotating the (X', Y', Z') coordinate system ψ around its own z' axis and we end up with the wheelset coordinate system. The matrix that switches (X', Y', Z') coordinates to (X_w, Y_w, Z_w) coordinates is the coordinate matrix for $\{\mathbf{e}_{x'}, \mathbf{e}_{y'}, \mathbf{e}_{z'}\}$ with respect to the basis $\{\mathbf{e}_{wx}, \mathbf{e}_{wy}, \mathbf{e}_{wz}\}$.

$$\mathbf{e}_x = \begin{bmatrix} \cos \psi \\ -\sin \psi \\ 0 \end{bmatrix} \quad \mathbf{e}_y = \begin{bmatrix} \sin \psi \\ \cos \psi \\ 0 \end{bmatrix} \quad \mathbf{e}_z = \begin{bmatrix} 0 \\ 0 \\ 1 \end{bmatrix}$$

Thus

$$\mathbf{M}_\psi = \begin{bmatrix} \cos \psi & \sin \psi & 0 \\ -\sin \psi & \cos \psi & 0 \\ 0 & 0 & 1 \end{bmatrix}$$

The matrix that switches rail coordinates to wheelset coordinates is

$${}_w\mathbf{M}_r = \mathbf{M}_\psi \cdot \mathbf{M}_\phi = \begin{bmatrix} \cos \psi & \sin \psi \cos \phi & \sin \psi \sin \phi \\ -\sin \psi & \cos \psi \cos \phi & \cos \psi \sin \phi \\ 0 & -\sin \phi & \cos \phi \end{bmatrix} \approx \begin{bmatrix} 1 & \psi & 0 \\ -\psi & 1 & \phi \\ 0 & -\phi & 1 \end{bmatrix}$$

We now seek the transformation matrix that converts contact coordinates to wheelset coordinates and it is found in precisely the same manner as before (see figure C.3). For the left wheel the coordinate matrix for $\{\mathbf{e}_{cx}, \mathbf{e}_{cy}, \mathbf{e}_{cz}\}$ with respect to the basis $\{\mathbf{e}_{wx}, \mathbf{e}_{wy}, \mathbf{e}_{wz}\}$ is

$$\mathbf{e}_x = \begin{bmatrix} 1 \\ 0 \\ 0 \end{bmatrix} \quad \mathbf{e}_y = \begin{bmatrix} 0 \\ \cos \delta_l \\ \sin \delta_l \end{bmatrix} \quad \mathbf{e}_z = \begin{bmatrix} 0 \\ -\sin \delta_l \\ \cos \delta_l \end{bmatrix}$$

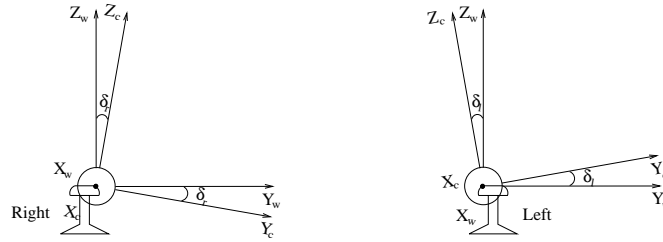


Figure C.3:

Hence

$${}^w\mathbf{M}_{cl} = \begin{bmatrix} 1 & 0 & 0 \\ 0 & \cos \delta_l & -\sin \delta_l \\ 0 & \sin \delta_l & \cos \delta_l \end{bmatrix}$$

For the right wheel we get

$$\mathbf{e}_x = \begin{bmatrix} 1 \\ 0 \\ 0 \end{bmatrix} \quad \mathbf{e}_y = \begin{bmatrix} 0 \\ \cos \delta_r \\ -\sin \delta_r \end{bmatrix} \quad \mathbf{e}_z = \begin{bmatrix} 0 \\ \sin \delta_r \\ \cos \delta_r \end{bmatrix}$$

Therefore

$${}^w\mathbf{M}_{cr} = \begin{bmatrix} 1 & 0 & 0 \\ 0 & \cos \delta_r & \sin \delta_r \\ 0 & -\sin \delta_r & \cos \delta_r \end{bmatrix}$$

An important property with the transformation matrices ${}^w\mathbf{M}_r$, ${}^w\mathbf{M}_{cl}$ and ${}^w\mathbf{M}_{cr}$ is that they are orthogonal. This means that

$$\begin{aligned} {}^r\mathbf{M}_w &= {}^w\mathbf{M}_r^{-1} = {}^w\mathbf{M}_r^T \\ {}^{cl}\mathbf{M}_w &= {}^w\mathbf{M}_{cl}^{-1} = {}^w\mathbf{M}_{cl}^T \\ {}^{cr}\mathbf{M}_w &= {}^w\mathbf{M}_{cr}^{-1} = {}^w\mathbf{M}_{cr}^T \end{aligned}$$

We are also able to find the transformation matrices that converts contact coordinates to rail coordinates and vice versa. We utilize the addition formulas and get

$$\begin{aligned}
{}_r\mathbf{M}_{cl} &= {}_r\mathbf{M}_w \cdot {}_w\mathbf{M}_{cl} \\
&= \begin{bmatrix} \cos \psi & -\sin \psi & 0 \\ \sin \psi \cos \phi & \cos \psi \cos \phi & -\sin \phi \\ \sin \psi \sin \phi & \cos \psi \sin \phi & \cos \phi \end{bmatrix} \cdot \begin{bmatrix} 1 & 0 & 0 \\ 0 & \cos \delta_l & -\sin \delta_l \\ 0 & \sin \delta_l & \cos \delta_l \end{bmatrix} \\
&\approx \begin{bmatrix} 1 & -\psi \cos \delta_l & \psi \sin \delta_l \\ \psi & \cos(\delta_l + \phi) & -\sin(\delta_l + \phi) \\ 0 & \sin(\delta_l + \phi) & \cos(\delta_l + \phi) \end{bmatrix}
\end{aligned}$$

$$\begin{aligned}
{}_r\mathbf{M}_{cr} &= {}_r\mathbf{M}_w \cdot {}_w\mathbf{M}_{cr} \\
&\approx \begin{bmatrix} 1 & -\psi \cos \delta_r & -\psi \sin \delta_r \\ \psi & \cos(\delta_r - \phi) & \sin(\delta_r - \phi) \\ 0 & -\sin(\delta_r - \phi) & \cos(\delta_r - \phi) \end{bmatrix}
\end{aligned}$$

$$\begin{aligned}
{}_{cl}\mathbf{M}_r &= {}_{cl}\mathbf{M}_w \cdot {}_w\mathbf{M}_r \\
&\approx \begin{bmatrix} 1 & \psi & 0 \\ -\psi \cos \delta_l & \cos(\delta_l + \phi) & \sin(\delta_l + \phi) \\ \psi \sin \delta_l & -\sin(\delta_l + \phi) & \cos(\delta_l + \phi) \end{bmatrix}
\end{aligned}$$

$$\begin{aligned}
{}_{cr}\mathbf{M}_r &= {}_{cr}\mathbf{M}_w \cdot {}_w\mathbf{M}_r \\
&\approx \begin{bmatrix} 1 & \psi & 0 \\ -\psi \cos \delta_r & \cos(\delta_r - \phi) & -\sin(\delta_r - \phi) \\ -\psi \sin \delta_r & \sin(\delta_r - \phi) & \cos(\delta_r - \phi) \end{bmatrix}
\end{aligned}$$

A complete list of the rotational matrices used is presented below

$$\begin{aligned}
{}_i\mathbf{M}_r &= \begin{bmatrix} 1 & \psi & 0 \\ -\psi & 1 & \phi \\ 0 & -\phi & 1 \end{bmatrix} && \text{(rail to car body)} \\
{}_w\mathbf{M}_r &= \begin{bmatrix} 1 & \psi & 0 \\ -\psi & 1 & \phi \\ 0 & -\phi & 1 \end{bmatrix} && \text{(rail to wheelset)} \\
{}_r\mathbf{M}_w &= \begin{bmatrix} 1 & -\psi & 0 \\ \psi & 1 & -\phi \\ 0 & \phi & 1 \end{bmatrix} && \text{(wheelset to rail)} \\
{}_w\mathbf{M}_{cl} &= \begin{bmatrix} 1 & 0 & 0 \\ 0 & \cos \delta_l & -\sin \delta_l \\ 0 & \sin \delta_l & \cos \delta_l \end{bmatrix} && \text{(contact left to wheelset)} \\
{}_w\mathbf{M}_{cr} &= \begin{bmatrix} 1 & 0 & 0 \\ 0 & \cos \delta_r & \sin \delta_r \\ 0 & -\sin \delta_r & \cos \delta_r \end{bmatrix} && \text{(contact right to wheelset)} \\
{}_{cl}\mathbf{M}_w &= \begin{bmatrix} 1 & 0 & 0 \\ 0 & \cos \delta_l & \sin \delta_l \\ 0 & -\sin \delta_l & \cos \delta_l \end{bmatrix} && \text{(wheelset to contact left)} \\
{}_{cr}\mathbf{M}_w &= \begin{bmatrix} 1 & 0 & 0 \\ 0 & \cos \delta_r & -\sin \delta_r \\ 0 & \sin \delta_r & \cos \delta_r \end{bmatrix} && \text{(wheelset to contact right)} \\
{}_r\mathbf{M}_{cl} &= \begin{bmatrix} 1 & -\psi \cos \delta_l & \psi \sin \delta_l \\ \psi \cos(\delta_l + \phi) & -\sin(\delta_l + \phi) \\ 0 & \sin(\delta_l + \phi) & \cos(\delta_l + \phi) \end{bmatrix} && \text{(contact left to rail)} \\
{}_r\mathbf{M}_{cr} &= \begin{bmatrix} 1 & -\psi \cos \delta_r & -\psi \sin \delta_r \\ \psi \cos(\delta_r - \phi) & \sin(\delta_r - \phi) \\ 0 & -\sin(\delta_r - \phi) & \cos(\delta_r - \phi) \end{bmatrix} && \text{(contact right to rail)} \\
{}_{cl}\mathbf{M}_r &= \begin{bmatrix} 1 & \psi & 0 \\ -\psi \cos \delta_l & \cos(\delta_l + \phi) & \sin(\delta_l + \phi) \\ \psi \sin \delta_l & -\sin(\delta_l + \phi) & \cos(\delta_l + \phi) \end{bmatrix} && \text{(rail to contact left)} \\
{}_{cr}\mathbf{M}_r &= \begin{bmatrix} 1 & \psi & 0 \\ -\psi \cos \delta_r & \cos(\delta_r - \phi) & -\sin(\delta_r - \phi) \\ -\psi \sin \delta_r & \sin(\delta_r - \phi) & \cos(\delta_r - \phi) \end{bmatrix} && \text{(rail to contact right)}
\end{aligned}$$

Appendix D

Creepage

In this chapter we will derive the velocity of the contact point relative to the rail. For this we use a new set of coordinate systems that are similar to the previously defined coordinate systems, except that they are fixed in time. One could consider these new coordinate systems as a snapshot of the original ones at a specific instance in time. We denote these new coordinate systems by (X'_r, Y'_r, Z'_r) , (X'_w, Y'_w, Z'_w) and (X'_c, Y'_c, Z'_c) . The task is to find the velocity of the contact points in reference to (X'_c, Y'_c, Z'_c) , i.e. the velocity of the contact point relative to the rail.

In general, the velocity of a point on a rigid body consist of two parts. Firstly, there is a contribution due to the translational velocity of the body, and secondly, the angular velocity of the body. With respect to our problem we find that the velocity of the contact point is a composition of the translational velocity of the center of mass and rotational velocity around the center point of the wheelset. Thus, the velocity of the contact point is

$$\mathbf{V}_c = \mathbf{V}_{trans} + \mathbf{V}_{rot}$$

The translational velocity of the center of mass is

$$\mathbf{V}_{trans} = (V + \dot{x}) \cdot \mathbf{e}'_{rx} + \dot{y} \cdot \mathbf{e}'_{ry} + \dot{z} \cdot \mathbf{e}'_{rz}$$

The rotational velocity around the center of mass is

$$\mathbf{V}_{rot} = \boldsymbol{\omega} \times \mathbf{r}$$

where

$$\boldsymbol{\omega} = \dot{\phi} \cdot \mathbf{e}'_{wx} + \dot{\chi} \cdot \mathbf{e}'_{wy} + \dot{\psi} \cdot \mathbf{e}'_{wz}$$

The vector from the center of mass of the wheelset to the contact point is

$$\mathbf{r} = \begin{cases} 0 \cdot \mathbf{e}'_{wx} + a_l \cdot \mathbf{e}'_{wy} - r_l \cdot \mathbf{e}'_{wz} & \text{left contact point} \\ 0 \cdot \mathbf{e}'_{wx} - a_r \cdot \mathbf{e}'_{wy} - r_r \cdot \mathbf{e}'_{wz} & \text{right contact point} \end{cases}$$

In reference to (X'_w, Y'_w, Z'_w) we find regarding the left contact point

$$\begin{aligned}
\mathbf{V}_{cl} &= {}_w\mathbf{M}_r \begin{bmatrix} V + \dot{x} \\ \dot{y} \\ \dot{z} \end{bmatrix} + \begin{bmatrix} \dot{\phi} \\ \dot{\chi} \\ \dot{\psi} \end{bmatrix} \times \begin{bmatrix} 0 \\ a_l \\ -r_l \end{bmatrix} \\
&= \begin{bmatrix} 1 & \psi & 0 \\ -\psi & 1 & \phi \\ 0 & -\phi & 1 \end{bmatrix} \begin{bmatrix} V + \dot{x} \\ \dot{y} \\ \dot{z} \end{bmatrix} + \begin{bmatrix} \dot{\phi} \\ \dot{\chi} \\ \dot{\psi} \end{bmatrix} \times \begin{bmatrix} 0 \\ a_l \\ -r_l \end{bmatrix} \\
&= \begin{bmatrix} V + \dot{x} + \psi\dot{y} - r_l\dot{\chi} - a_l\dot{\psi} \\ -\psi(V + \dot{x}) + \dot{y} + \phi\dot{z} + r_l\dot{\phi} \\ -\phi\dot{y} + \dot{z} + a_l\dot{\phi} \end{bmatrix}
\end{aligned}$$

and for the right contact point the result is

$$\mathbf{V}_{cr} = \begin{bmatrix} V + \dot{x} + \psi\dot{y} - r_r\dot{\chi} + a_r\dot{\psi} \\ -\psi(V + \dot{x}) + \dot{y} + \phi\dot{z} + r_r\dot{\phi} \\ -\phi\dot{y} + \dot{z} - a_r\dot{\phi} \end{bmatrix}$$

In reference to (X'_c, Y'_c, Z'_c) we now find

$$\begin{aligned}
\mathbf{V}_{cl} &= {}_{cl}\mathbf{M}_w \begin{bmatrix} V + \dot{x} + \psi\dot{y} - r_l\dot{\chi} - a_l\dot{\psi} \\ -\psi(V + \dot{x}) + \dot{y} + \phi\dot{z} + r_l\dot{\phi} \\ -\phi\dot{y} + \dot{z} + a_l\dot{\phi} \end{bmatrix} \\
&= \begin{bmatrix} 1 & 0 & 0 \\ 0 & \cos \delta_l & \sin \delta_l \\ 0 & -\sin \delta_l & \cos \delta_l \end{bmatrix} \begin{bmatrix} V + \dot{x} + \psi\dot{y} - r_l\dot{\chi} - a_l\dot{\psi} \\ -\psi(V + \dot{x}) + \dot{y} + \phi\dot{z} + r_l\dot{\phi} \\ -\phi\dot{y} + \dot{z} + a_l\dot{\phi} \end{bmatrix} \\
&= \begin{bmatrix} V + \dot{x} + \psi\dot{y} - r_l\dot{\chi} - a_l\dot{\psi} \\ (-\psi(V + \dot{x}) + \dot{y} + \phi\dot{z} + r_l\dot{\phi}) \cos \delta_l + (-\phi\dot{y} + \dot{z} + a_l\dot{\phi}) \sin \delta_l \\ -(-\psi(V + \dot{x}) + \dot{y} + \phi\dot{z} + r_l\dot{\phi}) \sin \delta_l + (-\phi\dot{y} + \dot{z} + a_l\dot{\phi}) \cos \delta_l \end{bmatrix} \\
&\approx \begin{bmatrix} V + \dot{x} - r_l\dot{\chi} - a_l\dot{\psi} \\ (-\psi V + \dot{y} + r_l\dot{\phi}) \cos \delta_l + (\dot{z} + a_l\dot{\phi}) \sin \delta_l \\ -(-\psi V + \dot{y} + r_l\dot{\phi}) \sin \delta_l + (\dot{z} + a_l\dot{\phi}) \cos \delta_l \end{bmatrix}
\end{aligned}$$

and

$$\begin{aligned}
\mathbf{V}_{cr} &= {}_{cr}\mathbf{M}_w \begin{bmatrix} V + \dot{x} + \psi\dot{y} - r_r\dot{\chi} + a_r\dot{\psi} \\ -\psi(V + \dot{x}) + \dot{y} + \phi\dot{z} + r_r\dot{\phi} \\ -\phi\dot{y} + \dot{z} - a_r\dot{\phi} \end{bmatrix} \\
&= \begin{bmatrix} 1 & 0 & 0 \\ 0 & \cos \delta_r & -\sin \delta_r \\ 0 & \sin \delta_r & \cos \delta_r \end{bmatrix} \begin{bmatrix} V + \dot{x} + \psi\dot{y} - r_r\dot{\chi} + a_r\dot{\psi} \\ -\psi(V + \dot{x}) + \dot{y} + \phi\dot{z} + r_r\dot{\phi} \\ -\phi\dot{y} + \dot{z} - a_r\dot{\phi} \end{bmatrix} \\
&= \begin{bmatrix} V + \dot{x} + \psi\dot{y} - r_r\dot{\chi} + a_r\dot{\psi} \\ (-\psi(V + \dot{x}) + \dot{y} + \phi\dot{z} + r_r\dot{\phi}) \cos \delta_r - (-\phi\dot{y} + \dot{z} - a_r\dot{\phi}) \sin \delta_r \\ (-\psi(V + \dot{x}) + \dot{y} + \phi\dot{z} + r_r\dot{\phi}) \sin \delta_r + (-\phi\dot{y} + \dot{z} - a_r\dot{\phi}) \cos \delta_r \end{bmatrix} \\
&\approx \begin{bmatrix} V + \dot{x} - r_r\dot{\chi} + a_r\dot{\psi} \\ (-\psi V + \dot{y} + r_r\dot{\phi}) \cos \delta_r - (\dot{z} - a_r\dot{\phi}) \sin \delta_r \\ (-\psi V + \dot{y} + r_r\dot{\phi}) \sin \delta_r + (\dot{z} - a_r\dot{\phi}) \cos \delta_r \end{bmatrix}
\end{aligned}$$

The longitudinal and lateral creep are defined by

$$\begin{aligned}\xi_{\text{long}} &= \frac{v_{\text{long,wheel}} - v_{\text{long,rail}}}{V} \\ \xi_{\text{lat}} &= \frac{v_{\text{lat,wheel}} - v_{\text{lat,rail}}}{V}\end{aligned}$$

Since the rail is assumed to be fixed we find

$$\begin{aligned}\xi_{lx} &= 1 - \frac{r_l \dot{\chi}}{V} + \frac{\dot{x} - a_l \dot{\psi}}{V} \\ \xi_{rx} &= 1 - \frac{r_r \dot{\chi}}{V} + \frac{\dot{x} + a_r \dot{\psi}}{V} \\ \xi_{ly} &= \left(-\psi + \frac{\dot{y} + r_l \dot{\phi}}{V} \right) \cos \delta_l + \frac{\dot{z} + a_l \dot{\phi}}{V} \sin \delta_l \\ \xi_{ry} &= \left(-\psi + \frac{\dot{y} + r_r \dot{\phi}}{V} \right) \cos \delta_r - \frac{\dot{z} - a_r \dot{\phi}}{V} \sin \delta_r\end{aligned}$$

where we have neglected second order terms.

Finally, the spin creep terms are defined as the rotation around the normal to the contact plane normalized by the velocity. First, we have to find the angular velocity of the wheelset in reference to (X'_c, Y'_c, Z'_c) .

$$\begin{aligned}\omega_{cl} &= {}_{cl}\mathbf{M}_w \cdot \omega \\ &= \begin{bmatrix} 1 & 0 & 0 \\ 0 & \cos \delta_l & \sin \delta_l \\ 0 & -\sin \delta_l & \cos \delta_l \end{bmatrix} \begin{bmatrix} \dot{\phi} \\ \dot{\chi} \\ \dot{\psi} \end{bmatrix} \\ &= \begin{bmatrix} \dot{\phi} \\ \dot{\chi} \cos \delta_l + \dot{\psi} \sin \delta_l \\ -\dot{\chi} \sin \delta_l + \dot{\psi} \cos \delta_l \end{bmatrix}\end{aligned}$$

$$\begin{aligned}\omega_{cr} &= {}_{cr}\mathbf{M}_w \cdot \omega \\ &= \begin{bmatrix} 1 & 0 & 0 \\ 0 & \cos \delta_r & -\sin \delta_r \\ 0 & \sin \delta_r & \cos \delta_r \end{bmatrix} \begin{bmatrix} \dot{\phi} \\ \dot{\chi} \\ \dot{\psi} \end{bmatrix} \\ &= \begin{bmatrix} \dot{\phi} \\ \dot{\chi} \cos \delta_r - \dot{\psi} \sin \delta_r \\ \dot{\chi} \sin \delta_r + \dot{\psi} \cos \delta_r \end{bmatrix}\end{aligned}$$

Thus

$$\begin{aligned}\xi_{ls} &= \frac{-\dot{\chi} \sin \delta_l + \dot{\psi} \cos \delta_l}{V} \\ \xi_{rs} &= \frac{\dot{\chi} \sin \delta_r + \dot{\psi} \cos \delta_r}{V}\end{aligned}$$

Appendix E

Additional Penetration

In this chapter we will derive the expressions we have used to calculate the additional penetration due to the roll and vertical motion of the wheelset. This additional penetration combined with the static penetration from the RSGEO table enables us to compute the normal force dynamically.

Firstly, we find the vector from the contact point on the wheel to the contact point on the rail (see Figure E.1 and E.2 for details). For the left wheel we get

$$\begin{aligned}
 \mathbf{R}_r - \mathbf{R}_w &= \begin{bmatrix} x_{Rl} \\ a_{Rl} \\ z_{Rl} \end{bmatrix} - \left(\begin{bmatrix} x \\ y \\ z \end{bmatrix} + {}_r\mathbf{M}_w \cdot \begin{bmatrix} 0 \\ a_l \\ -r_l \end{bmatrix} \right) \\
 &= \begin{bmatrix} x_{Rl} - x \\ a_{Rl} - y \\ z_{Rl} - z \end{bmatrix} - \begin{bmatrix} 1 & -\psi & 0 \\ \psi & 1 & -\phi \\ 0 & \phi & 1 \end{bmatrix} \cdot \begin{bmatrix} 0 \\ a_l \\ -r_l \end{bmatrix} \\
 &= \begin{bmatrix} x_{Rl} - x + \psi a_l \\ a_{Rl} - y - a_l - \phi r_l \\ z_{Rl} - z - \phi a_l + r_l \end{bmatrix}
 \end{aligned}$$

We exclude the term $z_{Rl} + r_l$ because it is not a part of the *additional* penetration. Furthermore, we need to switch to the contact coordinate system, since the penetration is the z -component of this.

$$\begin{aligned}
 \Delta \mathbf{P} &= {}_{cl}\mathbf{M}_r \cdot \begin{bmatrix} x_{Rl} - x + \psi a_l \\ a_{Rl} - y - a_l - \phi r_l \\ -z - \phi a_l \end{bmatrix} \\
 &= \begin{bmatrix} 1 & \psi & 0 \\ -\psi \cos \delta_l & \cos(\delta_l + \phi) & \sin(\delta_l + \phi) \\ \psi \sin \delta_l & -\sin(\delta_l + \phi) & \cos(\delta_l + \phi) \end{bmatrix} \cdot \begin{bmatrix} x_{Rl} - x + \psi a_l \\ a_{Rl} - y - a_l - \phi r_l \\ -z - \phi a_l \end{bmatrix}
 \end{aligned}$$

The additional penetration is

$$\begin{aligned}\Delta P_{add,l} &= \psi(x_{Rl} - x + \psi a_l) \sin \delta_l - (a_{Rl} - y - a_l - \phi r_l) \sin(\delta_l + \phi) \\ &\quad + (-z - \phi a_l) \cos(\delta_l + \phi) \\ &\approx -(a_{Rl} - y - a_l - \phi r_l) \sin(\delta_l + \phi) + (-z - \phi a_l) \cos(\delta_l + \phi)\end{aligned}$$

We follow the same procedure for the right wheel and we get

$$\begin{aligned}\mathbf{R}_r - \mathbf{R}_w &= \begin{bmatrix} x_{Rr} \\ -a_{Rr} \\ z_{Rr} \end{bmatrix} - \left(\begin{bmatrix} x \\ y \\ z \end{bmatrix} + {}_r\mathbf{M}_w \cdot \begin{bmatrix} 0 \\ -a_r \\ -r_r \end{bmatrix} \right) \\ &= \begin{bmatrix} x_{Rr} - x \\ -a_{Rr} - y \\ z_{Rr} - y \end{bmatrix} - \begin{bmatrix} 1 & -\psi & 0 \\ \psi & 1 & -\phi \\ 0 & \phi & 1 \end{bmatrix} \cdot \begin{bmatrix} 0 \\ -a_r \\ -r_r \end{bmatrix} \\ &= \begin{bmatrix} x_{Rr} - x - \psi a_r \\ -a_{Rr} - y + a_r - \phi r_r \\ z_{Rr} - z + \phi a_r + r_r \end{bmatrix}\end{aligned}$$

$$\begin{aligned}\Delta \mathbf{P} &= {}_{cr}\mathbf{M}_r \cdot \begin{bmatrix} x_{Rr} - x - \psi a_r \\ -a_{Rr} - y + a_r - \phi r_r \\ -z + \phi a_r \end{bmatrix} \\ &= \begin{bmatrix} 1 & \psi & 0 \\ -\psi \cos \delta_r & \cos(\delta_r - \phi) & -\sin(\delta_r - \phi) \\ -\psi \sin \delta_r & \sin(\delta_r - \phi) & \cos(\delta_r - \phi) \end{bmatrix} \cdot \begin{bmatrix} x_{Rr} - x - \psi a_r \\ -a_{Rr} - y + a_r - \phi r_r \\ -z + \phi a_r \end{bmatrix}\end{aligned}$$

The additional penetration is

$$\begin{aligned}\Delta P_{add,r} &= -\psi(x_{Rr} - x - \psi a_r) \sin \delta_r + (-a_{Rr} - y + a_r - \phi r_r) \sin(\delta_r - \phi) \\ &\quad + (-z + \phi a_r) \cos(\delta_r - \phi) \\ &\approx (-a_{Rr} - y + a_r - \phi r_r) \sin(\delta_r - \phi) + (-z + \phi a_r) \cos(\delta_r - \phi)\end{aligned}$$

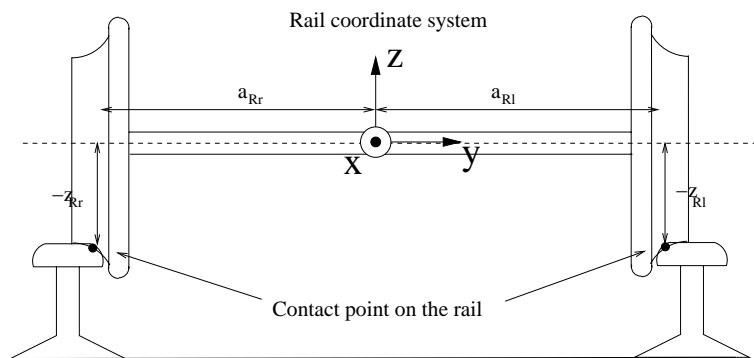


Figure E.1:

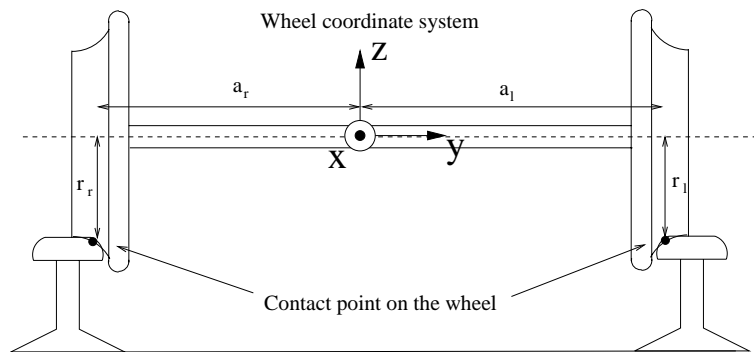


Figure E.2:

Appendix F

Differential Succession of the Dry Friction Element

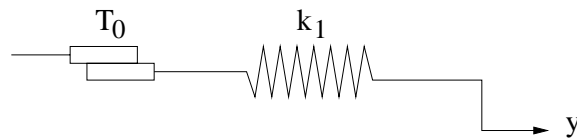


Figure F.1: Dry friction element.

We consider the dry friction element shown in figure F.1. The continuity condition for this element is

$$\dot{T} = k_1(-\dot{y} - v_s) \quad (\text{F.1})$$

The restoring force is bounded by Coulomb friction law, which is illustrated in figure F.2. It is important to know that this figure does *not* represent a mathematical *function*. Due to the non smooth characteristic of the friction force we make a differential succession in order to improve the numerical solution process.

For $|T| < T_0$ the sliding velocity of the dry friction slider is zero, which means that

$$\dot{T} = -k_1\dot{y} \quad |T| < T_0$$

For $T = T_0$ we have the situation shown in figure F.3. We have multiplied v_s by an arbitrary real number ρ , which is to be determined later on. This non smooth function is parameterized by the parameter s as illustrated in the figure. This leads to

$$\dot{T} = \begin{cases} 0 & s \geq 0 \\ s & s < 0 \end{cases} \quad \rho v_s = \begin{cases} s & s \geq 0 \\ 0 & s < 0 \end{cases}$$

By adding these two equations we find that

$$\dot{T} + \rho v_s = s$$

and according to the previous equation for \dot{T} we see that

$$\dot{T} = [s]^- = -[-s]^+ = -[-\dot{T} - \rho v_s]^+ \quad T = T_0 \quad (\text{F.2})$$

where

$$[x]^+ = \begin{cases} x & x \geq 0 \\ 0 & x < 0 \end{cases} \quad [x]^- = \begin{cases} 0 & x \geq 0 \\ x & x < 0 \end{cases}$$

By substituting the sliding velocity of the dry friction slider from equation (F.1) into (F.2) we get

$$\dot{T} = - \left[-\dot{T} - \rho \left[-\dot{y} - \frac{\dot{T}}{k_1} \right] \right]^+ \quad T = T_0$$

by choosing $\rho = k_1$ we see that

$$\dot{T} = -[k_1 \dot{y}]^+ \quad T = T_0$$

Similarity, we have for $T = -T_0$ (see figure F.4)

$$\dot{T} = \begin{cases} s & s \geq 0 \\ 0 & s < 0 \end{cases} \quad \rho v_s = \begin{cases} 0 & s \geq 0 \\ s & s < 0 \end{cases}$$

thus

$$\dot{T} + \rho v_s = s$$

and according to the previous equation for \dot{T} we see that

$$\dot{T} = [s]^+ = \left[\dot{T} + \rho \left[-\dot{y} - \frac{\dot{T}}{k_1} \right] \right]^+ = [-k_1 \dot{y}]^+ \quad T = -T_0$$

Thus, we have found that

$$\dot{T} = \begin{cases} -k_1 \dot{y} & |T| < T_0 \\ -[k_1 \dot{y}]^+ & T = T_0 \\ [-k_1 \dot{y}]^+ & T = -T_0 \end{cases}$$

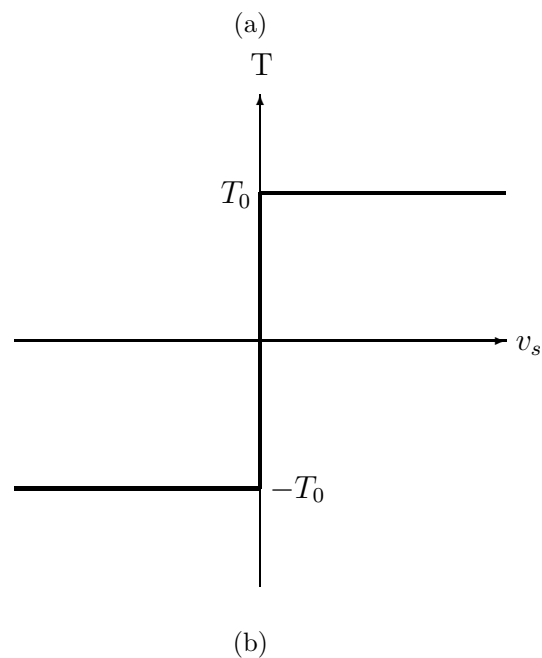
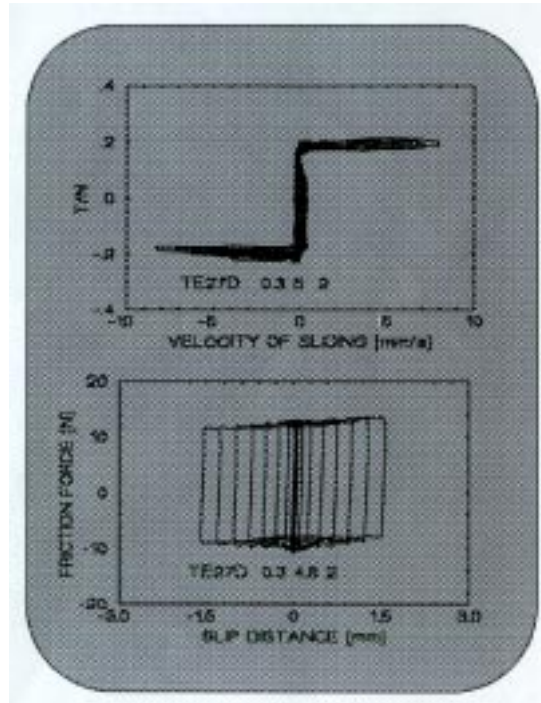


Figure F.2: (a) Measurement on clean surfaces confirming that the dry friction force obeys Coulomb's friction relation. (b) Schematic diagram of Coulomb's friction relation. It is *not* a mathematical function.

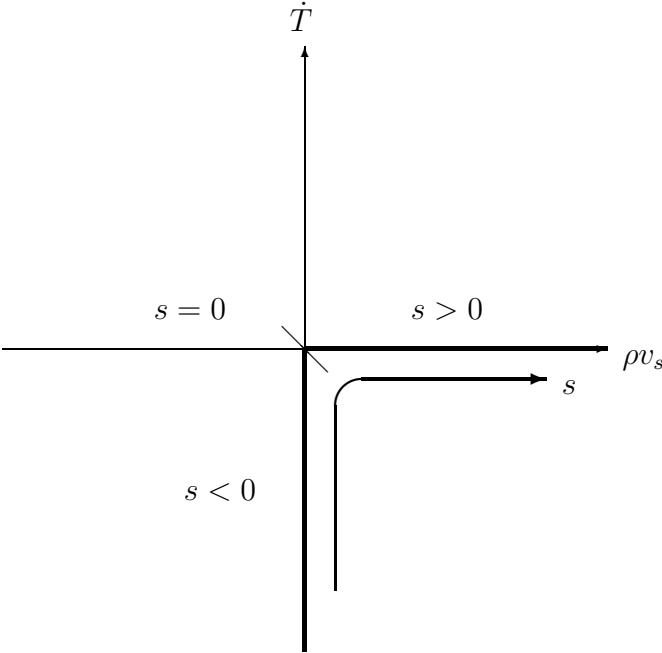


Figure F.3: $T = T_0$

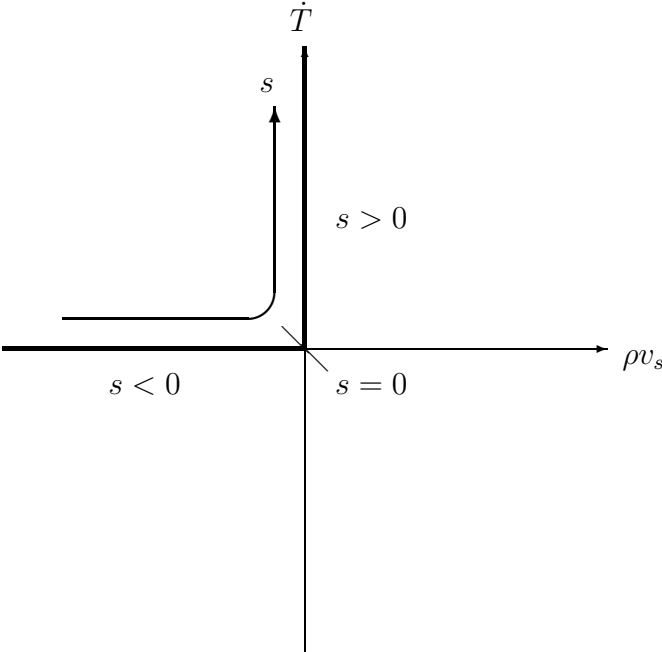


Figure F.4: $T = -T_0$

Appendix G

Maple Code for the Calculations of the Moment of Inertia

Our model of the car body consists of the following elements:

- (1) Underframe (6395 kg)
- (1) Floor (662 kg)
- (2) Front wall (550 kg each)
- (1) Roof (1339 kg)
- (4) Partition (244 kg each)
- (2) Sliding panels (1024 kg each)
- (4) buffer (149 kg each)
- (1) Center column (183 kg)
- (2) rail for sliding panels (132 kg each)

Total mass is 13563 kg

```
> restart;
> d1 := 0.6525; d2 := 1.595; d3 := 0.265; d4 := 2.350; d5 := 0.865; d6
:= sqrt(d1^2+d5^2); d7 := d1/2; d8 := 16.01; d9 := 2*d1 + d2;

d1 := .6525
d2 := 1.595
d3 := .265
d4 := 2.350
d5 := .865
d6 := 1.083504153
d7 := .3262500000
d8 := 16.01
d9 := 2.9000

> A_underframe := d8*(2*d1+d2); A_floor := A_underframe; A_frontwall :=
2*d1*d4 + d1*d5 + d2*(d4+d5); A_roof1 := d6*d8; A_roof2 := d2*d8;
> A_roof3 := A_roof1; A_roof := A_roof1 + A_roof2 + A_roof3; A_partition
:= A_frontwall; A_slidingpanels := d8*d4; l_cencol := d2+2*d4+2*d6;
> l_cencol1 := d4; l_cencol2 := d6; l_cencol3 := d2;

A_underframe := 46.429000
A_floor := 46.429000
A_frontwall := 8.7590875
A_roof1 := 17.34690149
A_roof2 := 25.53595
A_roof3 := 17.34690149
A_roof := 60.22975298
A_partition := 8.7590875
```

```

A_slidingpanels := 37.62350
L_cencol := 8.462008306
L_cencol1 := 2.350
L_cencol2 := 1.083504153
L_cencol3 := 1.595
> M_underframe := 6395; M_floor := 662; M_frontwall := 550; M_roof :=
> 1339; M_roof1 := A_roof1/A_roof*M_roof; M_roof2 :=
> A_roof2/A_roof*M_roof; M_roof3 := M_roof1; M_partition := 244;
> M_slidingpanels := 1024; M_buffer := 149; M_cencol := 183; M_cencol1
> := l_cencol1/l_cencol*M_cencol; M_cencol2 :=
> l_cencol2/l_cencol*M_cencol; M_cencol3 := l_cencol3/l_cencol*M_cencol;
> M_rail := 132; M_carbody := M_underframe + M_floor + 2*M_frontwall +
> M_roof + 4*M_partition + 2*M_slidingpanels + 4*M_buffer + M_cencol +
> 2*M_rail;

M_underframe := 6395
M_floor := 662
M_frontwall := 550
M_roof := 1339
M_roof1 := 385.6482876
M_roof2 := 567.7034249
M_roof3 := 385.6482876
M_partition := 244
M_slidingpanels := 1024
M_buffer := 149
M_cencol := 183
M_cencol1 := 50.82126895
M_cencol2 := 23.43193870
M_cencol3 := 34.49358467
M_rail := 132
M_carbody := 13563

```

Center of mass calculations of our model of the car body

Underframe

```

> r_cz_underframe := 0;
r_cz_underframe := 0

```

Floor

```

> r_cz_floor := d3;
r_cz_floor := .265

```

Front wall

```

> r_cz_frontwall_int1 := int(int(z,z=d3..d3+d4+d5/d1*y),y=0..d1):
> r_cz_frontwall_int2 := int(int(z,z=d3..d3+d4+d5),y=d1..d1+d2):
> r_cz_frontwall_int3 :=
> int(int(z,z=d3..d3+d4+d5-d5/d1*(y-d1-d2)),y=d1+d2..2*d1+d2):
> r_cz_frontwall := simplify(1/A_frontwall*(r_cz_frontwall_int1 +
> r_cz_frontwall_int2 + r_cz_frontwall_int3));
r_cz_frontwall := 1.787496379

```

Roof

```

> r_cz_roof := simplify(1/M_roof*(M_roof1*(d3+d4+d5/2) +
> M_roof2*(d3+d4+d5) + M_roof3*(d3+d4+d5/2)));
r_cz_roof := 3.230869478

```

Partition

```

> r_cz_partition_int1 := int(int(z,z=d3..d3+d4+d5/d1*y),y=0..d1):
> r_cz_partition_int2 := int(int(z,z=d3..d3+d4+d5),y=d1..d1+d2):
> r_cz_partition_int3 :=
> int(int(z,z=d3..d3+d4+d5-d5/d1*(y-d1-d2)),y=d1+d2..2*d1+d2):
> r_cz_partition := simplify(1/A_partition*(r_cz_partition_int1 +
> r_cz_partition_int2 + r_cz_partition_int3));

```

r_cz_partition := 1.787496379

Sliding panels

```

> r_cz_slidingpanels := d3+d4/2;

```

r_cz_slidingpanels := 1.440000000

Buffers

```

> r_cz_buffer := d3;

```

r_cz_buffer := .265

Center column

```

r_c = sum_{i=1}^N (m_i*r_i)/M_total = sum_{i=1}^N (L_i*r_i)/L_total
> r_cz_cencol := (2*M_cencol1*(d3+d4/2) + 2*M_cencol2*(d3+d4+d5/2) +
> M_cencol3*(d3+d4+d5))/M_cencol;

```

r_cz_cencol := 2.236178119

Rails for sliding panels

```

> r_cz_rail := d3+d4;

```

r_cz_rail := 2.615

Car body

Due to symmetry we have

```

> r_cx_carbody := d8/2;

```

r_cx_carbody := 8.005000000

Due to symmetry we have

```

> r_cy_carbody := d1 + d2/2;

```

r_cy_carbody := 1.450000000

```

r_c = sum_{i=1}^N (m_i*r_i)/M_total
> r_cz_carbody := simplify(1/M_carbody*(M_underframe*r_cz_underframe +
> M_floor*r_cz_floor + 2*M_frontwall*r_cz_frontwall + M_roof*r_cz_roof +
> 4*M_partition*r_cz_partition + 4*M_partition*r_cz_slidingpanels +
> 4*M_buffer*r_cz_buffer + M_cencol*r_cz_cencol +
> 2*M_rail*r_cz_rail));

```

r_cz_carbody := .8018408398

Adding freight

```

> M_freight := 20000;
> rho_freight := 19300;
> h_freight := M_freight/(rho_freight*d8*d9);

```

h_freight := .02231944323

```

> r_cz_freight := h_freight/2 + d3;
> r_cz_carbody := (M_carbody*r_cz_carbody +
> M_freight*r_cz_freight)/(M_carbody+M_freight);

```

r_cz_carbody := .4885904639

Moment of inertia calculations of our model of the car body

Underframe

```

Around a horizontal line through the center of mass of the underframe
> I_c_l1_underframe := 1/12*M_underframe*(2*d1+d2)^2;
                                     I_c_l1_underframe := 4481.829167
Around a horizontal line through the center of mass of the car body
> I_l1_underframe := I_c_l1_underframe +
> M_underframe*(r_cz_carbody-r_cz_underframe)^2;
                                     I_l1_underframe := 6008.447669
Around a vertical line through the center of mass of the underframe
> I_c_l2_underframe := 1/12*M_underframe*((2*d1+d2)^2+d8^2);
                                     I_c_l2_underframe := 141079.0825
Around a vertical line through the center of mass of the car body
> I_l2_underframe := I_c_l2_underframe + M_underframe*0^2;
                                     I_l2_underframe := 141079.0825

```

Floor

```

Around a horizontal line through the center of mass of the floor
> I_c_l1_floor := 1/12*M_floor*(2*d1+d2)^2;
                                     I_c_l1_floor := 463.9516667
Around a horizontal line through the center of mass of the car body
> I_l1_floor := I_c_l1_floor + M_floor*(r_cz_carbody-r_cz_floor)^2;
                                     I_l1_floor := 497.0468312
Around a vertical line through the center of mass of the floor
> I_c_l2_floor := 1/12*M_floor*((2*d1+d2)^2+d8^2);
                                     I_c_l2_floor := 14604.27718
Around a vertical line through the center of mass of the car body
> I_l2_floor := I_c_l2_floor + M_floor*0^2;
                                     I_l2_floor := 14604.27718

```

Front wall

```

> integrand_frontwall_l1 := (r_cy_carbody-y)^2 + (r_cz_carbody-z)^2:
> I_l1_frontwall_int1 :=
> int(int(integrand_frontwall_l1,z=d3..d3+d4+d5/d1*y),y=0..d1):
> I_l1_frontwall_int2 :=
> int(int(integrand_frontwall_l1,z=d3..d3+d4+d5),y=d1..d1+d2):
> I_l1_frontwall_int3 :=
> int(int(integrand_frontwall_l1,z=d3..d3+d4+d5-d5/d1*(y-d1-d2)),y=d1+d2
> ..2*d1+d2):

Around a horizontal line (parallel to the track ) through the center of mass of the car body
> I_l1_frontwall := M_frontwall/A_frontwall*(I_l1_frontwall_int1 +
> I_l1_frontwall_int2 + I_l1_frontwall_int3);
                                     I_l1_frontwall := 1720.707385

> integrand_frontwall_l2 := (r_cy_carbody-y)^2:
> I_l2_frontwall_int1 :=
> int(int(integrand_frontwall_l2,z=d3..d3+d4+d5/d1*y),y=0..d1):
> I_l2_frontwall_int2 :=
> int(int(integrand_frontwall_l2,z=d3..d3+d4+d5),y=d1..d1+d2):
> I_l2_frontwall_int3 :=
> int(int(integrand_frontwall_l2,z=d3..d3+d4+d5-d5/d1*(y-d1-d2)),y=d1+d2
> ..2*d1+d2):

Around a vertical line through the center of mass of the front wall
> I_c_l2_frontwall := M_frontwall/A_frontwall*(I_l2_frontwall_int1 +
> I_l2_frontwall_int2 + I_l2_frontwall_int3);
                                     I_c_l2_frontwall := 355.6217837

Around a vertical line through the center of mass of the car body
> I_l2_frontwall := I_c_l2_frontwall + M_frontwall*(d8/2)^2;
                                     I_l2_frontwall := 35599.63553

```

Roof

Roof 1
 Around a horizontal line through the center of mass of roof 1
 > I_c_l1_roof1 := 1/12*M_roof1*d6^2:
 Around a horizontal line through the center of mass of the car body
 > I_l1_roof1 := I_c_l1_roof1 +
 > M_roof1*((d1/2+d2/2)^2+(d3+d4+d5/2-r_cz_carbody)^2):
Roof 2
 Around a horizontal line through the center of mass of roof 2
 > I_c_l1_roof2 := 1/12*M_roof2*d2^2:
 Around a horizontal line through the center of mass of the car body
 > I_l1_roof2 := I_c_l1_roof2 + M_roof2*(d3+d4+d5-r_cz_carbody)^2:
Roof 3
 Around a horizontal line through the center of mass of the car body
 > I_l1_roof3 := I_l1_roof1:
Roof
 > I_l1_roof := I_l1_roof1 + I_l1_roof2 + I_l1_roof3;
 I_l1_roof := 11300.39135

Roof 1
 Around a vertical line through the center of mass of roof 1
 > I_c_l2_roof1 := 1/12*M_roof1*(d8^2+d1^2):
 Around a vertical line through the center of mass of the car body
 > I_l2_roof1 := I_c_l2_roof1 + M_roof1*(d1/2+d2/2)^2:
Roof 2
 Around a vertical line through the center of mass of roof 2
 > I_c_l2_roof2 := 1/12*M_roof2*(d8^2+d2^2):
 Around a vertical line through the center of mass of the car body
 > I_l2_roof2 := I_c_l2_roof2 + M_roof2*0^2:
Roof 3
 Around a vertical line through the center of mass of the car body
 > I_l2_roof3 := I_l2_roof1:
Roof
 > I_l2_roof := I_l2_roof1 + I_l2_roof2 + I_l2_roof3;
 I_l2_roof := 29722.77499

Partition

> integrand_partition_l1 := (r_cy_carbody-y)^2 + (r_cz_carbody-z)^2:
 > I_l1_partition_int1 :=
 > int(int(integrand_partition_l1,z=d3..d3+d4+d5/d1*y),y=0..d1):
 > I_l1_partition_int2 :=
 > int(int(integrand_partition_l1,z=d3..d3+d4+d5),y=d1..d1+d2):
 > I_l1_partition_int3 :=
 > int(int(integrand_partition_l1,z=d3..d3+d4+d5-d5/d1*(y-d1-d2)),y=d1+d2
 > ..2*d1+d2):

Around a horizontal line (parallel to the track) through the center of mass of the car body

> I_l1_partition := M_partition/A_partition*(I_l1_partition_int1 +
 > I_l1_partition_int2 + I_l1_partition_int3);
 I_l1_partition := 763.3683674

> integrand_partition_l2 := (r_cy_carbody-y)^2:
 > I_l2_partition_int1 :=
 > int(int(integrand_partition_l2,z=d3..d3+d4+d5/d1*y),y=0..d1):
 > I_l2_partition_int2 :=
 > int(int(integrand_partition_l2,z=d3..d3+d4+d5),y=d1..d1+d2):
 > I_l2_partition_int3 :=
 > int(int(integrand_partition_l2,z=d3..d3+d4+d5-d5/d1*(y-d1-d2)),y=d1+d2
 > ..2*d1+d2):

Around a vertical line through the center of mass of the partition

> I_c_l2_partition := M_partition/A_partition*(I_l2_partition_int1 +
 > I_l2_partition_int2 + I_l2_partition_int3);
 I_c_l2_partition := 157.7667550

Around a vertical line through the center of mass of the car body

> I_l2_partition := I_c_l2_partition + M_partition*(d8/2)^2;
 I_l2_partition := 15793.29286

Sliding panels

Around a horizontal line through the center of mass of the sliding panels

```
> I_c_l1_slidingpanels := 1/12*M_slidingpanels*d4^2;
                                     I_c_l1_slidingpanels := 471.2533333
```

Around a horizontal line through the center of mass of the car body

```
> I_l1_slidingpanels := I_c_l1_slidingpanels +
> M_slidingpanels*(r_cy_carbody)^2+(r_cz_slidingpanels-r_cz_carbody)^2)
> ;
                                     I_l1_slidingpanels := 3551.117761
```

Around a vertical line through the center of mass of the sliding panels

```
> I_c_l2_slidingpanels := 1/12*M_slidingpanels*d8^2;
                                     I_c_l2_slidingpanels := 21872.64853
```

Around a vertical line through the center of mass of the car body

```
> I_l2_slidingpanels := I_c_l2_slidingpanels +
> M_slidingpanels*(r_cy_carbody)^2;
                                     I_l2_slidingpanels := 24025.60853
```

Buffers

Around a horizontal line through the center of mass of the car body

```
> I_l1_buffer :=
> M_buffer*((d1+d2/2-d7)^2+(r_cz_buffer-r_cz_carbody)^2);
                                     I_l1_buffer := 195.6082069
```

Around a vertical line through the center of mass of the car body

```
> I_l2_buffer := M_buffer*((d1+d2/2-d7)^2+(d8/2)^2);
                                     I_l2_buffer := 9736.083020
```

Center column**cencol 1**

Around a horizontal line through the center of mass of cencol1

```
> I_c_l1_cencol1 := 1/12*M_cencol1*d4^2:
Around a horizontal line through the center of mass of the car body
> I_l1_cencol1 := I_c_l1_cencol1 +
> M_cencol1*((d1+d2/2)^2+(d3+d4/2-r_cz_carbody)^2):
```

cencol2

Around a horizontal line through the center of mass of cencol2

```
> I_c_l1_cencol2 := 1/12*M_cencol2*d6^2:
Around a horizontal line through the center of mass of the car body
> I_l1_cencol2 := I_c_l1_cencol2 +
> M_cencol2*((d1/2+d2/2)^2+(d3+d4+d5/2-r_cz_carbody)^2):
```

cencol3

Around a horizontal line through the center of mass of cencol3

```
> I_c_l1_cencol3 := 1/12*M_cencol3*d2^2:
Around a horizontal line through the center of mass of the car body
> I_l1_cencol3 := I_c_l1_cencol3 +
> M_cencol3*(d3+d4+d5-r_cz_carbody)^2:
```

center column

Around a horizontal line through the center of mass of the car body

```
> I_l1_cencol := 2*I_l1_cencol1 + 2*I_l1_cencol2 + I_l1_cencol3;
                                     I_l1_cencol := 1039.095259
```

cencol 1

Around a vertical line through the center of mass of the car body

```
> I_l2_cencol2 := M_cencol1*(d1+d2/2)^2:
```

cencol2

Around a vertical line through the center of mass of cencol2

```

> I_c12_cencol2 := 1/12*M_cencol2*d1^2:
Around a vertical line through the center of mass of the car body
> I_l2_cencol2 := I_c12_cencol2 + M_cencol2*(d1/2+d2/2)^2:

cencol3
Around a vertical line through the center of mass of cencol3
> I_c12_cencol3 := 1/12*M_cencol3*d2^2:
Around a vertical line through the center of mass of the car body
> I_l2_cencol3 := I_c12_cencol3:

center column

Around a vertical line through the center of mass of the car body
> I_l2_cencol := 2*I_l2_cencol2 + 2*I_l2_cencol2 + I_l2_cencol3;
                                         I_l2_cencol := 128.9988700

Rail for sliding panels

Around a horizontal line through the center of mass of the car body
> I_l1_rail := M_rail*((d1+d2/2)^2+(d3+d4-r_cz_carbody)^2);
                                         I_l1_rail := 874.3835120

Around a vertical line through the center of mass of the rail
> I_c12_rail := 1/12*M_rail*d8^2:
Around a vertical line through the center of mass of the car body
> I_l2_rail := I_c12_rail + M_rail*(d1+d2/2)^2;
                                         I_l2_rail := 3097.051100

Car body

Around a horizontal line through the center of mass of the car body
> I_l1_carbody := I_l1_underframe + I_l1_floor + 2*I_l1_frontwall +
> I_l1_roof + 4*I_l1_partition + 2*I_l1_slidingpanels + 4*I_l1_buffer +
> I_l1_cencol + 2*I_l1_rail;
                                         I_l1_carbody := 34973.30472

Around a vertical line through the center of mass of the car body
> I_l2_carbody := I_l2_underframe + I_l2_floor + 2*I_l2_frontwall +
> I_l2_roof + 4*I_l2_partition + 2*I_l2_slidingpanels + 4*I_l2_buffer +
> I_l2_cencol + 2*I_l2_rail;
                                         I_l2_carbody := 413097.2275

```

Adding freight

```

> I_l1_carbody := I_l1_carbody + 1/12*M_freight*(d9^2+h_freight^2) +
> M_freight*(r_cz_carbody - r_cz_freight)^2;
                                         I_l1_carbody := 49893.33806

> I_l2_carbody := I_l2_carbody + 1/12*M_freight*(d8^2+d9^2);
                                         I_l2_carbody := 854314.0608

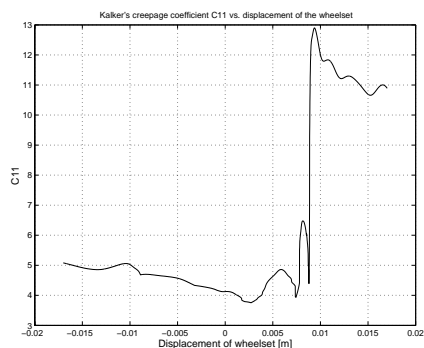
> r_cx_carbody; r_cy_carbody; r_cz_carbody;
                                         8.005000000
                                         1.450000000
                                         .4885904639

```

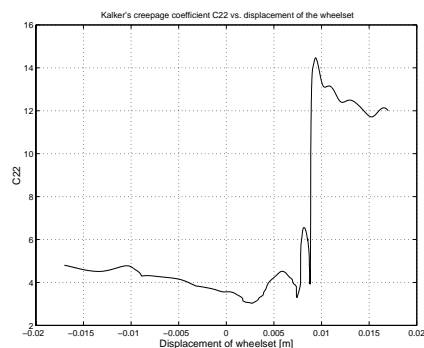

Appendix H

RSGEO table

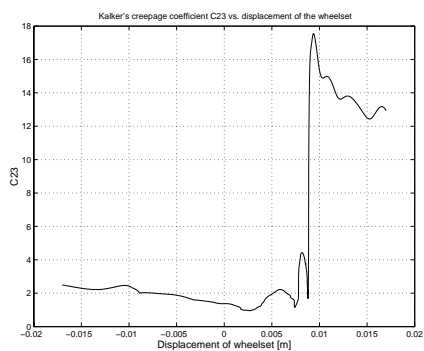
The data table known as the RSGEO table is of central importance to our simulations in that it stipulates important contact parameters related to the wheel-rail interface. This table, tabulated with respect to lateral motion of a wheelset, was created by Walter Kik for Lasse Engbo Christiansen, and used in [4]. In this chapter, we present a series of figures which demonstrate how important parameters in the wheel-rail interface change with shifting lateral movement of a wheelset. Importantly, all values were generated for a wheelset with S1002 profile wheels resting under its own weight on UIC60 rails, canted at $1/40$ towards the centerline for a track with a gauge of 1435 mm. Furthermore, the table is for the left wheel only, and we assume symmetry with respect to the right wheel.



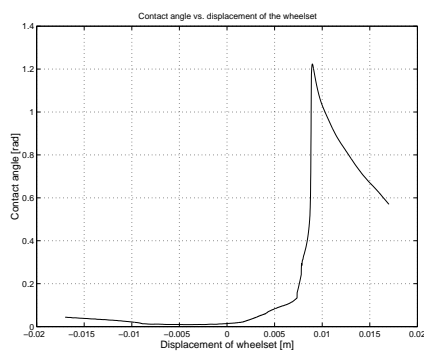
(a) Kalker's creepage coefficient C_{11} .



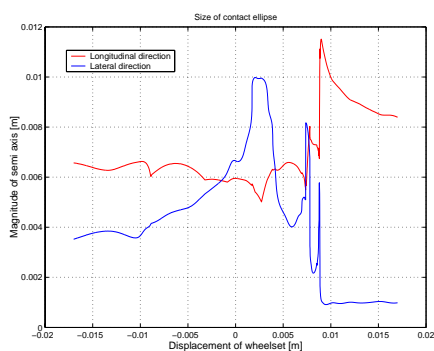
(b) Kalker's creepage coefficient C_{22} .



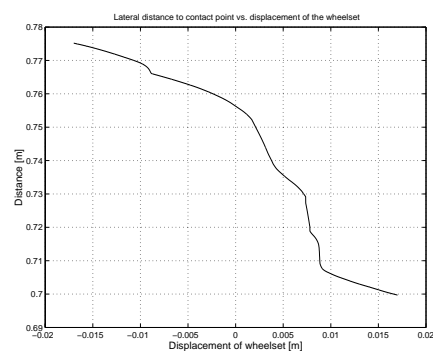
(c) Kalker's creepage coefficient C_{23} .



(d) Contact angle.

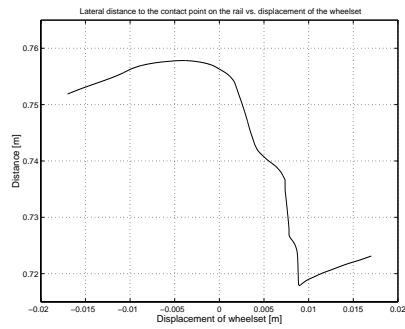


(e) Semi axes in contact ellipse.

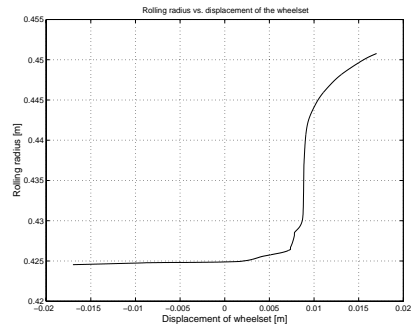


(f) Lateral distance to the contact point on the wheel.

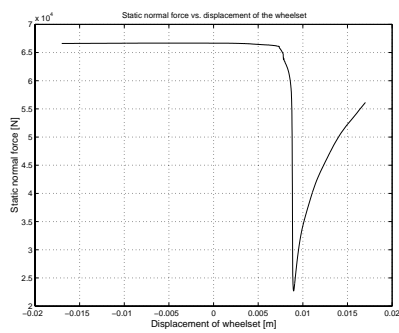
Figure H.1: RSGEO table (left wheel).



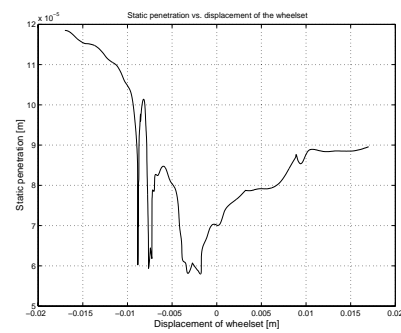
(a) Lateral distance to the contact point on the rail.



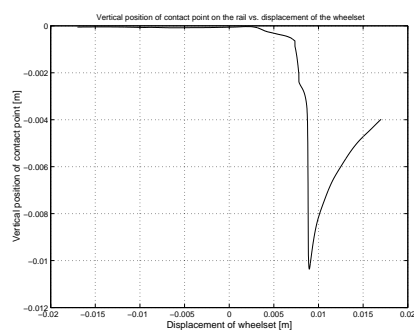
(b) Wheel rolling radius.



(c) Static normal force.



(d) Static penetration.



(e) Vertical position of the contact point on the rail.

Figure H.2: RSGEO table (left wheel).

Appendix I

Java Demonstration

We here present a series of figures which illustrate the **Java** based GUI for the **C++** code that implements our simulation model. As this is true cross platform code, we have shown screenshots for both Sun's Solaris as used by IMM¹, as well as Apple's FreeBSD UNIX based Mac OS X.2.6.

I.1 Sun Solaris 5.8

The figures presented in this section were produced under Sun's Solaris 5.8 which is used at IMM and a greater part of DTU.

¹Institute for Informatics and Mathematical Modelling

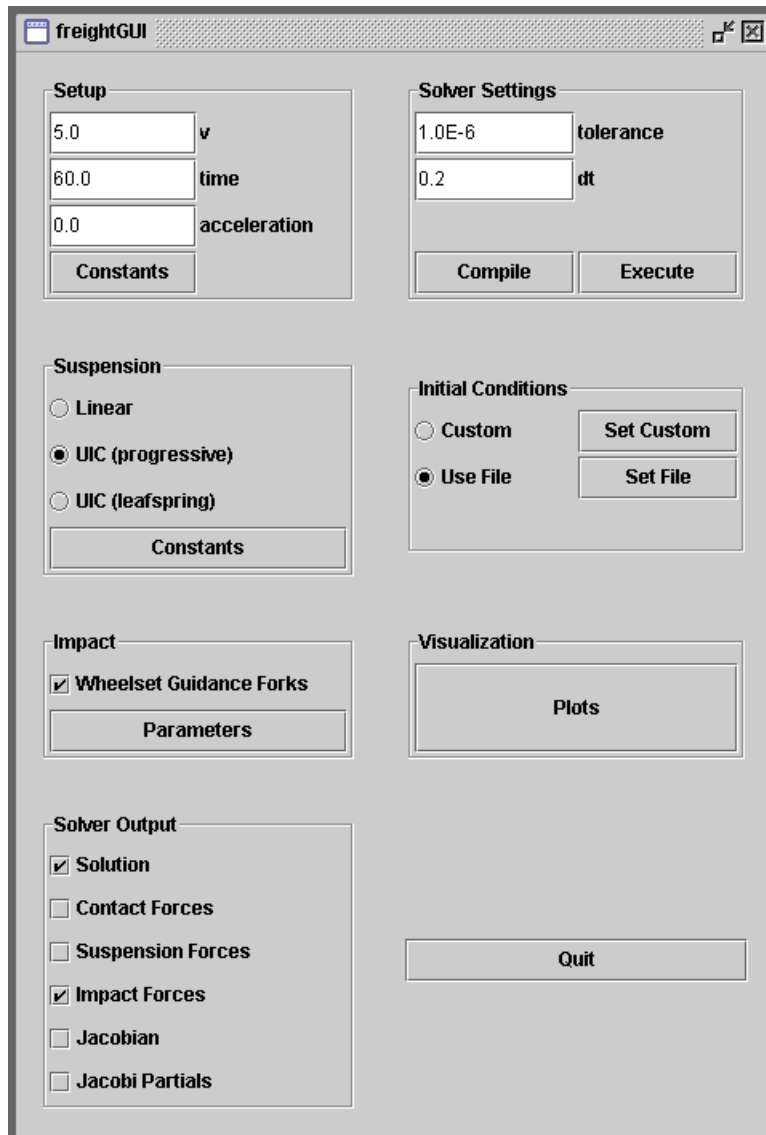


Figure I.1: Main program window under Solaris.

```
Parameter class created.
Wheelset class created.
Wheelset class created.
WheelRailContact class created.
WheelRailContact class created.
CarBody class created.
Suspension class created.
Impact class created.
-> Invoking Parameters::readFiles() ...
-> Loading Simulation Parameters ...
-> Loading Simulation Parameters OK
-> Loading Impact Parameters ...
-> Loading Impact Parameters OK
-> Loading Constants ...
-> Loading Constants OK
-> Loading UICLINVERT Parameters ...
-> Loading UICLINVERT Parameters OK
-> Invoking Parameters::readFiles() OK
-> Initialization ...
-> Initialization OK
-> SDIRK: Instance declared succesfully
-> Setting IC ...
-> Setting IC OK
*****
                SOLVER INFORMATION
*****
Time span = [0, 60]
dt         = 0.2
nvar       = 50
*****
PARAMETERS Object
v = 5
t = 60
a = 0
tol = 1e-06
dt = 0.2
impact = ON
out_sol = ON
out_contact = OFF
out_susp = OFF
out_impact = ON
out_jac = OFF
...
(t,v,Mstep) = (0.800,5.000, 59)|-----x-----|
Save Position      Break      Close
```

Figure I.2: Simulation output under Solaris.

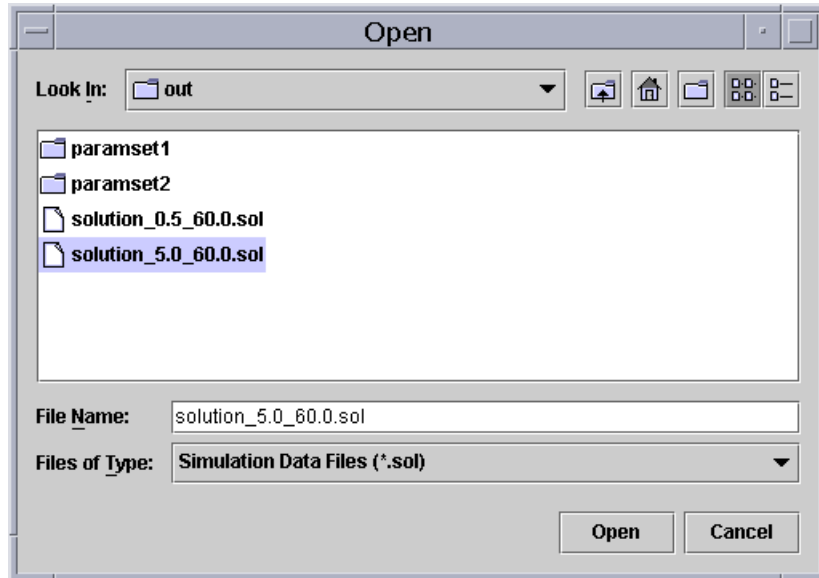


Figure I.3: Choosing a saved simulation file under Solaris.

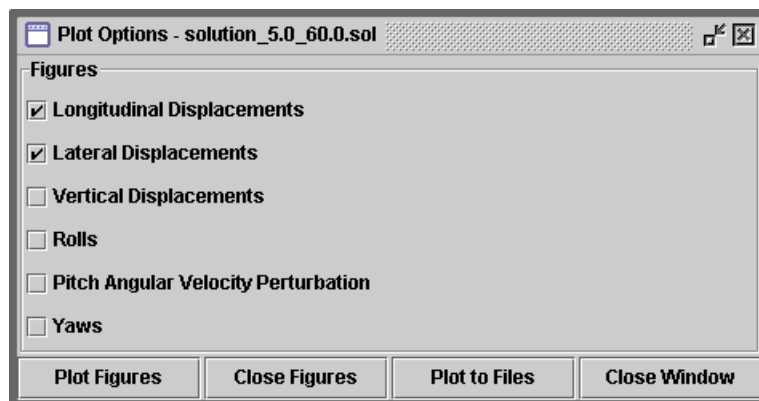


Figure I.4: Choosing what to plot under Solaris.

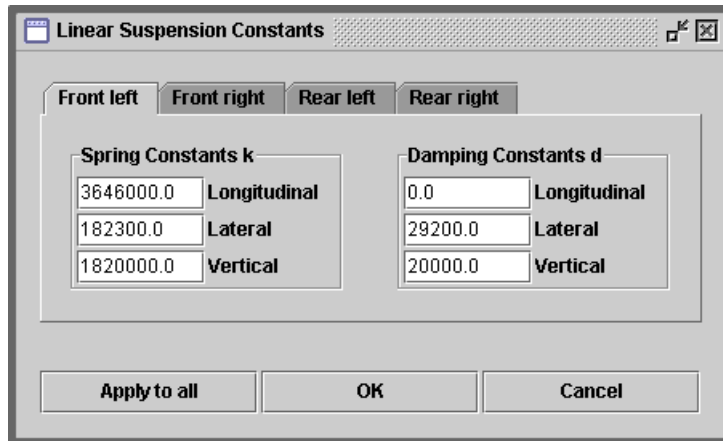


Figure I.5: Choosing linear suspension parameters under Solaris.

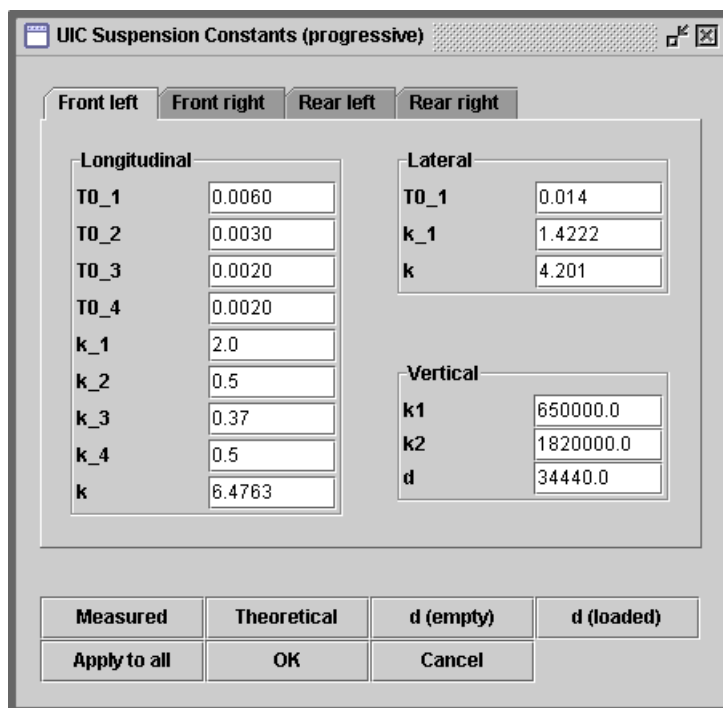


Figure I.6: Choosing progressive spring suspension parameters under Solaris.

UIC Suspension Constants (leafspring)

Front left Front right Rear left Rear right

Longitudinal

TO_1	0.00698
TO_2	0.00511
TO_3	9.1E-4
TO_4	0.00716
k_1	3.44
k_2	2.0
k_3	0.33
k_4	1.9
k	5.5

Lateral

TO_1	0.018
k_1	10.503
k	3.413

Vertical

c	650000.0
mu0	0.2
b	0.0015
Fr	6070.0

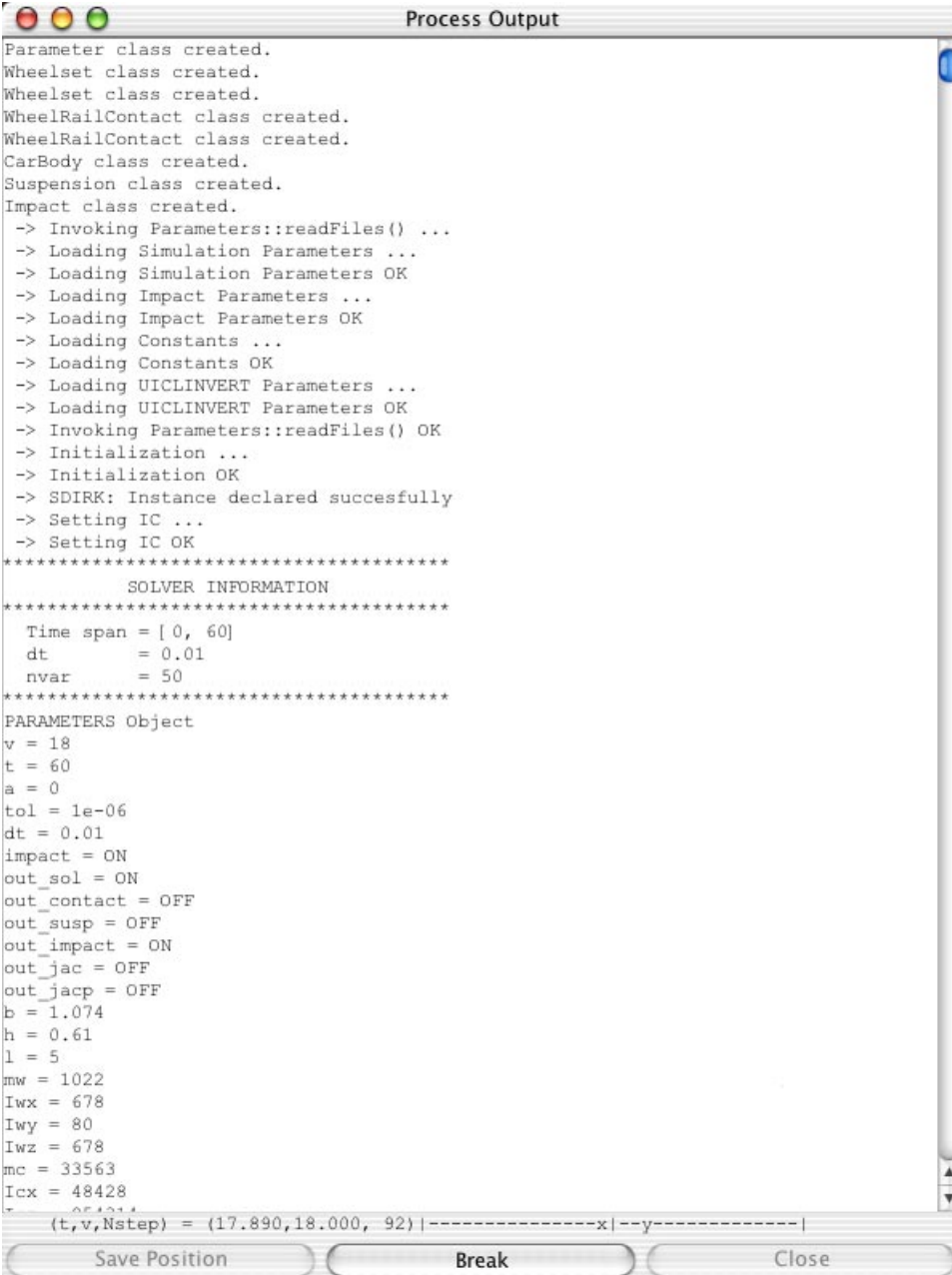
Measured Theoretical Apply to all

OK Cancel

Figure I.7: Choosing standard leaf spring suspension parameters under Solaris.

I.2 Apple Mac OS X.2.6 Jaguar

The figures presented in this section were produced under Apple's Mac OS X.2.6.



```
Parameter class created.
Wheelset class created.
Wheelset class created.
WheelRailContact class created.
WheelRailContact class created.
CarBody class created.
Suspension class created.
Impact class created.
-> Invoking Parameters::readFiles() ...
-> Loading Simulation Parameters ...
-> Loading Simulation Parameters OK
-> Loading Impact Parameters ...
-> Loading Impact Parameters OK
-> Loading Constants ...
-> Loading Constants OK
-> Loading UICLINVERT Parameters ...
-> Loading UICLINVERT Parameters OK
-> Invoking Parameters::readFiles() OK
-> Initialization ...
-> Initialization OK
-> SDIRK: Instance declared succesfully
-> Setting IC ...
-> Setting IC OK
*****
          SOLVER INFORMATION
*****
Time span = [ 0, 60]
dt          = 0.01
nvar        = 50
*****
PARAMETERS Object
v = 18
t = 60
a = 0
tol = 1e-06
dt = 0.01
impact = ON
out_sol = ON
out_contact = OFF
out_susp = OFF
out_impact = ON
out_jac = OFF
out_jacp = OFF
b = 1.074
h = 0.61
l = 5
mw = 1022
Iwx = 678
Iwy = 80
Iwz = 678
mc = 33563
Icx = 48428
t = 0.000000
(t,v,Nstep) = (17.890,18.000, 92) |-----x|---y-----|
Save Position      Break      Close
```

Figure I.8: Main program window under Mac OS X.

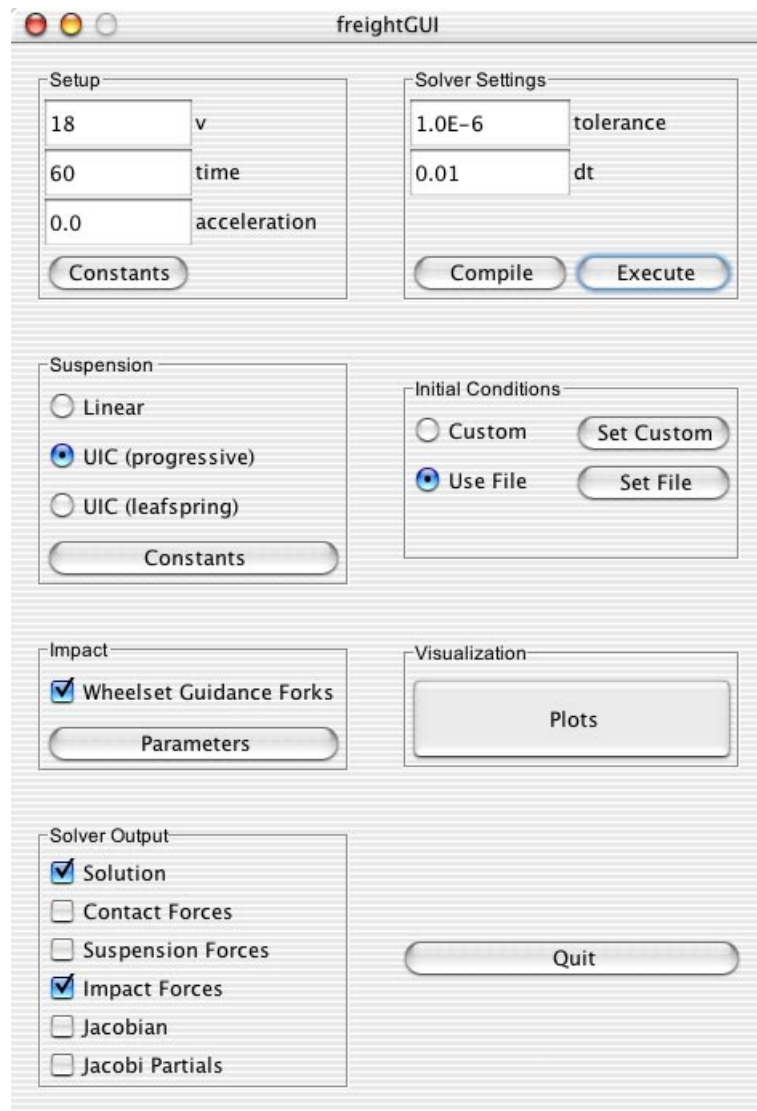


Figure I.9: Simulation output under Mac OS X.

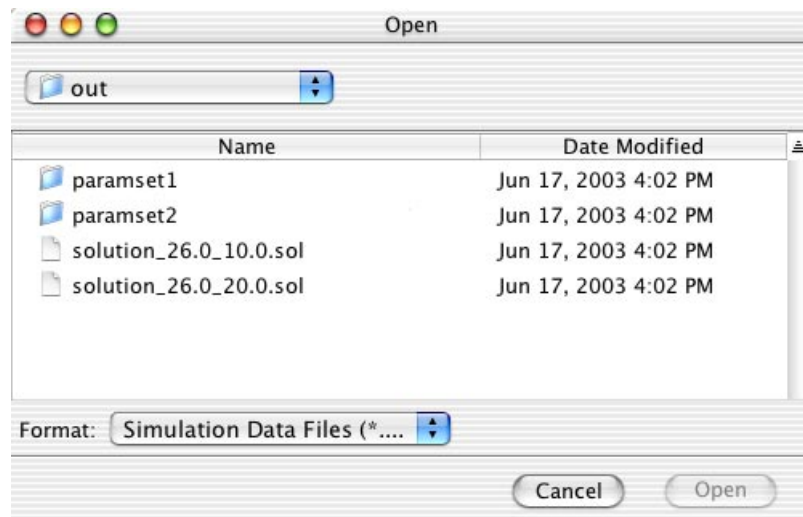


Figure I.10: Choosing a saved simulation file under Mac OS X.

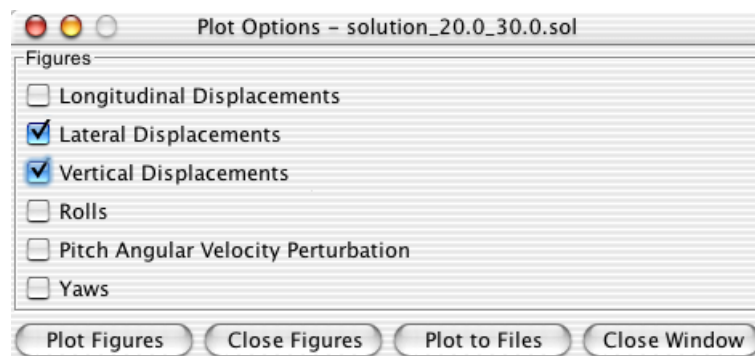


Figure I.11: Choosing what to plot under Mac OS X.

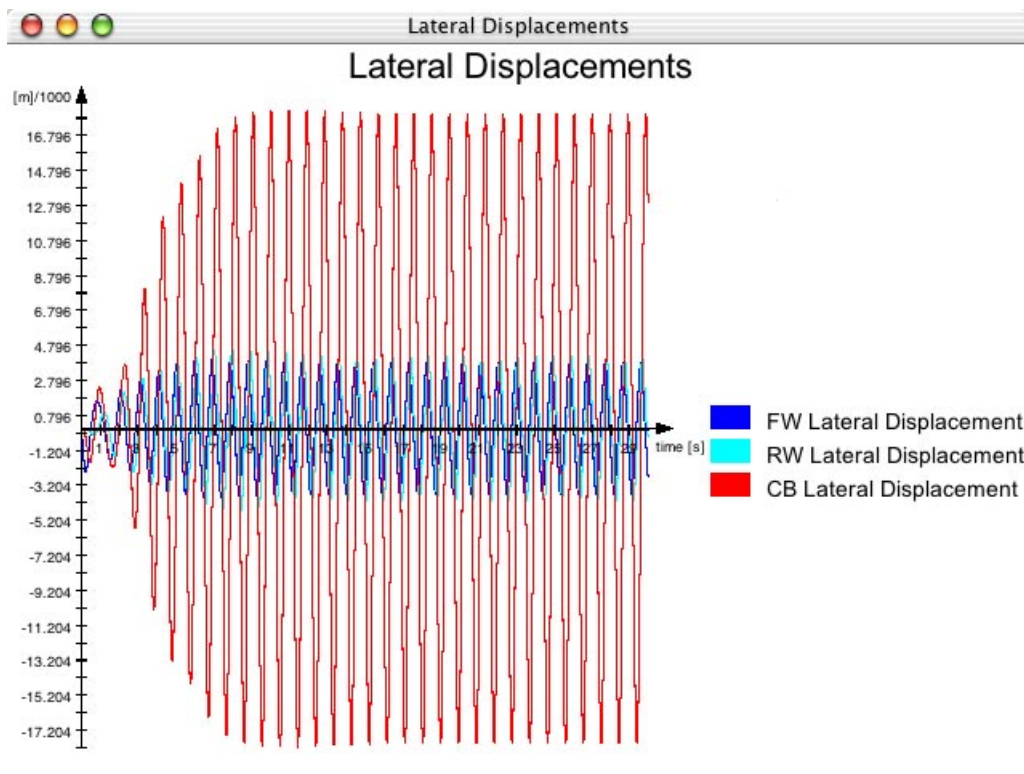


Figure I.12: Plot output under Mac OS X.

Bibliography

- [1] Barbara Blazejczyk-Okolewska, Krzysztof Czolczynski, Tomasz Kapitaniak, and Jerzy Wojewoda. *Chaotic Mechanics in Systems with Impacts and Friction*, volume 36 of *A*. World Scientific, 1999.
- [2] David Cebon. *Handbook of Vehicle-Road Interaction*. Swets & Zeitlinger.
- [3] Gunnar Christensen, Erik Both, and Preben Østergaard Sørensen. *Mekanik (in Danish)*. Scantryk A/S, 1997.
- [4] Lasse Engbo Christiansen. The Dynamics of a Railway Vehicle on a Disturbed Track. Master's thesis, Technical University of Denmark, June 2001.
- [5] Vijay K. Garg and Rao V. Dukkipati. *Dynamics of Railway Vehicle Systems*. Academic Press, 1984.
- [6] Wolfgang Hanneforth and Werner Fischer. *Laufwerke (in German)*. transpress VEB Verlag für Verkehrswesen, 1986.
- [7] Jens Christian Jensen. *Teoretiske og eksperimentelle dynamiske undersøgelser af jernbanekøretøjer (in Danish)*. PhD thesis, IMM-DTU, 1995.
- [8] Jerzy Piotrowski. A Mathematical Model of the UIC Link Suspension for Freight Wagons. Technical report, Institute of Vehicles, Warsaw University of Technology.
- [9] Eva Charlotte Slivsgaard. *On the Interaction Between Wheels and Rails in Railway Dynamics*. PhD thesis, IMM-DTU, 1995.
- [10] Steven H. Strogatz. *Nonlinear Dynamics and Chaos*. Perseus Books, 8 edition, 1998.
- [11] Henrik Thillman. Non-Linear Railway Vehicle Dynamics. Master's thesis, Technical University of Denmark, July 2000.
- [12] Lars Trzepacz. Railway Freight Vehicle Dynamics. Master's thesis, Technical University of Denmark, July 2002.